

Dissertation zur Erlangung des Doktorgrades
an der Fakultät für Mathematik und Physik
der Albert-Ludwigs-Universität Freiburg im Breisgau

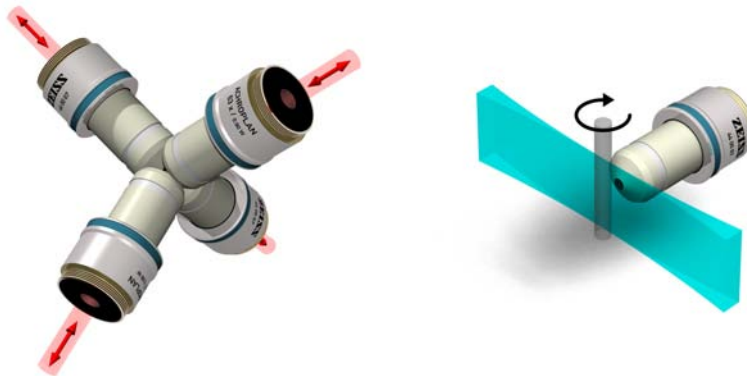


vorgelegt von
Jan Huiskens
aus Göttingen (Nds.)
2004

Dekan: Prof. Dr. R. Schneider
Betreuer: Prof. Dr. M. Weidemüller
Korreferent: Prof. Dr. H. Helm
Disputation: 30. August 2004

Multi-view microscopy and multi-beam manipulation for high-resolution optical imaging

Jan Huisken



Acknowledgements

The research work presented in this thesis has been carried out in the Light Microscopy Group of the European Molecular Biology Laboratory (EMBL) in Heidelberg, Germany.

I am grateful to Ernst Stelzer for giving me the chance to work in his group and for giving me insights into modern microscopy. Jim Swoger greatly contributed to the project's success. Thanks for everything.

I enjoyed the extraordinary interactive atmosphere in the institute and acknowledge Filippo Del Bene, Damian Brunner, Jan Ellenberg, Oliver Hantschel, Ferenc Jankovics, Thorsten Klee, Urban Liebel, Martina Rembold, Hanne Vermark, Jochen Wittbrodt for providing samples and fruitful discussions. Thanks to Sebastian Enders, James Jonkman, Klaus Greger, and the other former and present members of the Light Microscopy Group. It has been a pleasure to work with you.

This work would have been impossible without the technical support of Alfons Riedinger, Georg Ritter, Leo Burger, Wolfgang Dilling, and the other members of the electronical and mechanical workshops.

Thanks to Prof. Weidemüller for acting as the external supervisor of my thesis. I appreciate his friendly and straightforward character.

It has been an honor and an extremely inspiring experience to have been part of the International PhD Program at EMBL.

This work was financially supported by the BMBF (German Ministry of Education and Research) and the EMBL.

Thanks to Elke, Frieder, and Veronika.



Publications

v

Some of the results presented in this work have been previously published:

Articles

J. Huiskens, J. Swoger, F. Del Bene, J. Wittbrodt, E. H. K. Stelzer. Optical sectioning deep inside live embryos by Selective Plane Illumination Microscopy. *Science*, **305**, 1007 (2004).

J. Huiskens, J. Swoger, E. H. K. Stelzer. Three-dimensional optical manipulation using four collimated intersecting laser beams. *submitted* (2004).

J. Swoger, J. Huiskens, E. H. K. Stelzer. Multiple imaging axis microscopy improves resolution for thick sample applications. *Opt. Lett.*, **28**, 1654 (2003).

J. Huiskens, E. H. K. Stelzer. Optical levitation of absorbing particles in a nominally Gaussian laser beam. *Opt. Lett.*, **27**, 1223 (2002).

Conference proceedings

J. Huiskens, J. Swoger, E. H. K. Stelzer. Active particle manipulation with four laser beams, in: D. V. Nicolau, J. Enderlein, R. C. Leif, D. L. Farkas (eds.) Imaging, Manipulation, and Analysis of Biomolecules, Cells, and Tissues II. *Proc. SPIE* **5322** (2004).

Books

A. Rohrbach, J. Huiskens, E.-L. Florin, E. H. K. Stelzer. Photonic Force Microscopy, in: R. Rajagopalan (ed.): Optical trapping and manipulation of particles and polymers, Cambridge Univ. Press (in press).

A. Rohrbach, J. Huiskens, E. H. K. Stelzer. Optical trapping of small particles, in: P. Török, F. J. Kao (eds.): Optical Imaging and Microscopy, Springer: 357-386 (2003).

Conference Abstracts

J. Huiskens, J. Swoger, K. Greger, E. H. K. Stelzer. Selective plane illumination microscopy (SPIM) for “Biology’s new dimension”, 4th European Life Scientist Organisation Meeting 2004, Nice.

J. Huiskens, J. Swoger, E. H. K. Stelzer. Isotropic resolution and optical manipulation in multiview microscopy, Focus on Microscopy 2004, Philadelphia.

E. H. K. Stelzer, J. Swoger, J. Huisken. High and isotropic resolution with large samples in the selective plane illumination microscope (SPIM), Focus on Microscopy 2004, Philadelphia.

J. Huisken, J. Swoger, E. H. K. Stelzer. Active particle manipulation with four laser beams, SPIE Photonics West 2004, San Jose.

J. Swoger, J. Huisken, E. H. K. Stelzer. Multiple imaging axis microscopy (MIAM), SPIE Photonics West 2004, San Jose.

E. H. K. Stelzer, J. Swoger, J. Huisken. High-resolution observation of large samples in a widefield theta microscope, SPIE Photonics West 2004, San Jose.

J. Huisken, J. Swoger, E. H. K. Stelzer. Differential Active Optical Manipulator (DAOM): particle manipulation with four laser beams, Focus on Microscopy 2003, Genova.

J. Swoger, J. Huisken, E. H. K. Stelzer. Multiple Imaging Axis Microscopy (MIAM): improved resolution in optically thick samples, Focus on Microscopy 2003, Genova.

E. H. K. Stelzer, S. Enders, J. Swoger, J. Huisken. High-resolution observation of large samples in a widefield theta microscope, Focus on Microscopy 2003, Genova.

J. Swoger, J. Huisken, E. H. K. Stelzer. Multiple Imaging Axis Microscopy (MIAM), Focus on Microscopy 2002, Kaohsiung, Taiwan.

J. Huisken, E. H. K. Stelzer. Levitation and Rotation of Absorbing Micron-Sized Particles, Focus on Microscopy 2001, Amsterdam.

Patents

E. H. K. Stelzer, J. Huisken, S. Lindek, J. Swoger. Mikroskop, PCT/EP03/05991, pending.

E. H. K. Stelzer, S. Enders, J. Huisken, S. Lindek, J. Swoger. Mikroskop, German patent DE 10257423, pending.

E. H. K. Stelzer, J. Huisken. Verfahren und Instrument zur Positionierung und Orientierung kleiner Teilchen in einem Laserstrahl, German patent DE 10028418.

Contents

Introduction	1
Challenges in optical microscopy, 1 • Directions in biological imaging, 2 • This work, 3.	
CHAPTER 1 Multi-Imaging Axis Microscopy	5
1.1 Motivation	5
Fluorescence widefield microscopy, 5 • Point spread function, 7 • Confocal Microscopy, 9 • Single lens limitations, 11 • Improving the resolution, 12 • Confocal theta microscopy, 15.	
1.2 Multi-view microscopy	18
Goals of multi-view combination, 18 • Experimental realizations, 19.	
1.3 Image processing	21
1.4 The tetrahedral multi-imaging axis microscope	26
Design, 26 • Setup, 27.	
1.5 Experimental methods and results	31
Sample preparation, 31 • Data pre-processing, 32 • Data fusion, 35.	
CHAPTER 2 The Differential Active Optical Manipulator	37
2.1 Optical manipulation	39
Introduction, 39 • Collimated beams, 39 • Optical levitation and active feedback, 40 • Optical Tweezers, 41 • Multi-beam arrangements, 43 • Four beam manipulation, 45.	
2.2 Theory	47
Forces in collimated laser beams, 47 • Forces in a four beam manipulator, 51.	
2.3 Setup	56
2.4 Experimental results	60
Conclusion, 64.	
CHAPTER 3 Selective Plane Illumination Microscopy	67
3.1 Challenges of imaging large samples	69
Optical sectioning, 69 • Light sheet thickness, 73 • Imaging in heterogeneous tissue, 76.	

3.2	The Selective Plane Illumination Microscope	77
	Setup, 77 • Data collection for multi-view reconstruction, 77 •	
	Image processing outline, 80.	
3.3	Example 1: Medaka fish embryo	82
3.4	Example 2: <i>Drosophila melanogaster</i>	87
3.5	Performance of the SPIM	90
	Lateral resolution, 90 • Comparison with confocal microscopy, 90	
	• Penetration depth and aberrations with SPIM, 93.	
3.6	Conclusion	95
CHAPTER 4 Summary and Conclusion		97
Appendix		99
Bibliography		109

Introduction

Imaging techniques that provide a picture of the object under investigation are key tools for the sciences: *a picture is worth a thousand words*. In the wide range from Ångstroms explored by X-ray diffraction to lightyears depicted by telescopes various imaging techniques have been developed and perfected during the centuries. Specifically in biology and medicine, optical microscopy techniques are well established and widespread. They provide a noninvasive and nondestructive way of imaging processes in live specimens.

The technique of fluorescence microscopy is one of the main applications of microscopy in biological and medical research. The sample can be fluorescently labelled with a variety of dyes that specifically bind to organelles, compartments of the cell or single proteins. Nowadays, the family of green fluorescent proteins (GFP) with its spectral variants are routinely applied to study gene and protein expression and to track single molecules in whole animals and single cells *in vivo*. The focus of this work is mainly on fluorescence microscopy.

Challenges in optical microscopy

A figure of merit often used in optical microscopy is the *resolution*. The resolving power of a microscope is fundamentally limited by the spatial and temporal frequencies to which it exposes the sample as well as the spatial and temporal frequencies it can collect in response. Three main components determine the performance of the microscope, (1) the instrument itself, i. e. the optics and the imaging mode used, (2) the wavelengths of the light used (exposure and response), and (3) the sample that is imaged. The influence of the sample is often underestimated. However, the properties of the specimen can heavily limit the achievable resolution. The overall resolution of an instrument is therefore often worse than the theoretically expected resolution, when only (1) and (2) are taken into account.

The resolution of a microscope is heavily dependent on the optical thickness and the inhomogeneity of the sample. The resolution and the signal to noise ratio are therefore generally a function of the depth at which the microscope is focused inside the sample. For applications where large samples are imaged the

penetration depth of the microscope is a crucial characteristic. In terms of resolution an optical microscope should provide the best possible resolution within the constraints of a given experiment.

Even though it is obvious that high resolution is important and worth to strive for; it is by far not the only characteristic of a microscope. When looking at live specimen the influence of the microscope and its light on the sample is especially crucial. Photo-toxicity and heating can easily damage the sample or make it behave abnormally. When looking at fluorescent markers in the specimen one has to be aware of the fact that intensive excitation has photo-toxic and destructive effects. Photo-bleaching is the most obvious, resulting in a loss of signal. Live specimens are often dynamic, and the image acquisition speed of the microscope has to keep up with the processes under investigation.

The practical use of a microscope is therefore determined by both its physical parameters and its biocompatibility. For some fixed specimens (e. g. in cell biology) high resolution might be the ultimate goal, if the acquisition speed and possible bleaching are of minor interest. However, for many of applications, especially dynamic studies *in vivo*, the microscope has to fulfill more challenging requirements. For example fluorescence imaging throughout an intact embryo for several hours or days of its development requires the microscope to be capable of collecting high resolution data at high speed with minimal stress for the sample. The goal of light microscopy must be to provide the ideal instrument (in terms of resolution, contrast, speed, etc.) for a given (biological) problem. If, moreover, the microscope enables new experiments that have been infeasible before, then such an instrument is especially valuable.

Directions in biological imaging

All imaging techniques require the user to prepare the specimen in a certain way. The mounting of the sample has to be appropriate for the microscope and the objective lens (working distance, field of view). From the imaging point of view, the sample is ideal if it is transparent, flat, spatially fixed, and exhibits strong contrast. Therefore, if possible, the sample is prepared to allow ideal imaging conditions.

This also means that the scientist concentrates on specimens or organisms that he is able to image. For example cell biologists have been cultivating their cells in a flat topology. Growing cells on coverslips makes them “compatible” with existing light microscopes. This, however, does not resemble the conditions found in tissue. Hence, cultivated cells represent an artificial biology adapted to the requirements of the microscope. This may have no implications for some results, but can lead to severe artefacts when looking at cell mechanics and migration or intracellular signaling. Techniques like electron microscopy that require

even stricter sample preparation techniques also suffer from these problems, but they cannot be used for studies on live specimens and therefore do not claim to record the “dynamic reality”.

Three-dimensional cell cultures more closely mirror what happens in living organisms. They are becoming increasingly popular because people have experienced that the results in 2D and 3D cultures can differ dramatically (*Abbott, 2003*). The field of cell migration has already profited from 3D cell cultures (*Webb and Horowitz, 2003*).

This work

The work presented in this thesis tackles all the mentioned challenges in optical microscopy and opens the third dimension for biological experiments like 3D cell cultures. Two instruments were built that provide high and isotropic resolution. In the *Multi Imaging Axis Microscope (MIAM)* four objective lenses are used to both image the sample and to manipulate it with optical forces. The *Selective Plane Illumination Microscope (SPIM)* is especially well suited for large biological samples and provides optical sectioning deep inside the specimen, efficient fluorescence excitation and reduced photo-bleaching. A technique for gentle sample preparation and manipulation is presented. Both instruments share the technique of multi-view combination to improve the overall image quality and the resolution in all directions.

The text is split into three chapters: the first two deal with the Multi Imaging Axis Microscope. The MIAM is a wide-field optical microscope that observes a sample simultaneously from multiple directions without requiring the sample to be rotated or tilted. The prototype is capable of high-resolution imaging of the interior of a 300 μm -diameter sample. Compared with a single-axis system, the MIAM can achieve a reduction of the axial point-spread function elongation by a factor of 5.8 and a 3.5-fold improvement in volume resolution by simple linear image combination techniques. Chapter 1 presents the underlying principle, the setup and the imaging capability of the MIAM. The gentle manipulation of samples in this microscope by optical forces is demonstrated in chapter 2. Chapter 3 presents the SPIM. The optical sectioning obtained is explained and illustrated, as is the procedure of multi-view combination.

1. Multi-Imaging Axis Microscopy

The Multi-Imaging Axis Microscope (MIAM) is a system in which four objective lenses are used to generate 3D images of a sample from four sides simultaneously. The fusion of these data sets yields an overall improved resolution throughout the whole sample.

1.1 Motivation

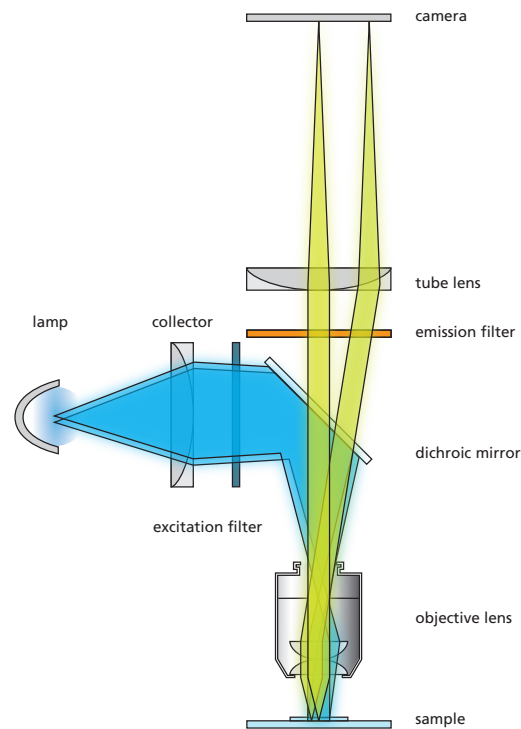
Fluorescence microscopy is an essential tool in modern life sciences, and in particular in biology (*Hurtley and Helmuth, 2003*). Like all forms of imaging it is subject to physical limits on its resolving power. The anisotropy of the resolution inherent in conventional single lens designs is especially undesirable. It leads to artefacts in the resulting images and can therefore lead to misinterpretations and false quantifications of the data. This introductory section explains conventional widefield and confocal microscopes, introduces the point spread function, and illustrates the drawbacks of single lens systems. Finally, the various approaches in the literature to improve the resolution in microscopy are summarized.

1.1.1 Fluorescence widefield microscopy

In a classical optical microscope the object in the focal plane of the optics is imaged onto the image plane. This image plane is either observed by eye through an ocular, or a camera is placed in this plane to capture the image. Most common are microscopes in which the image is formed by a telecentric system consisting of an objective lens and a tube lens. The objective lens is usually interchangeable. The magnification M of such a system is determined by the ratio of the focal lengths of the tube lens f_{TL} and of the objective lens f_{OL} . In a *widefield microscope* the sample is illuminated uniformly throughout the field of view that is imaged, and the image is captured at once by eye or camera.

In an *epifluorescence microscope* a set of two filters and a dichroic mirror are used for selective excitation and detection of fluorescence in the sample (Fig. 1.1).

Fig. 1.1 Classical epifluorescence microscope. Illumination (blue) and detection path (green) are shown schematically each exemplarily with two ray bundles. A broadband light source is used for excitation. Excitation and detection bands are selected with excitation and emission filters and a dichroic mirror. The image is recorded with a camera.



The excitation filter transmits the appropriate band of the spectrum of the lamp and the dichroic mirror reflects it into the objective lens and onto the sample. The fluorescence light emitted by the fluorophores in the sample is collected by the same objective lens and transmitted by the dichroic mirror and the detection filter.

The characteristics of a *widefield epifluorescence microscope* (Fig. 1.1) are therefore

Widefield epifluorescence microscope

1. single lens for illumination and detection,
2. uniform illumination,
3. widefield detection (e. g. with a camera).

The resolution of any imaging system is limited. In an ideal* conventional microscope the resolution is determined by the wavelength of the light λ and the numerical aperture $NA = n \cdot \sin \alpha$ of the objective lens, where n is the refractive index of the medium in which the sample is embedded and α is half the opening angle of the cone over which light is collected. Knowledge of these values is sufficient to characterize the imaging properties of a conventional microscope as it has been introduced so far.

* Influences of the sample and the resulting deterioration of resolution are discussed later.

1.1.2 Point spread function

The imaging performance of a microscope is best described in terms of its *point spread function (PSF)*. The *amplitude PSF* $h(x, y, z)$ reflects the strength of the electromagnetic field in the image plane when observing a point-like light source. However, only the *intensity PSF* $|h(x, y, z)|^2$, the squared modulus of the amplitude PSF, is detectable. This describes the image formed by a point object. It can be experimentally determined by moving a sub-resolution object (fluorescent bead) through the focal plane and consecutively recording the image of the object. Real objects can often be regarded as a collection of point objects; the image I of such an object is the three-dimensional convolution of the object structure O and the intensity PSF $|h(x, y, z)|^2$

$$I(x, y, z) = O(x, y, z) \otimes |h(x, y, z)|^2. \quad (1.1)$$

According to *Born and Wolf* (1999), the amplitude PSF is given by

$$h(u, v) = -i \frac{2\pi n A \sin^2 \alpha}{\lambda} e^{i u / \sin^2 \alpha} \int_0^1 J_0(v\rho) e^{-i u \rho^2 / 2} \rho d\rho, \quad (1.2)$$

where A is the area of the aperture and J_0 the zeroth-order Bessel function.* v and u are normalized optical units perpendicular and parallel to the optical axis, respectively, and are given by

$$v = \frac{2\pi n r \sin \alpha}{\lambda}, \quad u = \frac{2\pi n z \sin \alpha}{\lambda}, \quad r^2 = x^2 + y^2, \quad (1.3)$$

i. e. the beam propagates parallel to the z -axis and r is the distance to the beam's axis.

The intensity PSF is the product of the amplitude PSF and its complex conjugate

$$|h(u, v)|^2 = h(u, v) \cdot h^*(u, v). \quad (1.4)$$

The intensity PSF $|h|^2$ can be understood: (1) as the intensity distribution in the object resulting from a point source illumination located in the image plane, and (2) as the relative probability of a photon, emitted from a certain location in the object, hitting a point detector in the image plane. Since the two events of illumination and detection are independent, the *overall intensity* PSF $|h_{\text{tot}}|^2$ is described by the product of the functions describing the *illumination* and the *detection* PSFs

$$|h_{\text{tot}}|^2 = |h_{\text{ill}}|^2 \cdot |h_{\text{det}}|^2. \quad (1.5)$$

*The equation and the results obtained from it are only valid close to the focus. For simplicity, polarization is not taken into account in the calculations.

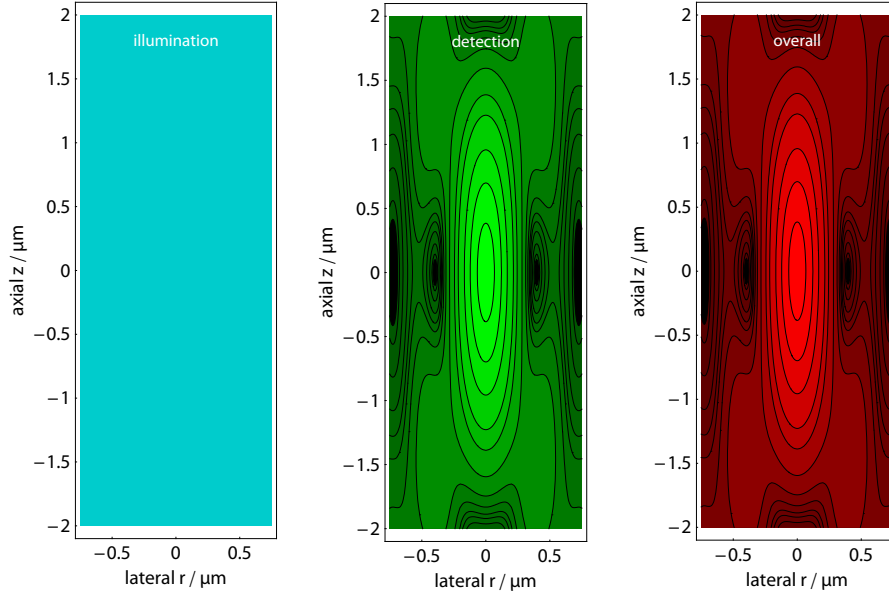


Fig. 1.2 Intensity point spread functions (PSF) in a widefield microscope. The conventional widefield microscope is characterized by the uniform illumination (left). The overall PSF (right) is obtained by multiplying the detection (middle) and illumination PSFs. The overall PSF is in this case identical to the detection PSF (middle). $\lambda = 520 \text{ nm}$, $\text{NA} = 0.8$, $n = 1.33$. Contour lines are plotted for intensities of 0.9, 0.7, 0.5, 0.3, 0.2, 0.1, 0.05, 0.03, 0.02, 0.015, 0.01, 0.005, 0.002, 0.001. The intensities are shown with a look-up-table (LUT) of gamma = 0.25, in blue for excitation, in green for detection, and in red for the product.

In a fluorescence widefield microscope, in which the whole sample is evenly illuminated (no point illumination), i. e. $|h_{\text{ill}}|^2 \equiv 1$, the overall PSF is identical to the detection PSF

$$|h_{\text{widefield}}|^2 = |h_{\text{det}}|^2. \quad (1.6)$$

The PSFs for some typical parameters ($\lambda_{\text{det}} = 520 \text{ nm}$, $\text{NA} = 0.8$, $n = 1.33$) are plotted in Fig. 1.2. Clearly visible is the elongation along the z -axis, the optical axis. The full width at half maximum (FWHM) of the central peak is about a factor five larger in the axial direction than it is in the lateral direction for the given parameters.

The FWHM in the lateral and the axial directions of the PSF can be seen as a measure of the lateral and axial resolution, respectively. The resolution is the minimum distance between two point object that can still be sufficiently distinguished. Various definitions of what “sufficient” is exist in the literature. The most common is the *Rayleigh criterion*, which says that two objects are resolved when the first minimum of a PSF profile along the direction of interest is aligned with the central maximum of a second PSF profile. For the lateral direction (in

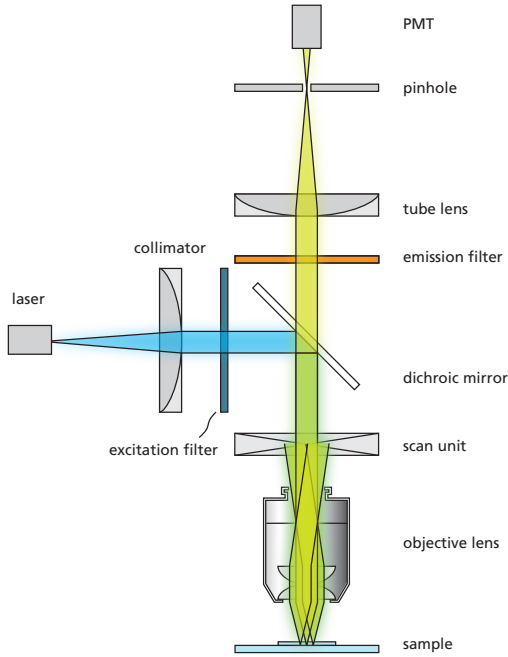


Fig. 1.3 Confocal fluorescence microscope. Schematically illumination (blue) and detection path (green) are shown.

the x, y -plane) this is

$$R_{x,y} = \frac{1.22\lambda}{2NA} \approx \frac{0.6\lambda}{NA}. \quad (1.7)$$

In our example this means that the lateral resolution is

$$R_{x,y;(\lambda=520\text{ nm}, NA=0.8)} \approx 0.40 \mu\text{m}.$$

Correspondingly, in axial direction one gets

$$R_z = \frac{2\lambda n}{NA^2}, \quad (1.8)$$

$$R_z;(\lambda=520\text{ nm}, NA=0.8, n=1.33) \approx 2.2 \mu\text{m}.$$

Note that the resolution in the axial direction is dependent on the inverse square of the NA. An increase of the NA therefore has a strong effect, e. g. from $NA = 0.8$ to 1.3 the axial resolution improves from $2.2 \mu\text{m}$ to $0.82 \mu\text{m}$.

1.1.3 Confocal Microscopy

In a confocal laser scanning microscope the sample is illuminated by a focused beam (see Fig. 1.3), point-by-point. This is achieved by a set of scanning mirrors that move the excitation beam across the sample in a raster fashion. Detection with a widefield detector (photo-multiplier) is performed through a pinhole. This pinhole is placed in a conjugate plane to the focal plane and thereby

ensures that only light that stems from the focus is detected.* The confocal fluorescence microscope is characterized by

Confocal fluorescence microscope

1. single lens for illumination and detection,
2. focused illumination (beam scanning),
3. point-wise detection through a pinhole.

The focused excitation beam in a confocal microscope is described by the illumination PSF, and the detection through the pinhole is quantified by the detection PSF (Fig. 1.4). Again, the overall PSF (1.5) is the product of the two

$$|h_{\text{confocal}}(x, y, z)|^2 = |h_{\text{ill}}(x, y, z)|^2 \cdot |h_{\text{det}}(x, y, z)|^2. \quad (1.9)$$

In contrast to a widefield microscope, the confocal illumination PSF is not constant: it describes the point illumination. Since the same objective lens is used for the illumination and detection in a confocal microscope, the illumination and the detection PSF differ only in the wavelengths λ_{ill} and λ_{det} , respectively. In fluorescence microscopy the emission maximum of the fluorophore is usually close to the excitation maximum. For example for the Green Fluorescent Protein GFP, which is most frequently excited with an Ar^+ -laser, the illumination wavelength is $\lambda_{\text{ill}} = 488 \text{ nm}$ and detection is around $\lambda_{\text{det}} = 520 \text{ nm}$. Hence $|h_{\text{ill}}|^2$ and $|h_{\text{det}}|^2$ are nearly identical, which means the total PSF of a confocal microscope is approximately the square of the conventional PSF (1.6).

The FWHM of the PSF of a confocal microscope is for this reason reduced by a factor of approximately $1/\sqrt{2}$ in both directions, i. e. the resolution is enhanced by about 30 %.

$$R_{x,y,\text{conf}} = \frac{1.22\lambda_{\text{em}}}{2\sqrt{2}\text{NA}} \approx \frac{0.4\lambda_{\text{em}}}{\text{NA}} \quad (1.10)$$

$$R_{x,y,\text{conf}}(\lambda_{\text{em}}=520 \text{ nm}, \text{NA}=0.8) \approx 0.27 \mu\text{m}.$$

$$R_{z,\text{conf}} = \frac{\sqrt{2}\lambda_{\text{em}}n}{\text{NA}^2} \approx \frac{1.4\lambda_{\text{em}}n}{\text{NA}^2} \quad (1.11)$$

$$R_{z,\text{conf}}(\lambda_{\text{em}}=520 \text{ nm}, \text{NA}=0.8) \approx 1.5 \mu\text{m}.$$

In addition, the side lobes are reduced relative to the central peak and the signal is mainly obtained from the central volume. However, the overall shape of the PSF, i. e. its axial elongation, is not changed at all. The axial resolution is still worse than the lateral by the same factor as in the conventional microscope. A drawback of the confocal microscope is the low image acquisition

*The function of the pinhole and the resulting optical sectioning capability of the confocal microscope are discussed in section 3.1.1.

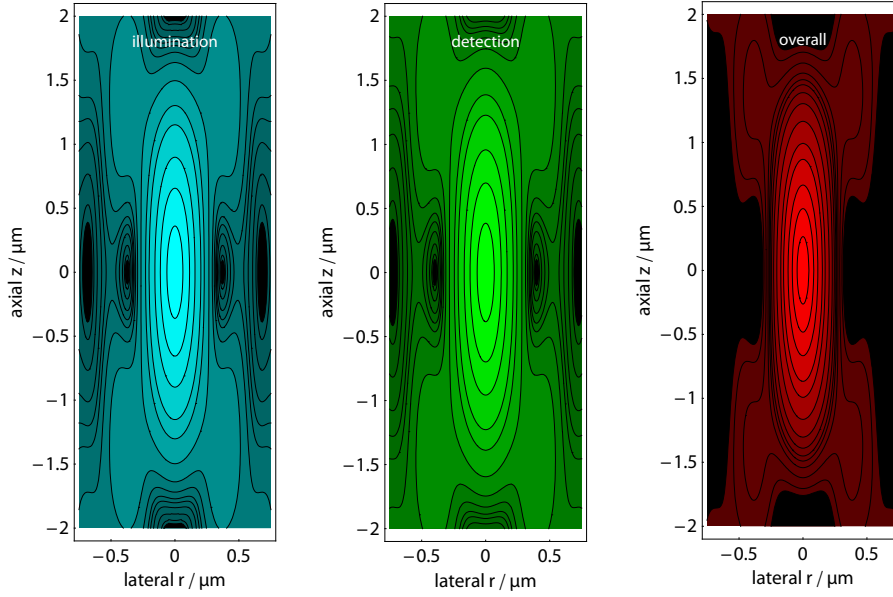


Fig. 1.4 Confocal point spread functions (PSF). Point illumination (left) and point detection (center) yield an overall improved resolution (right). Compared to the conventional microscope, the overall PSF in a confocal microscope is narrower in both dimensions and side lobes are suppressed. $\lambda_{\text{ill}} = 488$, $\lambda_{\text{det}} = 520$, $\text{NA} = 0.8$, $n = 1.33$. Same contour lines and LUT as in Fig. 1.2.

speed because of the time required for the scanning which is necessary to acquire a full image. In addition, often when working with low fluorescence intensities the pinhole diameter has to be increased beyond its ideal size, which reduces the resolution of the confocal microscope. The true advantage of the confocal microscope, namely its optical sectioning capabilities are discussed in section 3.1.1.

1.1.4 Single lens limitations

The anisotropy of the PSF, i. e. its pronounced elongation along the optical axis, is an effect of the limited NA: the light emitted from the sample is collected only within a limited angle. The anisotropy of the resolution

$$\frac{R_{x,y}}{R_z} = \frac{1.22}{4n} \text{NA} \approx 0.3 \sin \alpha$$

is an intrinsic property of single lens microscopy. The axial resolution is at best a factor of about three lower than the lateral resolution.

The image obtained in the microscope is the convolution of the actual object and the PSF of the instrument used (1.1). Therefore, the image of an object is

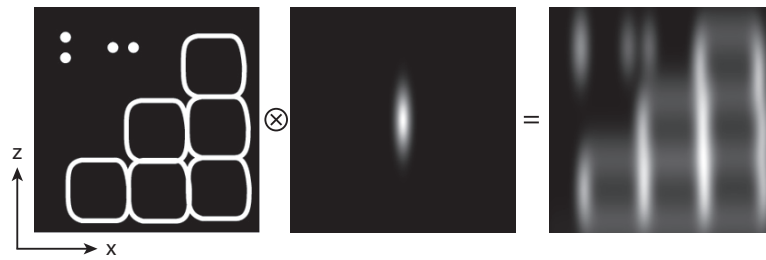


Fig. 1.5 A simulated 2D sample (left) is convolved with an anisotropic PSF (center) to yield the image (right). The PSF is a factor of four wider in z than in x . This results in a strong blur in z and a poor resolution in this direction. The two axially aligned objects in the top left corner cannot, whereas the two that are laterally displaced can be distinguished. In addition, structures along z appear brighter in the image than similar structures extended in x .

smear out and particularly strongly blurred in the axial direction. In addition to the fact that fewer fine structures along z can be resolved, artefacts are introduced that are caused by the anisotropy of the PSF. This phenomenon is illustrated in Fig. 1.5. As expected, closely spaced circles along z cannot be resolved in contrast to circles distributed along x . Moreover, a strong enhancement of structures oriented along z is striking. The membranes of the stylized cells that extend along x are washed out whereas the cell walls along z show up as bright lines. This demonstrates that an *isotropic* resolution, which avoids artefacts of this sort, is of great interest. When viewing thin, flat samples such as cultured cells on a coverslip, this is not a significant restriction; however, current biological applications increasingly demand three-dimensional (3D) information about millimeter-sized samples, for which poor axial resolution is often a serious issue.

1.1.5 Improving the resolution

The formulas for the resolution in a conventional widefield microscope ((1.7), (1.8)) have been derived under the following *assumptions*:

1. observation is done in the conventional geometry, in which light is collected by a single lens with a certain NA,
2. the excitation is uniform throughout the sample,
3. fluorescence is excited by a single photon in a linear process.

Under these assumptions, the resolution can be improved only by two means. The lateral and axial resolutions can be improved by

1. decreasing the wavelength of light used to image the sample, and
2. by using an objective lens of higher numerical aperture (see (1.7), (1.8)).

Of course, the available range of fluorophores and the specimen limit the range of applicable wavelengths. Biological samples are sensitive in the UV, objective lenses are well corrected only in the visible, and, most importantly for many applications, only a few staining protocols exist. Therefore, the experiment dictates the choice of fluorophore and wavelengths to excite and detect it.

The numerical aperture of available objective lenses is at maximum 1.4. This can only be achieved using oil as immersion medium, which can result in severe aberrations when looking at biological samples in aqueous medium. A water-immersion lens with a lower NA is often the better choice. In addition to their limited effectiveness, the two methods of improving the resolution given above still leave the axial resolution worse than the lateral. The problem of the anisotropy of the PSF cannot be solved by these means.

One can also achieve a resolution improvement by negation of one or more of the three assumptions. This, however, involves new microscope designs and different modes of operation. Several microscope designs and techniques to increase the resolution have been suggested and experimentally demonstrated in the literature (*Gustafsson, 1999*). Improved resolution can be obtained for example by using excitation light that varies with position. In section 1.1.3 it has been shown that for a *confocal microscope*, in which the concept of spatially varying illumination is realized by point illumination, the resolution can be improved by a factor of $1/\sqrt{2}$ (see (1.10),(1.11)).

Another example for a realization of spatially varying excitation light is the technique of *structured illumination*, in which the sample is illuminated with a sinusoidal pattern. This has been shown to be a powerful technique to increase both the axial and lateral resolutions. Using a conventional (single lens) wide-field microscope the sample is illuminated with spatially structured excitation light. A series of images is taken with different orientations of the pattern and by computational processing of the data the unmodulated image is restored at a higher resolution than the conventional image. In *standing wave fluorescence microscopy (SWFM)* (*Bailey et al., 1993*) the sample is excited by the interference of two counter-propagating waves in *axial* direction. The combination of three images acquired with different phases of the pattern yields an improved axial resolution. However, since the individual fringes cannot be distinguished the technique only works for samples thinner than the fringe spacing. In lateral direction a two-fold resolution improvement can be achieved by *laterally structured illumination* (*Gustafsson, 2000*). Since this improvement is only achieved along a single direction (the direction perpendicular to the stripes) the pattern has to be rotated several times and many images have to be taken to achieve an improvement in all directions in the x - y -plane.*

*This technique of structured illumination should not be confused with the optical sectioning technique of *Neil et al. (1997)* discussed in section 3.1.1.

Another approach is the process of non-linear excitation of the sample. In *two-photon microscopy* (Zipfel *et al.*, 2003), intense light pulses of approximately twice the wavelength of the normal excitation light are used to induce fluorescence. Two-photon microscopy allows deeper penetration into scattering samples because of the longer wavelength that is used (which reduces scattering and absorption), and it provides optical sectioning (subject of section 3.1.1) because of the nonlinear effect of two-photon absorption exploited. However, it does not increase the resolution. In contrast, the resolution is reduced by about 15 % (Jonkman and Stelzer, 2002). In *stimulated emission depletion microscopy* (STED) (Hell, 2003) the excitation spot in a confocal microscope is shaped by a sequence of two pulses. The excitation spot of the first pulse has the extent of a regular PSF. The second pulse (with a higher wavelength than the fluorescence emission) is shaped such that it depletes most of the initial fluorescence from the outer regions of the PSF. Excited molecules are forced by stimulated emission into an upper vibrational level of the ground state whose fast vibrational decay prevents re-excitation. This leaves a fluorescent spot with an axial extent that is six-fold and a lateral extent that is 2-fold reduced (Klar *et al.*, 2000).

The collection angle, i. e. the angular aperture, can be doubled by using a second objective on the other side of the sample. In a *4Pi confocal fluorescence microscope* (Hell and Stelzer, 1992) the sample is illuminated coherently through both objectives. The wavefronts interfere in the focal volume and produce a central maximum that is four to five times narrower along the optical axis than in a conventional microscope. Unfortunately, secondary maxima are very pronounced; they can be reduced by two-photon excitation and by computational deconvolution. Different operating modes exist where the fluorescence light is either incoherently detected with one lens (4Pi(A)) or coherently with both lenses (4Pi(B) and 4Pi(C)).

A similar approach in the widefield context is *I⁵M microscopy* (Gustafsson *et al.*, 1999). Again, two lenses are used for illumination and detection. I⁵M combines two techniques. In image interference microscopy (I²M) the light from both lenses is coherently collected on a single detector providing improved axial resolution (this is analogous to 4Pi-B microscopy). This can be combined with incoherent interference illumination producing axial fringes and encoding high axial resolution (I³M, analogous to 4Pi-A).

All of these methods require sophisticated equipment and alignment procedures, and are limited in their image acquisition speeds. In structured illumination microscopy from three to several hundred images must be taken to reach the desired resolution improvement. In addition, the illumination pattern has to penetrate to the focal plane undistorted. If the pattern is not as expected, i. e. it varies across the field of view or changes with depth, the method can result in artefacts. This limits the range of samples for which the technique can be successfully used. Due to the slow acquisition speed, bleaching of the fluorophores

can be a serious issue and the imaging of live samples might be impossible. The 4Pi and STED microscopes are especially challenging to build and align. They are also very slow in acquisition speed because of the scanning that is required in confocal microscopes.

A direct approach to tackle the anisotropy problem of the PSF and the resulting artefacts is to use two or more lenses for illumination and/or detection, oriented along non-parallel, intersecting axes. Rotation of the detection lens with respect to the illumination lens also rotates the associated PSF. The extent of the overall PSF (the product of illumination and detection PSF) becomes dominated by the lateral resolution of both lenses. This idea is realized in the confocal theta microscope (following section) and in the widefield context in the SPIM (Selective Plane illumination Microscope, chapter 3).

1.1.6 Confocal theta microscopy

The approaches presented so far are (widefield or confocal) methods that use either one or two axially aligned objective lenses. A variation of confocal microscopy in which this linear arrangement of lenses is given up is *confocal theta microscopy* (Stelzer and Lindek, 1994). In this technique the sample is illuminated by a point source through one objective lens, and a second objective lens, whose optical axis is at an angle θ to the illumination axis, is used to image the emitted fluorescence onto a point detector (see Fig. 1.6). The sample is scanned through the overlap of the illumination and detection volumes to build up an image of the sample. The confocal theta fluorescence microscope is characterized by:

Confocal theta microscope

1. two separate axes for illumination and detection,
2. focused illumination (sample scanning),
3. point-wise detection through a pinhole.

As for the confocal microscope (1.9), the PSF of such a microscope is described by the product of illumination and detection PSF. Because of the orientation (we assume a rotation of the illumination of 90° about y) the variables of the illumination PSF x and z need to be interchanged, yielding

$$|h_{\text{theta}}(x, y, z)|^2 = |h_{\text{ill}}(-z, y, x)|^2 \cdot |h_{\text{det}}(x, y, z)|^2. \quad (1.12)$$

The illumination, detection and overall PSF are plotted in Fig. 1.6. Clearly, by separating illumination and detection and orienting them perpendicularly the anisotropy of the PSF is nearly eliminated. The extent of the overall PSF along the detection axis is dominated by the lateral extent of the illumination PSF. This makes the overall PSF nearly isotropic.

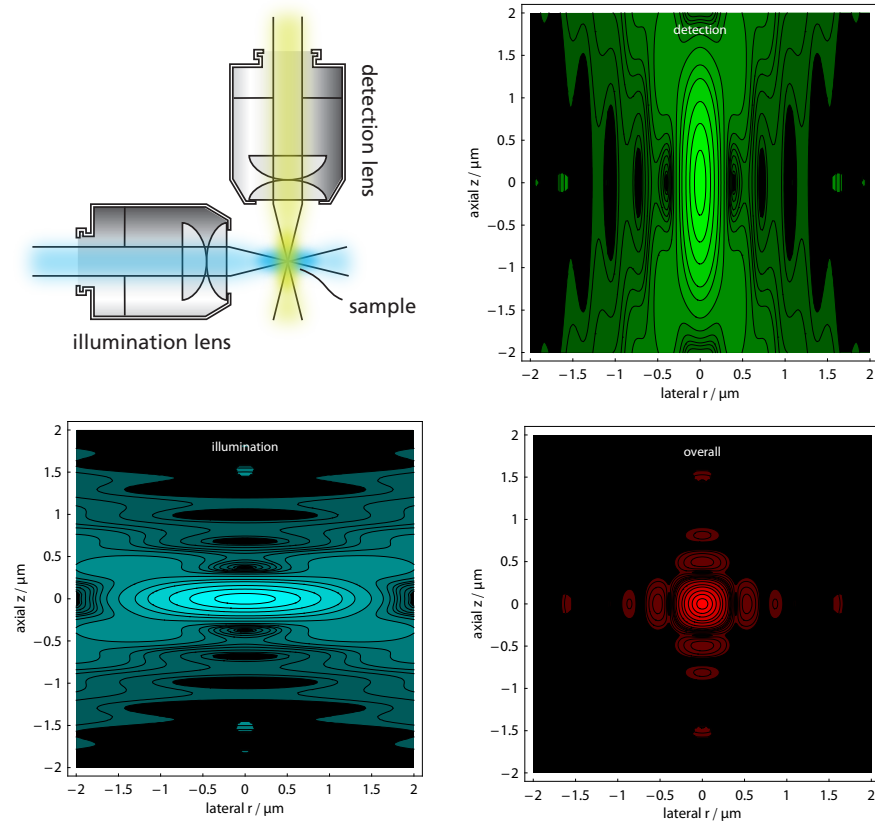


Fig. 1.6 Arrangement of objective lenses and intensity point spread functions (PSF) in a confocal theta microscope. Illumination and detection lenses are in a perpendicular arrangement (top left). The overall PSF (bottom right) is obtained by multiplying the illumination (bottom left) and detection PSF (top right). $\lambda_{\text{ill}} = 488 \text{ nm}$, $\lambda_{\text{det}} = 520 \text{ nm}$, $\text{NA} = 0.8$, $n = 1.33$. Same contour lines and LUT as in Fig. 1.2.

The concept of theta microscopy is general, describing a confocal microscope in which the angle between the illumination and the detection lens is θ (hence the name). However, smallest confocal volumes are obtained if they are perpendicular ($\theta = 90^\circ$) (Lindek *et al.*, 1994b) and acceptably small volumes if the angle is between 70° and 110° (Lindek *et al.*, 1994a). In addition to the two lens solution shown in Fig. 1.6 (Lindek *et al.*, 1995), a more compact single-lens theta microscope has been developed (Lindek *et al.*, 1997; Swoger *et al.*, 1998). In this setup illumination and detection are performed through the same lens side-by-side. The illumination beam is reflected off a small mirror that is placed next to the sample and illuminates it from the side. The concept of theta microscopy has also been extended to 4Pi microscopy (Lindek *et al.*, 1994a,b). Variations of the theta microscope have been build by Wang *et al.* (2003) and Palero *et al.* (2002). A theoretical analysis of a six-lens system in which four objectives are used for coherent illumination and two for coherent detection has been presented by Haeberle *et al.* (2001).

Due to physical limitations of the objective arrangement, the theta principle can only be realized with objectives with sufficiently low NA (max. 0.8–0.9). This has to be taken into account when evaluating and comparing PSFs of a confocal and a confocal theta microscope. However, the resolution along the detection axis in a theta microscope is always better than that in a confocal microscope with a high-NA lens.

In addition to the sophisticated alignment of such a system, the main limitations of theta microscopy are the sample preparation and the image acquisition speed. In the literature, the sample has been mounted on, for example, a glass capillary. Especially in the single-lens theta the small working distance limits the range of samples that it is practical to image. Moreover, beam scanning like in a classical confocal microscope is only possible in one dimension in the theta microscope (Wang *et al.*, 2003). The sample has to be scanned in at least two dimensions for a full 3D data set, an inherently slow procedure since distortions of the object by the movement have to be avoided.

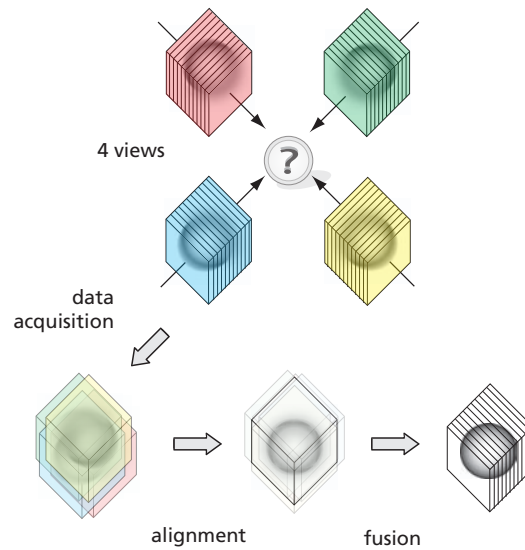


Fig. 1.7 Multi-view combination. In this example, the four image stacks of the sample that are taken from different angles feature good lateral resolution on the side facing the camera. The goal of multi-view combination is to combine the data sets such that “useful” information (in terms of the experiment), is extracted and merged into the final image. The poor information in one stack is thereby replaced by the best available information from the other stacks.

1.2 Multi-view microscopy

Another approach to tackle the problem of poor axial resolution is known as multi-view (or tilted-view) microscopy (*Shaw et al.*, 1989). With this method 3D images of the sample are taken from at least two different angles and then combined, so that in the reconstructed image the good (lateral) resolution from one view is used to compensate for the poor (axial) resolution from another.

1.2.1 Goals of multi-view combination

The idea in multi-view microscopy is to take a set of image stacks from the same object. Each data set represents a certain image of the sample taken from the particular angle (an example is illustrated in Fig. 1.7). Depending on the properties of the imaging system used to acquire these images, the data sets can be classified. Possible characterization parameters are

- anisotropy of the PSF (i. e. *directional* variations in image quality),
- *positional* variations of the image quality, and
- combinations of these two.

After the images have been acquired each data stack can be rated according to some of the criteria and with respect to the information that one strives for. If the imaging provides isotropic resolution the resolution of all data sets will be the same in all directions. If the sample is transparent and its homogenous refractive index matches the immersion medium there might be no distortions and no obscured information in any data set. However, in most microscopes the resolution is not isotropic, and most samples induce some sort of scattering or attenuation of the excitation and fluorescence light or other artefacts. Therefore, each data set is very likely to have particular features that are superior to features in other data sets.

The goal in multi-view microscopy is to fuse the different data sets to a single data set that inherits all desired information. More precisely, the needless information in any data set will be replaced by better information from another data set (if available). For this, one has to define, which information is desired and which is needless. Although it depends on the particular experiment, in microscopy the goal generally is an undistorted and complete image of the sample with a high resolution in all directions. In widefield and other microscopies this means that ideally the poor axial resolution of all data sets is improved. Also any attenuation of the signal in some parts of the sample should be removed without amplification of noise. This means that the figure of merits are resolution and signal to noise ratio. Therefore, the algorithm to fuse the data sets has to favor these two parameters (see section 1.3).

1.2.2 Experimental realizations

The idea of a widefield multi-view microscope can be realized in two ways. One option is to use a single lens for detection and to rotate the sample in order to acquire image stacks from different sides. This has been demonstrated in the literature and is often termed tilted-view microscopy (Agard, 1984; Bradl *et al.*, 1992, 1994; Can *et al.*, 2003; Kozubek *et al.*, 2002; Shaw, 1990; Shaw *et al.*, 1989). In order to get maximum resolution in the reconstruction it is necessary to rotate the sample by angles of up to 180° . However, a full rotation can be favorable as has been mentioned in the previous section to fill in missing information of e. g. the back side of the sample. Therefore the sample cannot be mounted on a conventional slide. The maximum tilt with a high numerical aperture lens would be ± 10 to $\pm 15^\circ$ (Agard, 1984). The sample is therefore often mounted inside a thin-walled glass capillary (Agard, 1984; Bradl *et al.*, 1992, 1994) or attached to the outside of the capillary (Kozubek *et al.*, 2002; Shaw, 1990; Shaw *et al.*, 1989). In the first case care has to be taken that the high refraction that occurs at the capillary wall is at least partially compensated by an appropriate immersion medium (usually oil). In the second case, the sample that sticks to the outside of a capillary can only be imaged from a limited range of angles to avoid the necessity

of imaging through the capillary. A two-view approach, in which the sample is rotated once by 180° has been shown to allow to compensate for attenuation in a confocal microscope (*Can et al.*, 2003).

However, practical limits and severe image registration issues have prevented widespread use of these techniques. Major limitations are the sample preparation requirements in glass and oil and the deformation of the sample during rotation. Special tilting devices have been built to adapt the technique to conventional microscopes (*Bradl et al.*, 1992). As a consequence, because of the vertical architecture of common microscope stands, the sample is rotated about a horizontal axis. The sample deforms easily as it is rotated and exposed to gravity in different orientations. These limitations can be overcome by mounting the sample in agarose and rotating the sample about a vertical axis. This is demonstrated in the Selective Plane Illumination Microscope presented in chapter 3.

A second approach to multi-view microscopy is the use of at least two objective lenses to image the sample (simultaneously) from more than one side. A low numerical aperture system ($NA = 0.4$) has been published using two orthogonally arranged objective lenses (*Kikuchi et al.*, 1997). In order to obtain isotropic resolution it is desirable to cover the full solid angle of 4π . For technical reasons one is restricted to a system that offers a limited number of views partially covering the whole sample. Ideally, the system should be laid out in a symmetric fashion that no part of the sample is particularly favored or discriminated. A set of four objective lenses arranged along the axes of a tetrahedron is presented in section 1.4. Systems that use six or more lenses are theoretically possible but practically unfeasible.

1.3 Image processing

In multi-view microscopy a set of N 3D image stacks is acquired from the same sample. To convert the data sets into a single high-resolution image stack, three steps are required:

1. preprocessing, which includes rotation, shearing, and scaling to compensate for the different orientations of the optical axes and the scan parameters,
2. registration, to align the four data stacks in 3D, and
3. fusion, i. e. selection and combination of the required information from each of the stacks.

The *first two steps* involve standard image-processing techniques and are discussed in the context of the particular experiment. They depend on the actual geometry under which the images have been taken and are therefore specific for the microscope that has been used. For the implementation of the MIAM, a four lens tetrahedral system, see section 1.5.2. The processing steps in the case of the SPIM, a single lens system in which the sample is rotated, are outlined in section 3.2.3.

For the *third step* we consider the following possible methods. The formulas describe the process of image fusion for each voxel in the stack, and must be applied to all voxels.

Arithmetic average

A very general approach to combine the data sets is to calculate the arithmetic average of the N 3D data sets (see also *Sätzler and Eils, 1997*)

$$I_{f,av} = \frac{1}{N} \sum_j^N I_j, \quad (1.13a)$$

$$\text{sequential: } I_{f,av}^{(n+1)} = \frac{1}{n+1} \left(n I_{f,av}^{(n)} + I_{n+1} \right). \quad (1.13b)$$

The sequential form can be useful if the data sets are to be combined one-by-one. This is especially useful when dealing with large data sets, e. g. when all data sets do not fit in the memory of the processing computer at once.

Maximum in Fourier space

A principal goal in multi-view combination is to preserve high resolution information from the individual raw data stacks. The final data stack should contain

as much high resolution information as the source stacks can provide. The spatial frequencies of each stack are accessible in Fourier (\mathcal{F}) space. One possible method of image combination is to pick the voxels in Fourier space that have the highest magnitude. The inverse Fourier transform yields the final image stack.

$$I_{f,w} = \mathcal{F}^{-1} \left\{ \sum_j^N w_j \tilde{I}_j \right\}, \quad (1.14a)$$

$$w_j = \begin{cases} 1, & \text{if } |\tilde{I}_j| = \max\{|\tilde{I}_1|, \dots, |\tilde{I}_N|\}, \\ 0, & \text{else} \end{cases}$$

$$\text{sequential: } I_{f,w}^{(n+1)} = \mathcal{F}^{-1} \left\{ w_n \tilde{I}_{f,w}^{(n)} + w_{n+1} \tilde{I}_{n+1} \right\}. \quad (1.14b)$$

Weighted average in Fourier space

More generally, in order to preserve all the information from the data stacks the spatial frequencies can also be weighted by their relative magnitudes (similar to *Shaw et al.* (1989)).

$$I_{f,w} = \mathcal{F}^{-1} \left\{ \sum_j^N w_j \tilde{I}_j \right\}, \quad w_j = |\tilde{I}_j| / \left(\sum_k^N |\tilde{I}_k| \right), \quad \tilde{I}_j = \mathcal{F}\{I_j\}, \quad (1.15a)$$

$$\text{sequential: } \mathcal{J}_{n+1} = \mathcal{J}_n + |\tilde{I}_{n+1}| \cdot \tilde{I}_{n+1},$$

$$\mathcal{J}_n = \sum_j^n |\tilde{I}_j| \cdot \tilde{I}_j, \quad (1.15b)$$

$$I_{f,w}^{(n+1)} = \mathcal{F}^{-1} \left\{ \mathcal{J}_{n+1} / \left(\sum_k^{n+1} |\tilde{I}_k| \right) \right\}.$$

Regarding the numerical calculations required, this method is particularly memory intensive. For a sequential fusion the intermediate result \mathcal{J}_n , the next term of the sum \mathcal{J}_{n+1} , and the normalization divisor have to be kept in memory. Once a fusion has been completed according to (1.15a) and only $I_{f,w}^{(n)}$ is known, no additional stack can be fused.

The following two methods are not robust, i. e. they are limited to special samples (e. g. isolated point objects), and can fail if there is mis-registration, spatial inhomogeneities, or noise.

Minimum

In the imaging process every point object is imaged as described by the PSF. In a second data set that has been acquired from a different angle, the PSF is most probably less extended in the former axial and more extended in the former lateral direction because of to the anisotropy of the resolution. In this case, a

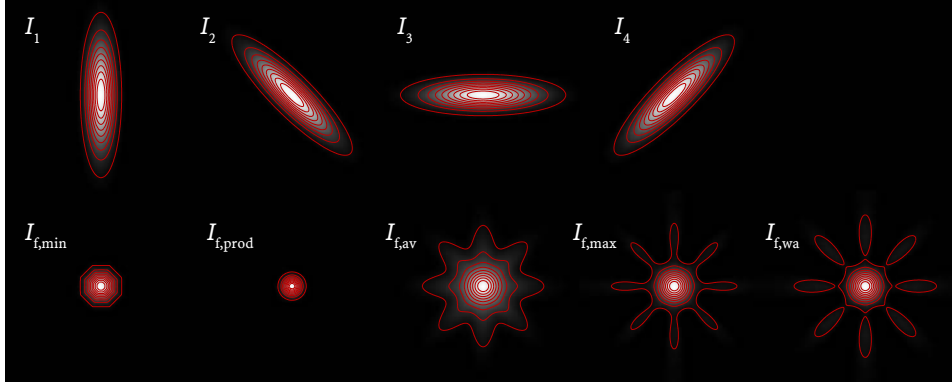


Fig. 1.8 Image fusion by different methods. Four simulated images (top row) have been fused by five different methods (bottom row). Each image has been normalized after fusion. Contour lines are spaced at 10 % steps.

possible operation is to take the minimum of the N data sets I_j for each volume element (voxel). The fused image stack I_f is build up by taking the minimum of all data sets for each voxel. This reduces the extent of such a point object to the minimum.

$$I_{f,\min} = \min \{I_1, \dots, I_j, \dots, I_N\}, \quad (1.16a)$$

$$\text{sequential: } I_{f,\min}^{(n+1)} = \min \{I_{f,\min}^{(n)}, I_{n+1}\}. \quad (1.16b)$$

Product

Another possible method is to multiply the images. The product represents the resulting image

$$I_{f,\text{prod}} = \prod_j^N I_j, \quad (1.17a)$$

$$\text{sequential: } I_{f,\text{prod}}^{(n+1)} = I_{f,\text{prod}}^{(n)} \cdot I_{n+1}. \quad (1.17b)$$

Comparison

Examples of the fusion of images by the different methods are shown in Fig. 1.8. The simulated images of a point-like bead imaged from four directions are combined. Clearly, taking the minimum of the four images results in a reduction of the point image spread, but in more complicated samples can introduce artefacts, and in addition is inherently unstable. Taking the product reduces the extent of the spot significantly. However, this method only works on point-like objects that are well-separated and of equal brightness. Moreover, for the purpose

of iterative stability it is desirable that the fusion of any two identical images is simply the original image. The product is the only one of the fusion methods discussed here that fails in this respect.

The arithmetic average can be obtained at high speed. However, clearly no weighting is performed and the high resolution of one stack in a particular direction is suppressed by the potentially low resolution of the other stacks in this direction. Because they yield smaller point images, the Fourier based methods are clearly advantageous in this respect, although they are by far the slowest of all the presented methods. In this example both perform nearly equally, but the maximum method is simpler and fully recursive. Although it is less resistant to noise, the maximum method gives a better resolution than the weighting method in low-noise images.

The test pattern shown in Fig. 1.9 was computationally convolved with the same four PSFs as in Fig. 1.8. The four fusion methods (minimum, average, maximum and weighted average in Fourier space) were applied to the blurred data. Clearly, taking the minimum completely fails on this sample and taking the average results in a strongly blurry image. The Fourier space based method are clearly advantages and reproduce the original sample quite well.

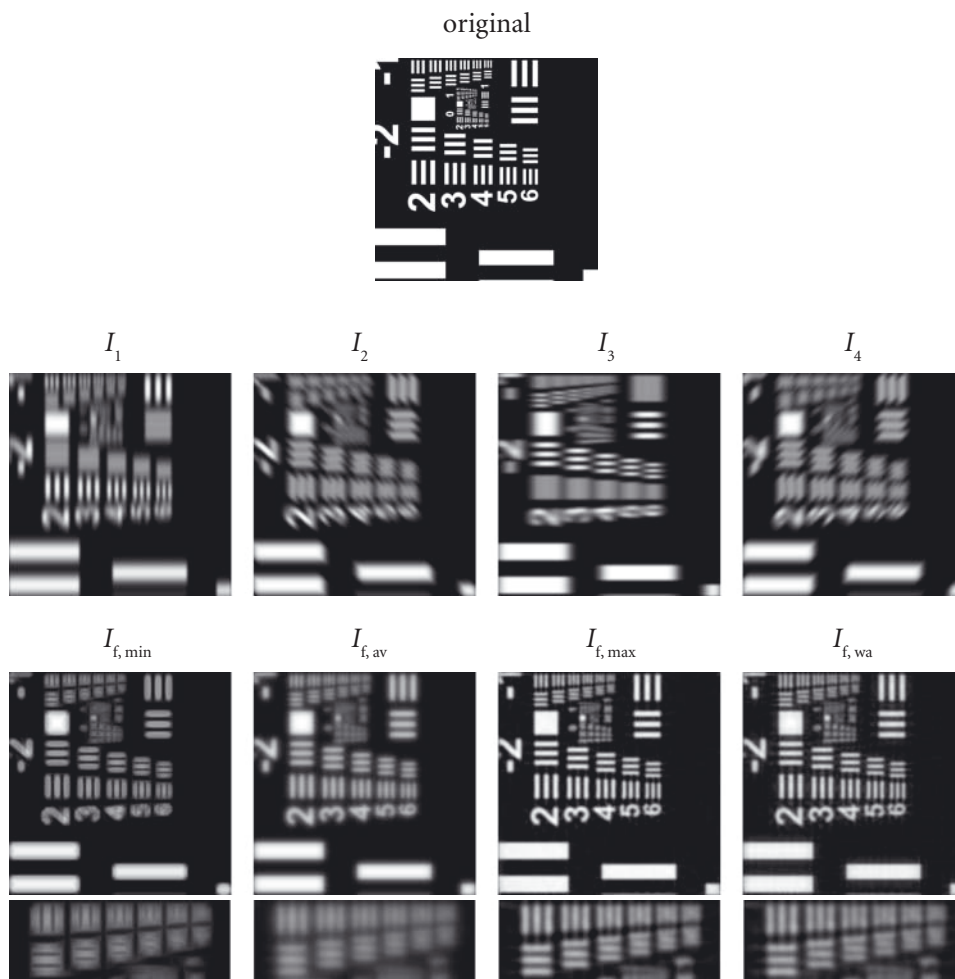


Fig. 1.9 Test pattern (top) blurred with the four PSF from Fig. 1.8 (middle row) and then combined with four different methods (bottom row). One area from the top has been enlarged and is shown for the four fused images.

1.4 The tetrahedral multi-imaging axis microscope

This section describes the geometry and the setup of such a microscope. The multi-imaging axis microscope (MIAM) is the realization of a widefield microscope in which four views of the sample are combined for improved resolution. It is characterized by

Tetrahedral multi-imaging axis microscope

1. four objective lenses for illumination and/or detection,
2. uniform illumination,
3. widefield detection (four cameras) and image combination.

1.4.1 Design

Let us consider a microscope consisting of four objective lenses. Each objective lens can be used for illumination and/or detection and all lenses have the same common focus. All lenses are equal and are symmetrically distributed around the common focus such that they are spaced by the same angle. Let the objectives be represented by vectors $\hat{\mathbf{a}}_i$, ($i = 1, \dots, 4$) that point to the common center. These vectors are normalized, so that

$$|\hat{\mathbf{a}}_i| = 1. \quad (1.18)$$

Due to the symmetry of the arrangement the vector sum of the four is

$$\sum_i \hat{\mathbf{a}}_i = \mathbf{0}. \quad (1.19)$$

The angle between the objectives is ϑ , which is given by the relationship

$$\hat{\mathbf{a}}_i \cdot \hat{\mathbf{a}}_j = \cos \vartheta \quad \text{for} \quad i \neq j. \quad (1.20)$$

By multiplying (1.19) with $\hat{\mathbf{a}}_1$, we find that

$$\hat{\mathbf{a}}_1 \cdot \sum_i \hat{\mathbf{a}}_i = 1 + 3 \cos \vartheta = \hat{\mathbf{a}}_1 \cdot \mathbf{0} = 0 \quad (1.21)$$

$$\Rightarrow \boxed{\cos \vartheta = -\frac{1}{3}} \Rightarrow \vartheta \approx 109.47^\circ. \quad (1.22)$$

This is the angle between two symmetry axes of a tetrahedron.

To describe the microscope, the following right-handed coordinate system has been set up (see Fig. 1.10): The objectives have been labelled 1–4 and the x -axis is horizontal and has been chosen to be parallel to the vertical plane containing

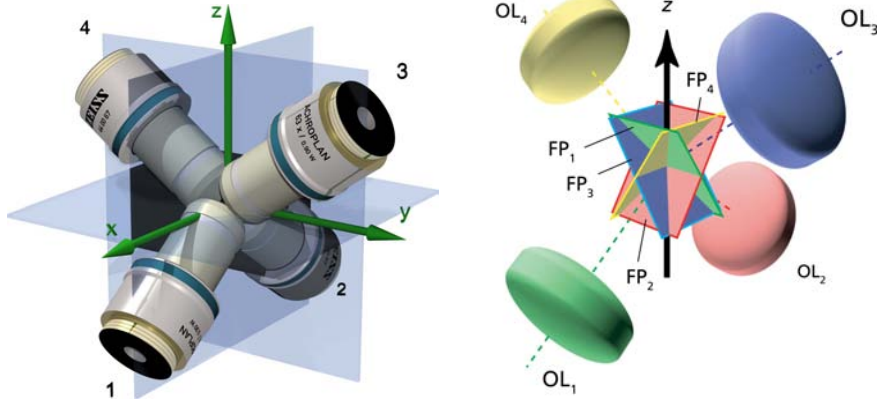


Fig. 1.10 A multi-view microscope consisting of four objective lenses (computer rendering). The objective lenses 1–4 are distributed such that each is separated from the others by the angle $\vartheta = \arccos(-1/3)$. The optical axes are oriented along the axes of a tetrahedron. Objective 1 and 2 are chosen to be in the x - z -plane, Objective 3 and 4 are in the y - z -plane. The focal planes FP_{1-4} intersect in a single point in the center of the arrangement.

the axes of objectives 1 and 2. The y -axis lies in the horizontal plane so that the z -axis points upwards.

In this coordinate system the objectives point in the following directions:

$$\hat{\mathbf{a}}_1 = \left(-\sqrt{\frac{2}{3}}, 0, \sqrt{\frac{1}{3}}\right), \quad (1.23a)$$

$$\hat{\mathbf{a}}_2 = \left(\sqrt{\frac{2}{3}}, 0, \sqrt{\frac{1}{3}}\right), \quad (1.23b)$$

$$\hat{\mathbf{a}}_3 = \left(0, -\sqrt{\frac{2}{3}}, -\sqrt{\frac{1}{3}}\right), \quad (1.23c)$$

$$\hat{\mathbf{a}}_4 = \left(0, \sqrt{\frac{2}{3}}, -\sqrt{\frac{1}{3}}\right). \quad (1.23d)$$

In such a setup the four objectives are arranged along the axes of a tetrahedron (Fig. 1.10).

1.4.2 Setup

The multi-imaging axis microscope (MIAM) presented in this work uses four identical objective lenses, Zeiss Achroplan 63 \times , 0.9 W. They are arranged symmetrically along the axes of a tetrahedron, i. e. all objectives contribute equally to the final image. The geometry of such a system has been discussed in the previous section. The system is specifically designed to be used with water (or other aqueous media) as its immersion medium. The Zeiss Achroplan series is

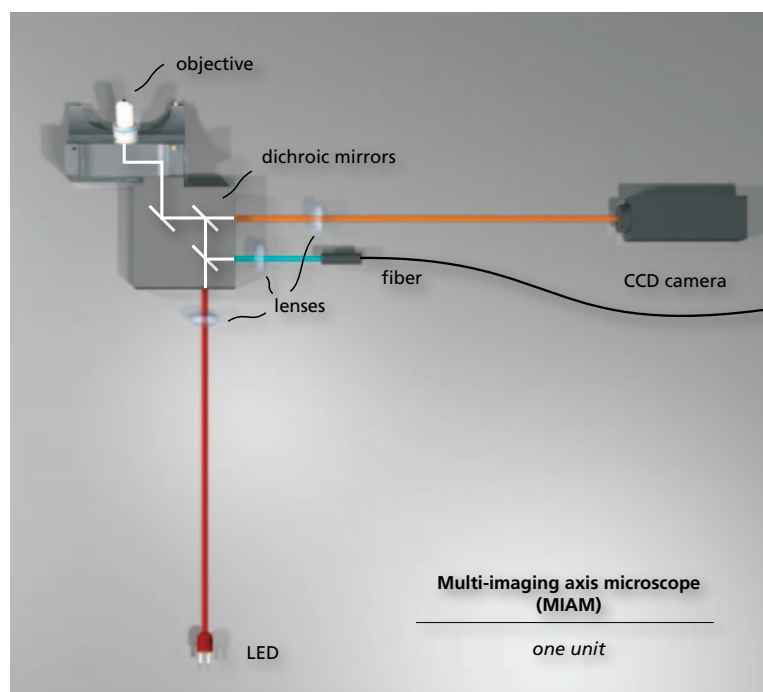


Fig. 1.11 One unit of the multi imaging axis microscope. For fluorescence excitation, the light from a laser (not shown) is directed into the objective by a fiber, a lens and (dichroic) mirrors. The fluorescence light that is collected by the objective is separated from the excitation light by dichroic mirrors and a filter and is imaged onto the camera. For scattering contrast a red LED is available. For a detailed list of components see the appendix.

corrected to be used without a cover slip in direct contact with water (“dipping lenses”). The Achroplan series magnification ranges from $10\times$ to $100\times$. The $63\times$ lens was chosen because it provides a large NA in a dipping water-immersion lens with sufficient working distance (1.5 mm) to fit in the tetrahedral geometry. Objective lenses by other companies have similar characteristics. The use of a water-dipping lens is essential in the MIAM because it allows observation in a biologically relevant environment with minimal optical distortions and because standard coverslips are not well suited to the objective lens arrangement.

Associated with each objective lens are the optics and CCD camera required to form four simultaneous fluorescence images of the sample. Fig. 1.11 shows one of the four units. Each unit represents a (fluorescence) widefield microscope. In addition to excitation light source, collimation lens, dichroic mirror, objective lens, emission filter, tube lens, and camera it consists of some extra mirrors to guide the light into the objective.

In a separate section connected to the four objective units by the optical fibers (see appendix), the 488-nm emission of an argon-ion laser and the 543-nm emis-

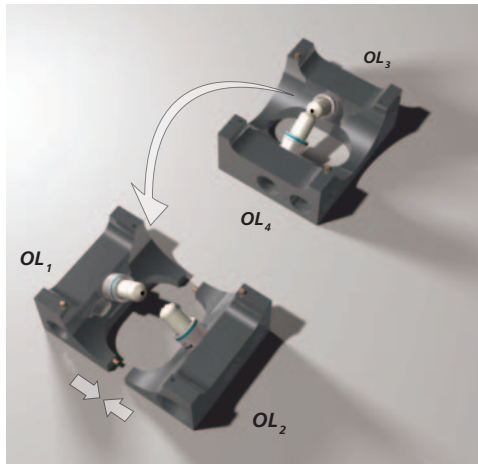


Fig. 1.12 The core of the microscope consists of four identical parts that hold the objectives in place. When assembled the objectives are oriented along the axes of a tetrahedron as illustrated in Fig. 1.10.

sion of an helium-neon laser are split into four beams of equal intensity. Each beam can be attenuated by an acusto-optical tunable filter (AOTF) and is coupled into the microscope through optical fibers (see appendix). The beam is collimated to illuminate the entire field of view of the objectives. Using the AOTFs, the intensity of illumination can be adjusted for each objective lens independently and at high speed (tuning time $< 4.5 \mu\text{s}$).

Each objective lens is held in a metallic block that ensures the correct angle of $\theta/2 = 54.7^\circ$ relative to the vertical z -axis. The core of the microscope is assembled by attaching four of these units (Fig. 1.12). In this manner, the correct orientation of the objective lenses and the stability of the most sensitive parts are ensured. Because of the symmetry of the system, all units and the associated optics are identical. Fig. 1.13 shows the layout of the system on an optical bench. Some beam paths, however, are folded with extra mirrors (omitted in the figure) to fit the setup on the bench. For a list of components, drawings, and photographs see the appendix.

The system is aligned such that the fields of view of the cameras overlap to the maximum extent. To achieve this, all cameras are rotated so that the projection of the z -axis is parallel to the long axis of the field of view (see Fig. 1.10). The focal planes intersect at one point at the physical center of the tetrahedron. This is illustrated for one objective in Fig. 1.14. For this photograph the excitation light was collimated as it enters the objective. The focus is clearly visible in the fluorescent drop between the two lenses.

It is clear from Fig. 1.10 that at any given time the four cameras will focus on different planes in the sample (i. e. the focal planes only coincide at one point). However, scanning the sample allows the entire sample to be translated through all four focal planes, and thus imaged in 3D in its entirety by all four cameras.

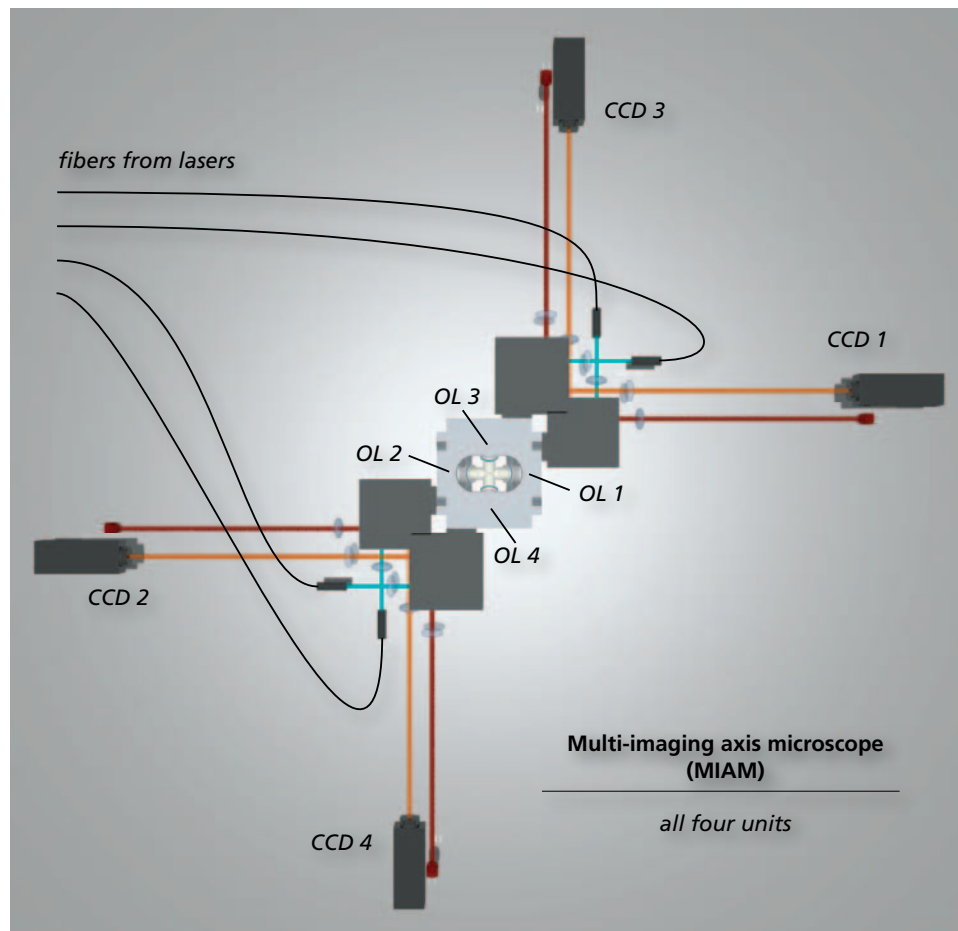


Fig. 1.13 Multi-imaging axis microscope. The four arms are arranged around the four objectives in a symmetric fashion.

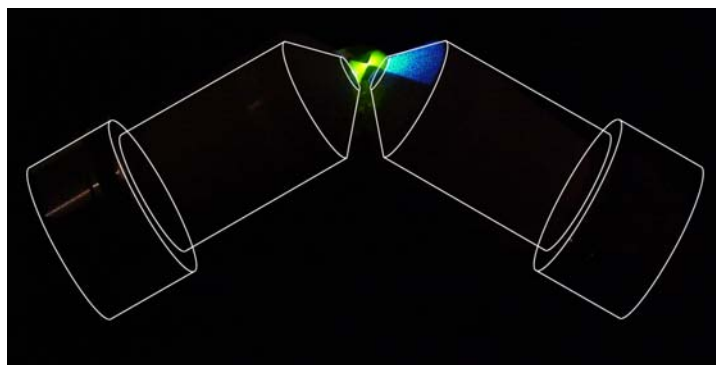


Fig. 1.14 Alignment of the first two units. The focus of one objective lens is clearly visible in this photograph (in the center of the drop of fluorescent dye). The orientation of the two lenses is outlined.

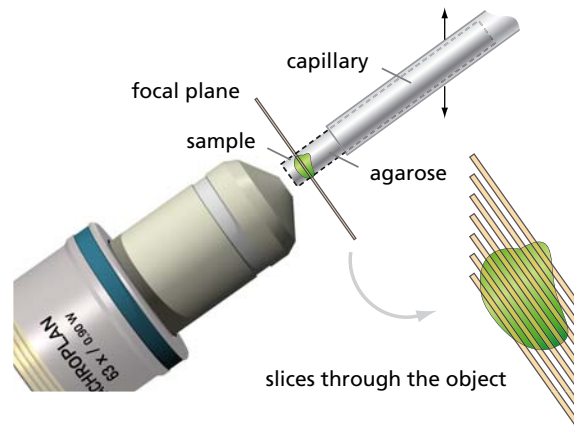


Fig. 1.15 The space opposite to objective no. 2 (other lenses omitted) is used to insert a capillary into the sample region between the lenses. The sample is embedded in a cylinder of agarose gel that is pushed out of the capillary. To acquire four complete three-dimensional stacks of the sample it is translated in the vertical direction (z -axis). In this illustration the capillary is shown not to scale (actual diameter of the agarose is $300\text{ }\mu\text{m}$).

1.5 Experimental methods and results

This section explains the processes of sample preparation, image acquisition, and image preprocessing necessary to get a three dimensional image of a sample. The resolution improvement in the MIAM by multi-view combination is demonstrated with a test sample.

1.5.1 Sample preparation

Obviously no conventional sample preparation on a cover slip is applicable in a multi-lens system such as the MIAM. However, the space between the lenses is about 3 mm in diameter, which leaves enough space for a micro capillary to be moved close to the focal planes of the objectives. The sample is embedded in an agarose gel. The solidified gel, which is $\approx 300\text{ }\mu\text{m}$ in diameter, is extruded from the capillary, so that the sample can be imaged free of an extra glass interface that can introduce severe distortions. The agarose is prepared at very low concentrations and its optical properties, i. e. its refractive index, are therefore nearly identical to water. Distortions due to the sample supporting material and mounting medium are minimal.

The sample embedded in the agarose and held by a micro-capillary can be translated in three dimensions with a mechanical stage. The capillary is moved close to the center of the lens arrangement and enough agarose is pushed out of the capillary to permit a unhindered view of the sample. The field of view of each

lens is about $40\text{ }\mu\text{m} \times 50\text{ }\mu\text{m}$. For samples in this size regime a maximum travel of $\approx 100\text{ }\mu\text{m}$ is sufficient to move the sample through the focal planes. This is performed in a precise manner with a piezo stage. The z -axis (see Fig. 1.10) has been chosen for the direction of this translation.

The sample is imaged in the MIAM with all four lenses simultaneously. It is moved through the focal planes in a stepwise fashion along z . After each step the illumination light (laser light for fluorescence excitation or LED for scattering contrast) is turned on and all cameras are triggered to acquire an image. Immediately after acquisition the illumination light is turned off to minimize exposure of the sample.

The cameras acquire images at a maximum rate of about seven frames per second. During stack acquisition the frame rate is limited by the stage speed, resulting in a frame rate of 1–2 frames per second. The 8-bit images of all cameras are saved to disk upon acquisition.

1.5.2 Data pre-processing

For the acquisition of a three-dimensional stack, the sample in the MIAM is not moved along the optical axis of the objective lens like as is usually done in microscopy. The direction of translation (z -axis) intersects with the optical axes 1–4 at an angle of $\theta/2 \approx 54.7^\circ$. Hence, a translation of Δz along the z -axis corresponds to movement of $\Delta z \cdot \cos(\theta/2)$ along the axial and of $\Delta z \cdot \sin(\theta/2)$ along the lateral direction of each lens. This means that the raw data appears to be sheared as illustrated in Fig. 1.15. In addition, the sample that is scanned along $+z$ is moved away from objectives lenses 1 and 2 and is moved towards objectives 3 and 4.

After this the four data sets are scaled to have identical pixel sizes in all three dimensions. The image stacks are all rotated so that the stacks extend along the z -axis. Finally, the data set are registered by performing a correlation. The elementary preprocessing steps that are performed on the data taken with the MIAM (see Fig. 1.16) are summarized in table 1.1.

The sample used here to illustrate the resolution-improving ability of the MIAM is a suspension of 200 nm fluorescent latex beads in a cylinder of agarose gel. Latex beads of this size represent a well-defined test sample commonly used to investigate the performance of microscopes. Figure 1.17(a) shows a projection of the raw 3D data stack from camera 1, which consisted of 400 slices of 960×1280 pixels with an approximate volume of $40\text{ }\mu\text{m} \times 50\text{ }\mu\text{m} \times 100\text{ }\mu\text{m}$. Figures 1.17(b)–(e) show subvolumes of Fig. 1.17(a), containing 12 beads each, as viewed by the four cameras. It is clear that the images of the beads are axially elongated and that the anisotropy of the resulting resolution is different for each camera.

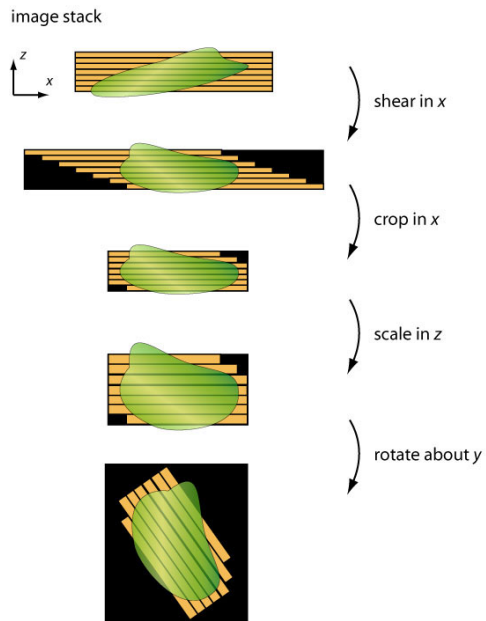


Fig. 1.16 Summary of the pre-processing steps performed with each stack from the MIAM. The data is sheared, scaled, and rotated. To reduce the processing time the stacks are cropped wherever possible.

	CCD ₁	CCD ₂	CCD ₃	CCD ₄
1. frame order	reverse		normal	
2. crop array				
3. normalize whole array				
4. turn array				
5. shear array	-4.035		+4.035	
6. crop array				
7. scale array				
8. rotation about z by	-54.74°		-(180° - 54.74°)	
9. turn array				
10. rotate about z by	0°	180°	-90°	+90°
11. registration				
12. fusion				

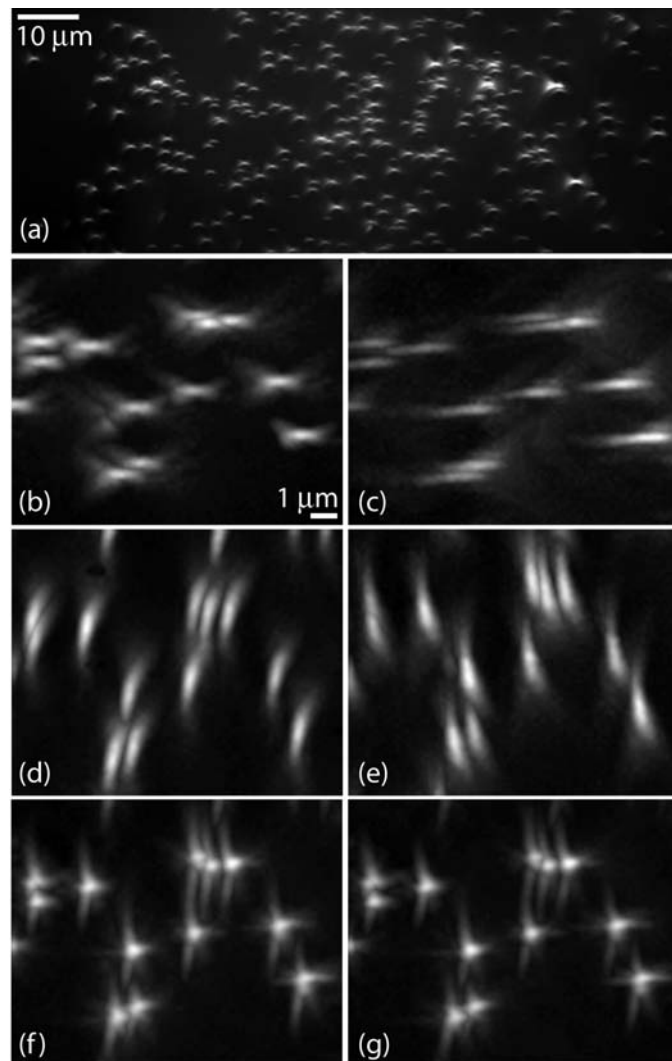


Fig. 1.17 Maximum-value projections, 200-nm fluorescent beads. (a) Large field-of-view image, CCD 1. (b), (c), (d), and (e) Cropped images of CCDs 1, 2, 3, and 4, respectively. Fusions of data from (b)–(e) by (f) arithmetic average and (g) weighted average are also shown. *Swoger et al.* (2003)

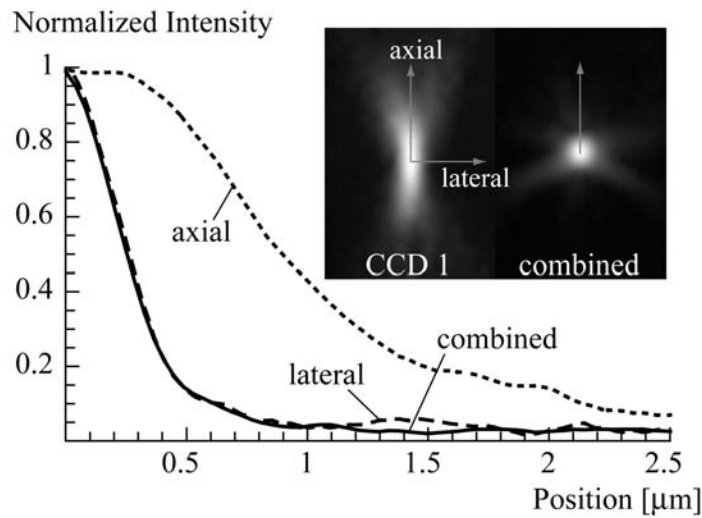


Fig. 1.18 Line scans through 3D stacks of a 200-nm bead. Dashed curves CCD 1. Solid curves, weighted-average fusion image. Inset, projections (perpendicular to optical axis of CCD 1) from CCD 1 and the fusion data set; arrows indicate line scan directions. *Swoger et al. (2003)*

1.5.3 Data fusion

The arithmetic-average fusion of the four single-lens data sets is shown in Fig. 1.17(f), and the weighted average is in Fig. 1.17(g). With both methods the bead images are clearly more symmetric than any of the single-camera images in Figs. 1.17(b)–(e): The axial elongation of the bead images has been eliminated. It must be emphasized that, although Fig. 1.17 shows projections along only a single direction, the observed isotropy is actually a 3D property of the fused images. A small improvement in the resolution is attained by use of the more computationally demanding weighted average.

To further illustrate the resolution improvement that the MIAM can provide, line plots through the images of one of the beads are shown in Fig. 1.18. Here the combined and lateral single-lens line plots are virtually identical, but the axial elongation is eliminated by the fusion of the four views. To determine the actual resolution of the images, one must correct for the size of the bead. To first order this can be done by subtracting the bead diameter (200 nm) from the measured image widths; the resulting resolutions of the different MIAM modes are listed in Table 1.2. The size of the single-lens and fusion PSFs' FWHM are shown, as well as the relative resolution gains that the MIAM provides. As expected from Fig. 1.17, this quantification shows that the arithmetic average yields results similar to, but slightly worse than, the weighted average. With the weighted-average fusion the isotropic resolution is slightly inferior to the lateral resolution measured for a single lens; however, this is more than compensated for by the dramatic de-

Table 1.2 Resolution and Gain^a. *Swoger et al.* (2003)

Method	Lateral	Axial	Volume
Theoretical FWHM			
Single lens	303 nm	1340 nm	64 aL ^c
Experimental FWHM			
Single lens ^b	257 nm	1927 nm	68 aL
Arithmetic	359 nm	359 nm	24 aL
Weighted	334 nm	334 nm	19 aL
Experimental Resolution Gains ^a			
Arithmetic	0.72	5.4	2.8
Weighted	0.77	5.8	3.5

^a $\text{FWHM}(\text{PSF}_{\text{singlecamera}})/\text{FWHM}(\text{PSF}_{\text{fusion}})$.

^b Mean, cameras 1–4.

^c 1 aL=10⁻¹⁸L.

crease in the axial elongation (a factor of 5.8), yielding a gain in the volume resolution of 3.5 \times .

No image restoration or deconvolution has been performed on the data presented. Since the fusion methods described in this work retain the linear, spatially invariant properties of the single-camera images, application of appropriate deconvolution algorithms should provide further significant increase in the resolution of the MIAM.

In conclusion, the data presented in this chapter demonstrate that the MIAM can be an extremely effective technique for imaging fluorescent samples that are at least as thick as 300 μm , with a volumetric increase in resolution by a factor of at least 3.5, compared with the equivalent single-lens system, and an essentially isotropic PSF. The combination of MIAM imaging with optical trapping and manipulation is described in the next chapter.

2. The Differential Active Optical Manipulator

In classical optical microscopy the sample under investigation is spatially fixed between a glass slide and a cover slip. This mounting procedure is adequate for cell cultures in which the cells grow on cover slips and are already in contact with a glass interface. However, these cells are kept under artificial conditions that do not represent the conditions found in tissue where cells are surrounded by other cells. Therefore it is doubtful whether some results obtained from cultured cells are applicable to cells as components of tissues and organisms.

Contemporary biological experiments increasingly demand configurations in which the sample is kept under physiologically relevant conditions. This could e. g. be realized by embedding the sample in an appropriate scaffold (see chapter 3) or by having the sample freely floating in a liquid medium rather than stuck to a coverslip. Such systems are applicable to single cells, tissues, and whole embryos. There is still a requirement for a means to confine and translate the sample in a microscope in which the sample floats and is not mechanically fixed. It has been shown that such tasks can be performed gently by applying optical forces (Ashkin, 1997). Optical tweezers (Ashkin *et al.*, 1986), including the recently developed dynamic multiple-beam optical tweezers (Grier, 2003), have been shown to be valuable tools in several fields.

The *Differential Active Optical Manipulator (DAOM)* (Huisken *et al.*, 2004c) presented in this chapter utilizes four collimated laser beams arranged along the axes of a tetrahedron to confine and move a microscopic sample in an aqueous medium. The DAOM makes use of a distinctive advantage of collimated light: in contrast to optical tweezers, this instrument allows movement of the confined particle over long distances without mechanical scanning. Only scattering forces are exploited to provide ultra-long working distances. The optical Earnshaw theorem (Ashkin and Gordon, 1983), which states that a small particle cannot be trapped solely by scattering forces, is overcome by introducing a feedback system. The beams' forces superimpose in their common volume, and the total force (magnitude and direction) on the particle can be set by adjusting the beams' intensities. This can be done quickly and independently for each beam.

As a demonstration, latex beads (20 μm in diameter) are moved across the whole field of view of the MIAM using 100 μm diameter beams. Active and automated

feedback can be implemented to ensure that the sample is held in place or transported to a specified position as desired. This allows focusing and lateral translation of the microscopic sample, which are common tasks in microscopy.

Because the system is realized in the framework of the MIAM, which has been introduced in the previous chapter, the sample is observed from four directions simultaneously. This demonstrates the instrument's potential as a universal manipulator in connection with high-resolution isotropic light microscopy.

In the following, the forces in collimated beams are explained and the use of the tetrahedral arrangement is motivated. The optical forces in such a four beam manipulator are calculated, the experimental setup is presented and recorded video sequences are analyzed and discussed.

2.1 Optical manipulation

2.1.1 Introduction

Various techniques of optical manipulation have found widespread use in the past decades: from the first experiments by *Ashkin* (1970) demonstrating that laser light can exert forces on dielectric particles, to routinely applied optical tweezers (*Ashkin et al.*, 1986). The applications are wide-spread, ranging from molecular biology and single molecule experiments to sorting devices and microscopic machines and motors (*Ashkin*, 1997). All instruments that exploit optical forces make use of a laser as the light source. However, the laser light can be manipulated in various ways to generate the desired optical trap.

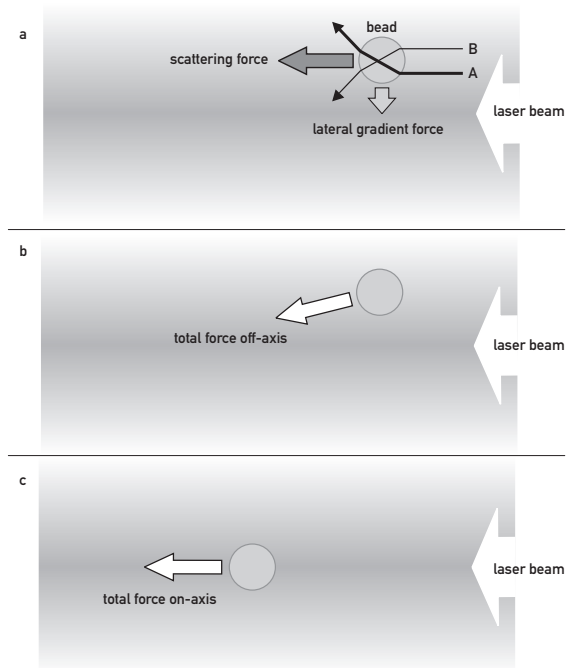
Generally, one can distinguish between (1) instruments exploiting only the axial scattering force to confine a sample and (2) instruments that in addition provide an axial gradient force that is present in highly focused beams to form a stable 3D trap. The first group of experiments includes “optical levitation” (*Ashkin and Dziedzic*, 1971) and “optical guiding” (*Gauthier and Frangioudakis*, 2000); the second group refers to “optical tweezers” or “single-beam gradient traps” (*Ashkin et al.*, 1986). Optical tweezers were invented because the single weakly focused laser beam in levitation experiments can only trap particles in 2D. However, as shown in this work, multi-beam arrangements can compensate for this deficit, thereby opening new perspectives and allowing exploration of new areas of optical manipulation.

In any beam of light, optical forces arise as soon as the light is scattered at an object exposed to the beam. Depending on the presence of local gradients a dielectric particle experiences different forces.

2.1.2 Collimated beams

Optical forces can be demonstrated using a collimated or weakly focused laser beam: a particle with a higher refractive index than the surrounding medium (which we will always assume in the following) is confined to the optical axis and pushed along the beam (*Ashkin*, 1970). Looking at a bead placed off-axis in a Gaussian laser beam (Fig. 2.1) we see that axial scattering and lateral gradient forces are responsible for this phenomenon. Any scattering of the light at the particle will exert a force along the beam’s axis. Lateral gradients, e. g. in case of a Gaussian intensity profile, give rise to an additional force component pointing towards the beam’s axis. The momentum transfer by a ray bundle close to the axis (A in Fig. 2.1a) is higher than one by a ray bundle that is farther away from the beam (and therefore less intense, B). The resulting total force is directed along the beam and towards the beam’s axis (Fig. 2.1b). Once the particle

Fig. 2.1 Forces present in collimated beams. a: A bead in a collimated laser beam experiences two optical forces: the scattering force pushing the particle along the beam and the (much weaker) lateral gradient force, which is present if there is a lateral gradient in the beam. b: The total force acting on the particle pushes the bead along the beam and towards the beam's axis. c: If the particle is on-axis only the scattering force is present. By varying the laser intensity the strength of the optical forces can be varied. (In this figure it is assumed that there are no external forces like gravity or buoyancy. The refractive index of the bead is higher than the refractive index of the surrounding medium.) *Huisken et al.* (2004a)



has reached the axis, it is pushed along the beam. This holds true as long as lateral confinement is strong enough to keep the particle on-axis. Under these circumstances a particle can be moved along any desired distance.

Note that this single beam does not yet act as an optical trap. The particle is confined on the optical axis (i. e. two-dimensionally confined), but can still move along the beam.

2.1.3 Optical levitation and active feedback

Optical levitation (*Ashkin and Dziedzic, 1971*) can be performed by directing the beam upwards. In this case the scattering force is anti-parallel to and counteracted by gravity (see Fig. 2.2a). If the laser beam is intense enough to overcome gravity the particle will be levitated. Depending on the laser power, optical properties, position, and density of the particle it will rise, sink or remain at rest.

By making the beam slightly diverging one can provide a range of intensities and a particle introduced to the system above the focus will come to rest where optical forces cancel gravity. The trap is now stable in the sense that any excursion from the rest position, either laterally or axially, will give rise to optical forces pushing the particle back to the potential minimum. These experiments are mostly performed in air, where buoyancy is negligible. The laser beam is focused by a long focal length lens into a glass chamber, which helps to reduce air flow. Particles can be injected into the beam from above and will come to rest

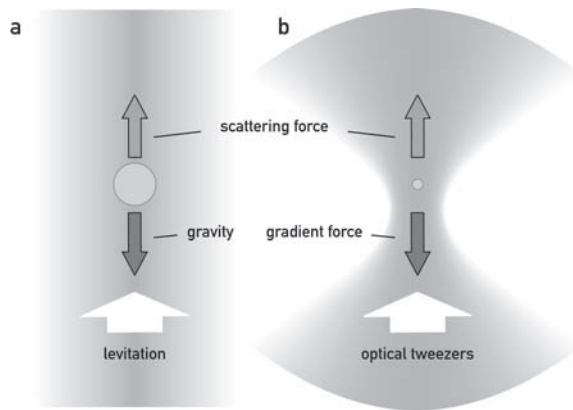


Fig. 2.2 a: Optical levitation. The particle is axially confined by a balance of optical scattering forces and gravity. Laterally an intensity gradient ensures on-axis position. b: Optical Tweezers. In the tight focus of the laser beam gradient forces pull the particle into the focus: the particle is trapped near the focus. *Huiskens et al. (2004a)*

above the focus (*Huiskens, 2000; Huiskens et al., 2002*).

Another way to trap, i. e. three-dimensionally confine, samples is by actively adjusting laser power of an upwards directed beam. By this method the particle can also be moved along the beam in a controlled fashion (*Ashkin and Dziedzic, 1976*). Detection of the particle position facilitates automatic implementation of such system. However, the system still relies on gravity. The maximum downward force is that due to gravity (when the beam is switched off) and the particle sinks freely. This generally makes this kind of trap fragile in the axial direction.

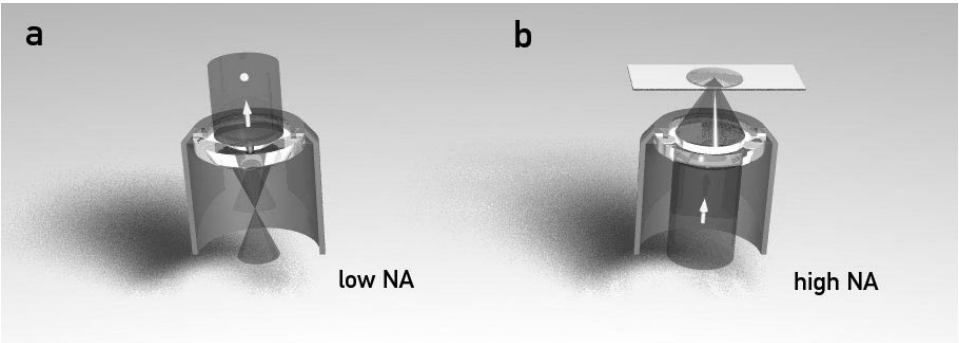
2.1.4 Optical Tweezers

Things change when the laser beam is strongly focused. Now axial gradient forces can become strong enough to counteract the scattering forces (Fig. 2.2b). This results in a stable three-dimensional trap (*optical tweezers, Ashkin et al. (1986)*) that is completely independent of gravity. Therefore it is also called single-beam gradient trap, and is usually operated in aqueous medium where gravitational effects are negligible. The particle is trapped in a position shortly behind the focus where the forward directed scattering force is balanced by the gradient force, which is directed towards areas of higher intensities.

In contrast to optical levitation, the particle is trapped in a fixed volume close to the focus. The particle cannot be moved by simply changing the laser power. In optical tweezers, increasing the intensity strengthens the trap and reduces the trapping volume, whereas decreasing the power enlarges it. Lateral movement of the sample can be performed by scanning the beam. Axial movement can be induced when the focus is moved axially by shaping the beam appropriately in the objective back focal plane. The range over which this can be done is limited by the aberrations that become pronounced when using the objective to trap away from the designed focal plane. Usually this distance is in the order of $40\ \mu\text{m}$ (*Sinclair et al., 2004*).

Table 2.1 Comparison: Optical Guiding (a) vs. Optical tweezers (b). *Huisken et al.* (2004a)

a) All-Optical Guiding	b) Optical Tweezers
collimated beam	strongly focused beam (high NA lens)
no / weak axial gradient	high axial gradient
only lateral confinement	three-dimensional trap
particles can be moved over any distance	small distances
changes in intensity can reposition particle	beam or objective has to be moved



Back focal plane beam shaping is done in holographic tweezers with spatial light modulators (*Curtis et al.*, 2002; *Rodrigo et al.*, 2002). These devices impose a phase shift at each pixel in an array. A precalculated phase pattern can then: create a trap at a defined position, create a whole array of traps, or move a trap across the field of view when the pattern is changed. However, the distances over which a sample can be moved is limited by the resolution of the spatial light modulator and is usually in the order of 50 μm (*Sinclair et al.*, 2004). Again, the axial distance is limited by the performance of the objective lens away from the focal plane. Because the underlying basis is still the gradient force trap, a high NA lens with its intrinsic short working distance is essential.

An optical manipulator for microscopy that can be used to translate the sample under observation should feature the following: a long working distance (to be capable to handle large samples); sufficient lateral working range (the distances over which samples can be transported should be large and span at least the full field of view); the axial travel range should be at least large enough to move the whole sample of interest through the focal plane; any translation should be fast and precise, ideally without mechanical movement of any part of the microscope. Often the ability to trap several particles at once is not needed, and therefore, keeping the features mentioned above in mind, a solution based on low NA lenses utilizing weakly focused beams is favorable. A summarizing comparison of optical guiding and optical tweezers is shown in Table 2.1.

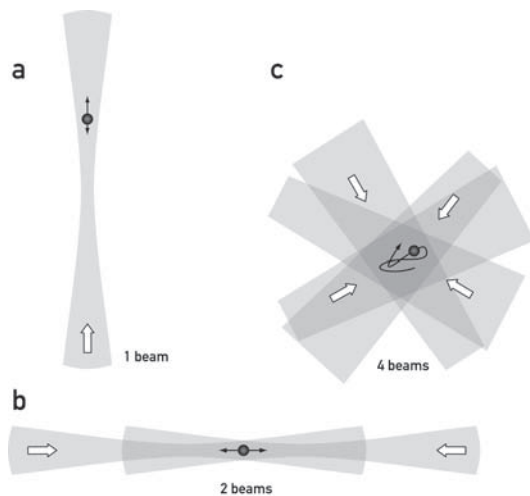


Fig. 2.3 Optical levitation and multi-beam traps. a: A vertically directed single laser beam can be used to confine microscopic particles. The particle is levitated by a balance of optical forces and gravity. b: Two counter-propagating beams trap particles in the central region between the two foci. The trapped particle can be moved along the common axis. c: In the DAOM four collimated laser beams allow full three dimensional manipulation within the volume of intersection. *Huiskens et al. (2004a)*

2.1.5 Multi-beam arrangements

Using a single laser beam a particle can be confined on the optical axis (Fig. 2.3a). The scattering force is directed along the beam and can be varied by adjusting the beam's power. This can be done quickly and precisely with acusto-optic modulators (AOM). Particles can be moved over very large distances (several mm) as long as lateral stability is provided.

A stable and flexible horizontal trap, however, can only be achieved by using more than one collimated beam. Two counter-propagating beams (Fig. 2.3b) can be used to transport a particle along their common axis (*Ashkin, 1970*). The scattering forces generated by the beams are balanced at a point between their foci; lateral stability is obtained by a strong lateral gradient, as in levitation. One- and two-dimensional manipulation has been achieved by utilizing the diverging beams from optical fibers (*Collins et al., 1999*).

A two-beam trap was realized using two fibers that guide light of a 1064 nm laser. Figure 2.4 shows a photograph of the setup. Two 20× microscope objective lenses were used to focus the laser light into the chamber. The beams are adjusted to counter-propagate with their foci being a few hundred micrometers apart. By modulating the intensity of one or both of the beams it was possible to move 10–30 μm glass beads along the common beam axis. The results confirm the observations of *Ashkin (1970)*.

A feature common to all of the above techniques is that they rely on lateral optical intensity gradients to provide stable traps. By varying the intensities of the beams the axial position of the particle can be set. Laterally the particle is confined on the axis, the lateral forces being dependent on the beam profile, intensity, and the particle size.

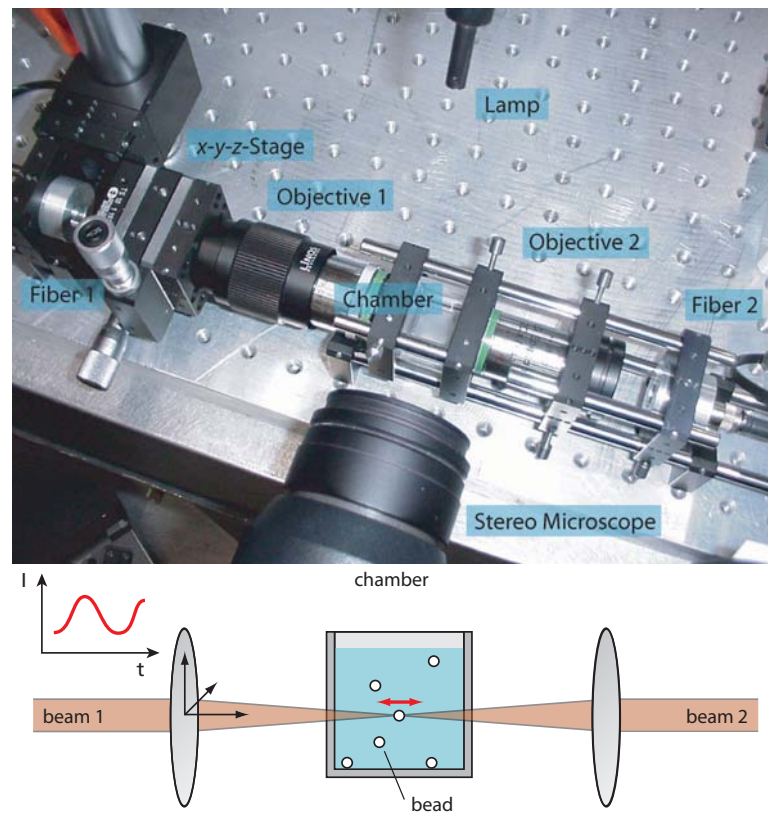


Fig. 2.4 Setup of a two-beam trap. The laser light emanating from the two fibers is collimated by lenses and focused by microscope objective lenses into a chamber. The beams are aligned such that they counter-propagate and that their foci are a few hundred microns apart. A particle can be trapped between the foci and moved along the beams' common axis.

For a three-dimensional manipulator that relies only on scattering forces, the minimum requirement for stability is a set of four beams (Fig. 2.3c), although for the one-dimensional case alternating beams have been demonstrated to create a temporal gradient sufficient to passively trap a particle at a fixed location (Ashkin and Dziedzic, 1985). A tetrahedral geometry has been proposed as a trap for atoms (Minogin, 1982), but was soon declared to be unfeasible. According to the *optical Earnshaw theorem* (Ashkin and Gordon, 1983), a small dielectric particle cannot be trapped using only the scattering force of optical radiation. In this work it is demonstrated that this restriction can be overcome, and that microscopic objects can be confined and moved in a controlled fashion by introducing a feedback system that controls the powers of the beams.

The *Differential Active Optical Manipulator (DAOM)* presented here does not require high NA objectives: in fact, the intensities gradients are deliberately minimized so that there is no location at which passive stable trapping can occur. In such a system, varying the intensities of the four beams independently allows adjustment of the direction and magnitude of the optical scattering forces acting on the sample. This, coupled with a 3D position sensor that feeds back to control the beam intensities, allows arbitrary active positioning of the sample. In consequence, a particle can be moved in 3D over distances limited only by the beam diameters and the field of view of the position sensor.

In the DAOM the four beams are arranged along the axes of a tetrahedron and are collimated in their volume of intersection. The optical forces generated by the beams add in their common volume (see Fig. 2.5) and the total force (magnitude and direction) acting on the sample is set by adjusting the intensities of the beams. This offers the possibility of moving the sample along arbitrary paths within a volume of about $100\,\mu\text{m} \times 100\,\mu\text{m} \times 100\,\mu\text{m} = 1\,\text{nL}$. Focusing and lateral translation of the microscopic sample, which are common tasks in three-dimensional light microscopy, are easily implemented.

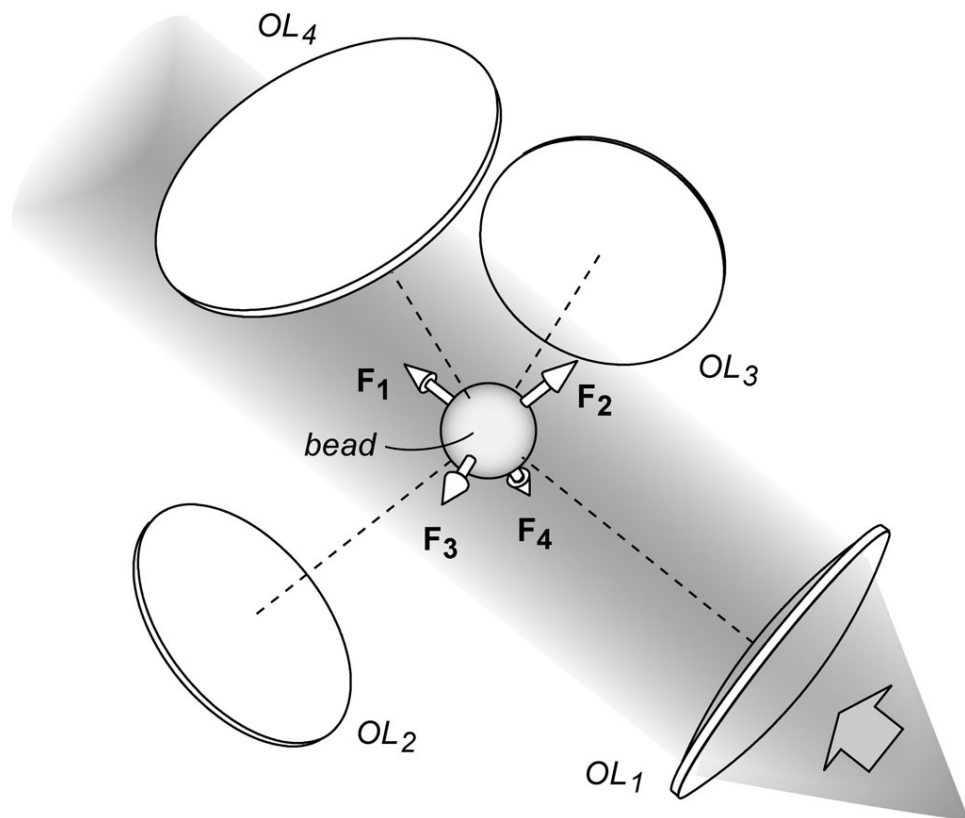


Fig. 2.5 Simplified geometry of the DAOM (not to scale). The four objective lenses (OL₁-OL₄) that collimate the laser beams, a bead and one beam are shown, and the directions of all four dominant (axial) forces are indicated. (*Huisken et al., 2004c*)

2.2 Theory

In this section the optical forces acting on a sphere in a collimated beam are calculated. The calculations are based on ray optics and are therefore only valid for the case of relatively large particles with respect to the wavelength of the trapping beam (radius $R \gg 1 \mu\text{m}$). The results obtained from a single beam are used to describe the forces in a tetrahedral trap like the DAOM.

2.2.1 Forces in collimated laser beams

The light pressure on a fully absorbing surface in a medium (refractive index n_m) is (Jackson, 1975)

$$p = \frac{n_m^2 E^2}{2\mu_0 c^2}, \quad (2.1)$$

and is exerted along the direction of light propagation. c is the speed of light in vacuum, μ_0 is the magnetic field constant, and E is the electric field strength, which at the waist of a Gaussian beam is

$$E^2 = \frac{4P\mu_0 c}{w^2 \pi n_m} e^{-\frac{2r^2}{w^2}}, \quad (2.2)$$

with laser power P and radius w of the beam at the waist. Hence, the pressure in a Gaussian beam is

$$p = \frac{2Pn_m}{w^2 \pi c} e^{-\frac{2r^2}{w^2}} = \frac{n_m}{c} I, \quad (2.3)$$

where I is the intensity of the beam at the point where the absorption occurs. The light pressure is linearly dependent on the light intensity.

If the light is not fully absorbed but rather reflected and transmitted, the process can be described by absorption followed by re-emission in the direction of reflection and transmission. In the following, we consider a ray bundle representing the beam propagating through the particle. At each interface the rays are reflected and transmitted, which results in an optical force acting at the interfaces.

As a *particle* we consider a sphere with radius R and index of refraction n_p that we assume to be homogeneous. It is immersed in a medium with a refractive index $n_m < n_p$. The vector pointing from the center of the particle to the surface in cartesian coordinates is

$$\mathbf{r}(\varphi, \vartheta) = R \hat{\mathbf{e}}(\varphi, \vartheta) \quad (2.4)$$

$$\hat{\mathbf{e}}(\varphi, \vartheta) = (\cos \varphi \sin \vartheta, \sin \varphi \sin \vartheta, \cos \vartheta) \quad (2.5)$$

where $\hat{\mathbf{e}}(\varphi, \vartheta)$ is the unit vector of the spherical coordinate system. This vector is perpendicular to the surface of the particle.

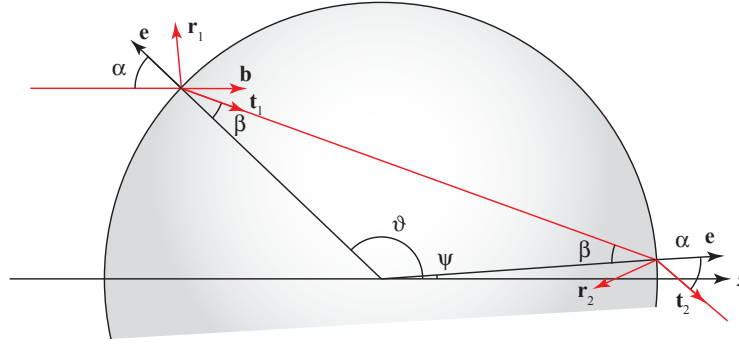


Fig. 2.6 A ray traverses a bead and is partially reflected and refracted.

The *beam* propagates along z (Fig. 2.6)

$$\hat{\mathbf{b}} = (0, 0, 1) \quad (2.6)$$

and is off axis by Δx . The beam has a Gaussian intensity profile and is incident on the particle with intensity

$$I(\varphi, \vartheta, \Delta x) = \frac{2P}{\pi w^2} e^{-2((x-\Delta x)^2 + y^2)/w^2}. \quad (2.7)$$

In the following we assume that the beam is well collimated over the full working range of the manipulator, i. e. all rays are assumed to be parallel and the intensity of the beam is described by (2.7).

At the *first point of intersection* the angle of incidence (i. e. the angle between $\hat{\mathbf{e}}$ and $-\hat{\mathbf{b}}$) is (Fig. 2.6)

$$\alpha(\varphi, \vartheta) = \arccos(-\hat{\mathbf{e}} \cdot \hat{\mathbf{b}}) = \pi - \vartheta. \quad (2.8)$$

The angle of refraction inside the sphere according to Snell's law is

$$\beta(\varphi, \vartheta) = \arcsin\left(\frac{n_m}{n_p} \sin(\alpha(\varphi, \vartheta))\right). \quad (2.9)$$

The rays are partially reflected and refracted, and the intensities are given by the reflection and transmission coefficients according to the Fresnel formulas*

$$R(\alpha, \beta) = \frac{\tan(\alpha - \beta)^2}{2 \tan(\alpha + \beta)^2} + \frac{\sin(\alpha - \beta)^2}{2 \sin(\alpha + \beta)^2}, \quad (2.10a)$$

$$T(\alpha, \beta) = 1 - R(\alpha, \beta). \quad (2.10b)$$

The direction of the transmitted ray $\hat{\mathbf{t}}_1$ can be obtained by rotating the vector $-\hat{\mathbf{e}}(\varphi, \vartheta)$ by the angle $-\beta$ about the axis

$$\hat{\mathbf{a}}_1(\varphi, \vartheta) = \hat{\mathbf{e}}(\varphi, \vartheta) \times \hat{\mathbf{b}}. \quad (2.11)$$

* For simplicity the formulas used here do not take polarization into account.

Rotation of a vector $\hat{\mathbf{u}}$ about an axis $\hat{\mathbf{v}}$ by an angle γ yields

$$\hat{\mathbf{u}} \cos \gamma + (1 - \cos \gamma)(\hat{\mathbf{v}} \cdot \hat{\mathbf{u}})\hat{\mathbf{v}} + \sin \gamma(\hat{\mathbf{v}} \times \hat{\mathbf{u}}). \quad (2.12)$$

The intensity of the transmitted ray is

$$I_{t,1}(\varphi, \vartheta, \Delta x) = I(\varphi, \vartheta, \Delta x) T(\alpha, \beta). \quad (2.13)$$

The direction of the reflected ray is obtained by rotation of the vector $\hat{\mathbf{e}}(\varphi, \vartheta)$ about the axis $\hat{\mathbf{a}}_1(\varphi, \vartheta)$ (2.11) by the angle α . The intensity is

$$I_{r,1}(\varphi, \vartheta, \Delta x) = I(\varphi, \vartheta, \Delta x) R(\alpha, \beta). \quad (2.14)$$

The resulting pressure \mathbf{p}_1 at (φ, ϑ) is

$$\mathbf{p}_1 = \frac{n_m}{c} \cos \alpha (\mathcal{I}\hat{\mathbf{b}} - I_{r,1}\hat{\mathbf{r}}_1 - I_{t,1}\hat{\mathbf{t}}_1). \quad (2.15)$$

The factor $\cos \alpha$ accounts for the fact that the rays hit the surface at an angle α .

The transmitted ray traverses the sphere and hits the surface again at the coordinates (ξ, ψ) (Fig. 2.6)

$$\xi(\varphi, \vartheta) = \varphi, \quad (2.16a)$$

$$\psi(\varphi, \vartheta) = \vartheta + 2\beta(\varphi, \vartheta) - \pi. \quad (2.16b)$$

The ray intersects the surface at an angle β . The direction of the reflected ray $\hat{\mathbf{t}}_2$ is obtained by rotating the vector $-\hat{\mathbf{e}}(\xi, \psi)$ around the axis $\hat{\mathbf{e}} \times \hat{\mathbf{t}}_1$ by the angle $-\beta$. Its intensity is

$$I_{r,2}(\varphi, \vartheta, \Delta x) = I_{r,1}(\varphi, \vartheta, \Delta x) R(\alpha, \beta). \quad (2.17)$$

The transmitted ray leaves the surface at an angle α . The direction is obtained by rotating the vector $\hat{\mathbf{e}}(\xi, \psi)$ around $\hat{\mathbf{e}} \times \hat{\mathbf{t}}_1$ by the angle α . Its intensity is

$$I_{t,2}(\varphi, \vartheta, \Delta x) = I_{t,1}(\varphi, \vartheta, \Delta x) T(\alpha, \beta). \quad (2.18)$$

The resulting pressure \mathbf{p}_2 at (ξ, ψ) is

$$\mathbf{p}_2 = \frac{n_m}{c} \cos \beta (I_{t,1}\hat{\mathbf{t}}_1 - I_{r,2}\hat{\mathbf{r}}_2 - I_{t,2}\hat{\mathbf{t}}_2). \quad (2.19)$$

The total force on the sphere is obtained by integration over the half of the sphere that faces the incident beam,

$$F = \int_{-\pi}^{\pi} d\varphi \int_{\pi/2}^{\pi} d\vartheta (\mathbf{p}_1(\varphi, \vartheta) + \mathbf{p}_2(\varphi, \vartheta)) \sin \theta R^2. \quad (2.20)$$

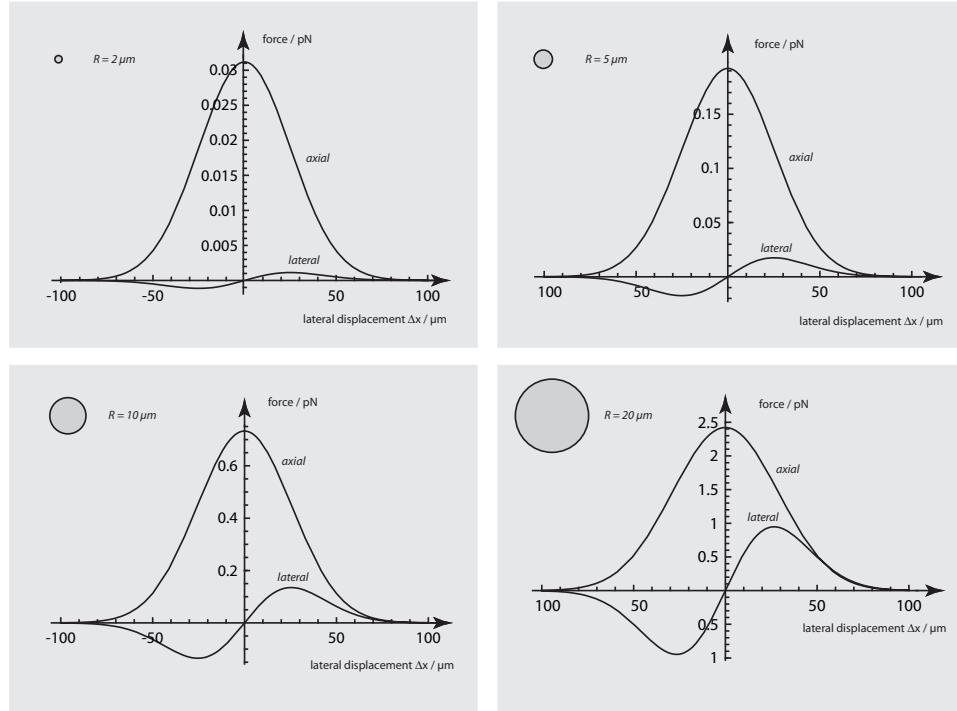


Fig. 2.7 Optical forces on a spherical particle in a collimated beam as a function of the lateral displacement of the sphere from the beam's axis. $R = 2, 5, 10, 20 \mu\text{m}$, $n_p = 1.6$, $n_m = 1.33$, $P = 10 \text{ mW}$, $w = 50 \mu\text{m}$.

We neglect further reflections within the particle as having negligible intensity (Wohland *et al.*, 1996).

Because of the cylindrical symmetry of the forces on a particle in a collimated beam it is useful to split them into two components: lateral and axial. The axial component pushes the particle along the propagation direction of the beam and the lateral component is directed towards the axis and can confine the particle to the axis (see section 2.1.2).

The optical forces were calculated according to the above model for four different particle sizes from $2 \mu\text{m}$ to $20 \mu\text{m}$ and the following parameters: $n_p = 1.6$, $n_m = 1.33$, $P = 10 \text{ mW}$, $w = 50 \mu\text{m}$. As can be seen in Fig. 2.7 the axial force follows the intensity profile of the beam: it is strongest in the center of the beam and drops off to the sides. The lateral force looks like the negative derivative of the axial force curve. Its magnitude is maximal when the lateral intensity gradient is maximal. In general, the optical forces on a sphere in a collimated beam increase with particle size. At the same time the lateral force becomes more pronounced as the particle size approaches the beam width.

The larger the sphere relative to the beam diameter, the larger the lateral gradient force relative to the axial scattering force. In Fig. 2.8 the optical forces along

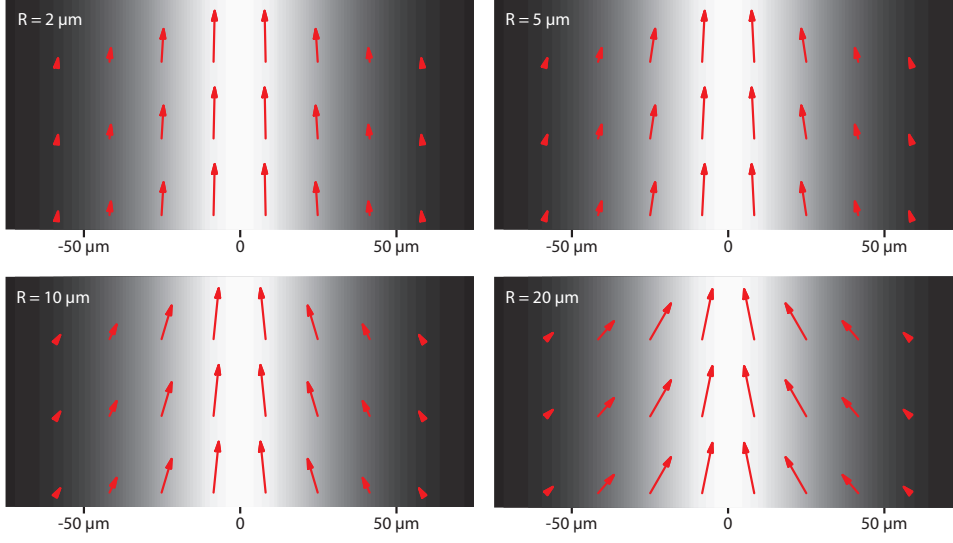


Fig. 2.8 Optical forces in a single collimated Gaussian beam. The larger the bead the more pronounced are lateral forces that confine the bead to the optical axis.

and across a beam are plotted for the same Gaussian beam ($w = 50 \mu\text{m}$). In the case of the $2 \mu\text{m}$ bead the lateral gradient does not provide a significant additional force, while the axial force is modulated by the intensity gradient. However, in the case of the $20 \mu\text{m}$ bead the lateral gradient leads to a strong lateral force pushing the particle towards the beam's axis. As we will see in the following section this influences the overall forces in a tetrahedral trap.

2.2.2 Forces in a four beam manipulator

In a multi-beam manipulator, in which N collimated beams are used to confine and move a sample, the total optical force on a particle is the sum of N axial and N lateral force components

$$\mathbf{F} = \sum_{i=1}^N \frac{P_i}{P_0} (\mathbf{F}_{\text{ax},i} + \mathbf{F}_{\text{lat},i}). \quad (2.21)$$

We assume that the relative power of each beam P_i/P_0 can be adjusted independently of the others, and neglect the effects of inter-beam interference.

The *axial* force components $\mathbf{F}_{\text{ax},i}$ are directed along the axes $\hat{\mathbf{a}}_i$ (see section 1.4.1) and depend on the distance d_i of the particle to the axes

$$\mathbf{F}_{\text{ax},i}(d_i) = F_{\text{ax},i}(d_i) \hat{\mathbf{a}}_i. \quad (2.22)$$

The displacement vector \mathbf{d}_i from a point at \mathbf{x} to an axis $\hat{\mathbf{a}}_i$ is

$$\mathbf{d}_i = (\mathbf{x} \cdot \hat{\mathbf{a}}_i) \hat{\mathbf{a}}_i - \mathbf{x}. \quad (2.23)$$

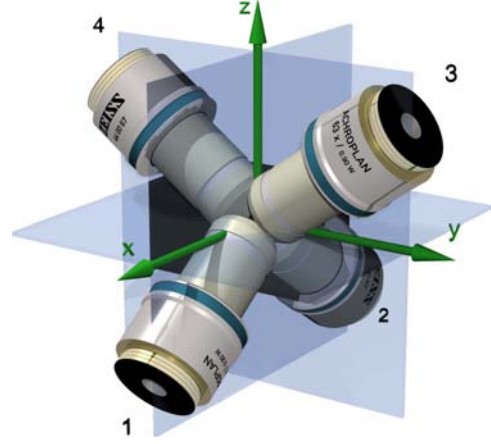


Fig. 2.9 In the Differential Active Optical Manipulator (DAOM) four trapping beams are oriented along the axes of a tetrahedron. Each beam is collimated by an Achromplan 63 \times , NA = 0.9 lens. In the center of the lens arrangement the beams overlap in a volume ca. 100 μm in diameter.

The *lateral* force components $\mathbf{F}_{\text{lat},i}$ are directed along this vector $\hat{\mathbf{d}}_i$

$$\mathbf{F}_{\text{lat},i}(d_i) = |F_{\text{lat},i}(d_i)|\hat{\mathbf{d}}_i. \quad (2.24)$$

The Differential Active Optical Manipulator (DAOM) presented in this work uses four collimated beams. The collimated beams are provided by four objective lenses that are arranged along the axes of a tetrahedron as shown in Fig. 2.9.

From section 1.4.1, the four axes are arranged along the directions

$$\hat{\mathbf{a}}_1 = (-\sqrt{\frac{2}{3}}, 0, \sqrt{\frac{1}{3}}), \quad \hat{\mathbf{a}}_2 = (\sqrt{\frac{2}{3}}, 0, \sqrt{\frac{1}{3}}), \quad (2.25a)$$

$$\hat{\mathbf{a}}_3 = (0, -\sqrt{\frac{2}{3}}, -\sqrt{\frac{1}{3}}), \quad \hat{\mathbf{a}}_4 = (0, \sqrt{\frac{2}{3}}, -\sqrt{\frac{1}{3}}). \quad (2.25b)$$

For this configuration, the total optical force on a 2 μm sphere is calculated and plotted in Fig. 2.10 for the case of equal beam powers. The forces in the x - y -plane (Fig. 2.10A) are directed towards the center of the manipulator. The forces are strongest at a distance of ca. 25 μm from the center. The forces of all four beams cancel in the center of the manipulator, where no optical force acts on the particle. Looking at the x - y -plane, it seems as if the four beams provide a stable trap and the particle can be trapped passively in the center. However, looking at a plane in which one of the four optical axis lie we see that the particle can escape along the direction of this axis (in Fig. 2.10B this is shown for objective lens number 4).

As has been shown in Fig. 2.7, the axial scattering forces dominate over the lateral gradient forces in the case of a small bead (e.g. $R = 2 \mu\text{m}$) relative to the beam width ($w = 50 \mu\text{m}$). This means that without any lateral gradient forces the tetrahedral configuration cannot provide a stable trapping position. However, a stable trap can be achieved by actively compensating for any drift of the particle. In addition, the particle can be trapped and manoeuvred across the

overlap of the four beams by actively changing the power of the four beams. In our example (Fig. 2.10B), once the bead has left the center position along the axis of beam 4, it can be moved back into the center by increasing the powers of beams 1–3.

Figure 2.11 shows the same plot for a much larger bead ($R = 20 \mu\text{m}$). The lateral gradient forces of beams 1–3 are strong enough to overcome the axial forces and confine the bead to the center of the trap. This, however does not limit the functionality of the DAOM. There are only weak *lateral* gradient forces involved, and these can be overcome with axial forces. This is in contrast to optical tweezers where strong *axial* gradient forces are always present and do not allow the transport of the particle along the beam.

In the DAOM the goal is to provide a means to transport the particle across long distances. As has been explained in the introduction, this can be done by the use of collimated laser beams. It has been shown that for a single beam without an axial gradient no stable trapping is possible, which at the same time leaves the possibility to move a particle over long distances. Using four collimated beams assures that the particle can be moved in any direction by simply changing the intensities of the beams. This is demonstrated in section 2.4.

In addition to the optical forces, the sample in the DAOM can experience buoyancy, friction, and thermal forces. If the sample is at rest, the sum of all forces must vanish:

$$\mathbf{0} = \sum_{i=1}^4 \mathbf{F}_{\text{opt},i}(\mathbf{x}, t) + \mathbf{F}_b + \mathbf{F}_f(v(t)) + \mathbf{F}_t(t). \quad (2.26)$$

The buoyancy \mathbf{F}_b is a gravitational effect and depends solely on the relative density of the sample and its volume. The friction $\mathbf{F}_f(v(t))$ is a function of the sample's velocity relative to the immersion medium $v(t)$. $\mathbf{F}_t(t)$ describes the thermal forces that cause the sample to exhibit Brownian motion. These forces are not under the direct control of the experimenter, and can cause the particle to be disturbed from its desired position. However, the optical forces $\mathbf{F}_{\text{opt},i}(\mathbf{x}, t)$, can be controlled temporally via interactive feedback to keep (2.26) fulfilled (see section 2.4).

In order to change the position of the sample, the optical forces are varied so as to provide a net force that pushes the sample in the desired direction. Once the target position is reached, the forces are again balanced and the DAOM ensures a zero net force. Only in the case of a desired displacement or an external perturbation is this balance briefly disrupted. It should be noted that (2.26) can be satisfied by an infinite set of optical forces. Theoretically, any combination of optical forces whose sum balances buoyancy and friction can be chosen. This gives us the freedom to reduce the total power sufficiently to exclude optical and thermal damage to the sample.

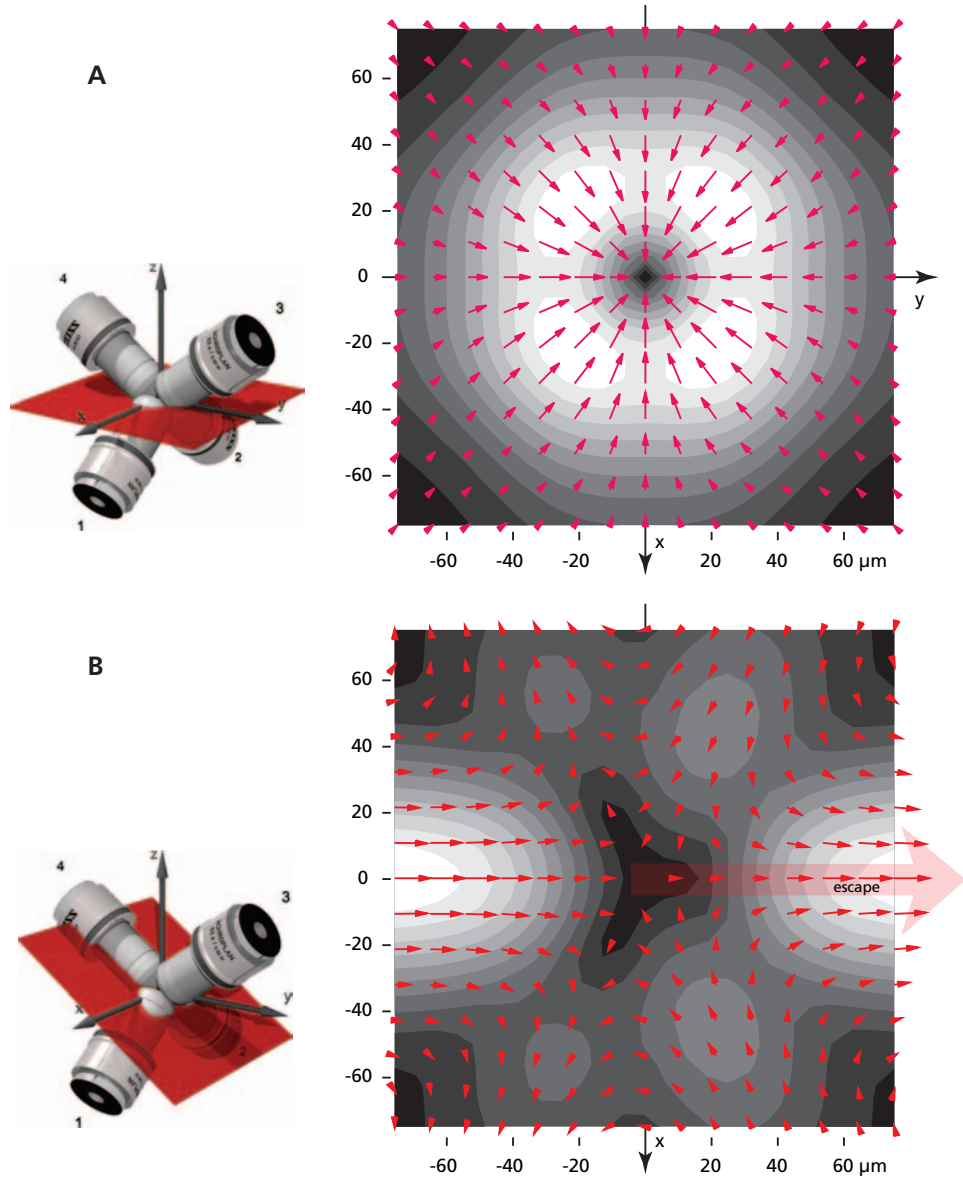


Fig. 2.10 Optical forces on a $R = 2\ \mu\text{m}$ bead in the DAOM with all four beams set to equal intensity. In (A) the projection of the forces in the x - y -plane are shown. In (B) the projection of the forces in the plane in which the x -axis and the optical axis 4 lie is shown. The particle will be pushed out of the manipulator along one of the optical axis. The beams have a radius of $w = 50\ \mu\text{m}$.

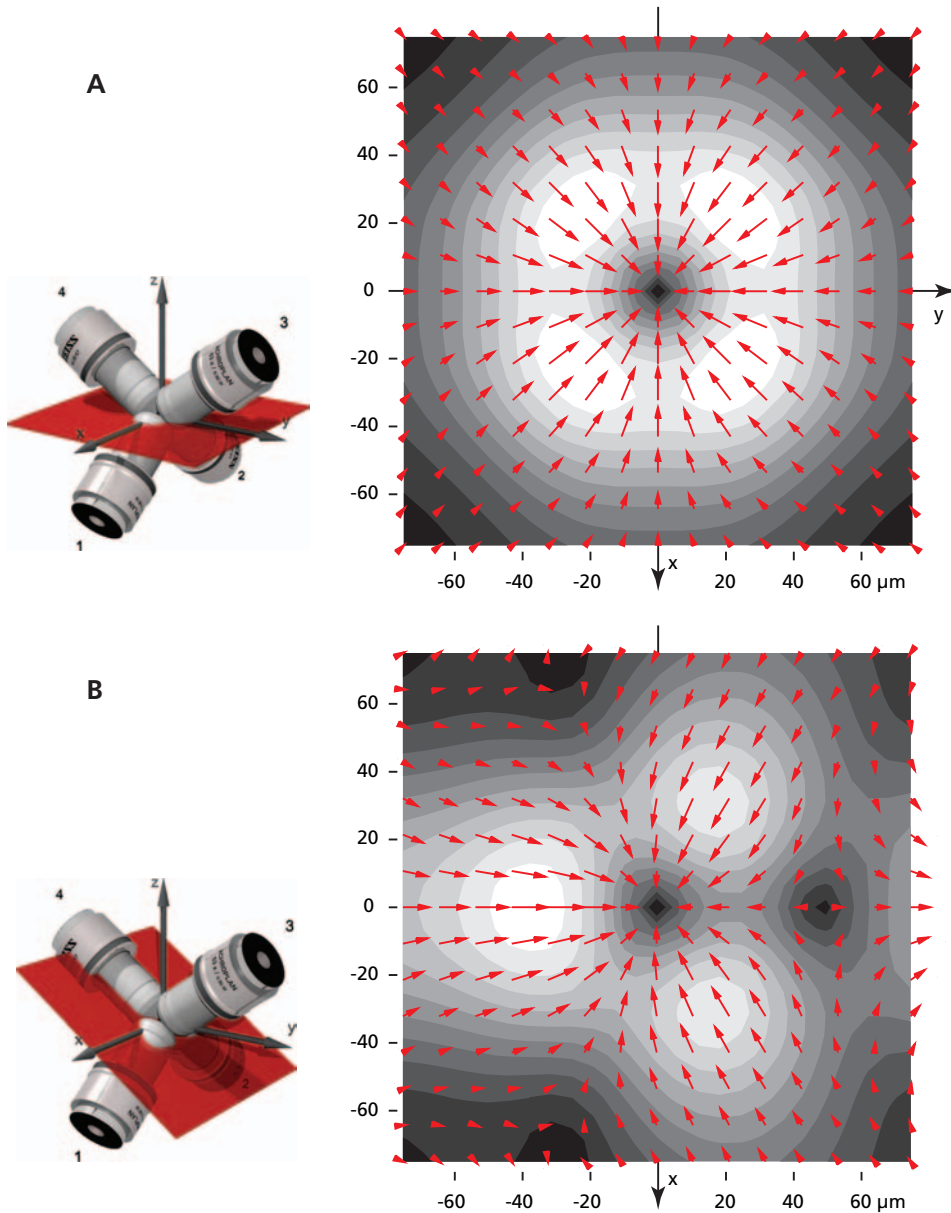


Fig. 2.11 Optical forces on a $R = 20 \mu\text{m}$ bead in the DAOM with all four beams set to equal intensity. In (A) the forces in the x - y -plane are shown. In (B) the plane in which the x -axis and the optical axis 4 lie is shown. Such a large bead is stably trapped in the center of the manipulator. The beams have a radius of $w = 50 \mu\text{m}$.

2.3 Setup

The Multi-Imaging Axis Microscope (MIAM) introduced in chapter 1 provides an ideal frame work for a tetrahedral optical manipulator. The objective lenses that are used for the imaging can at the same time be used to shape the manipulation beams.

The setup of the DAOM (without most of the parts required for the MIAM) is depicted in Fig. 2.12. It consists of two units. One unit (Fig. 2.12a) provides the four beams for sample manipulation. The output of a laser (Nd-YAG, $\lambda = 1064 \text{ nm}$) is split into four beams by an arrangement of mirrors and beam splitter cubes. Each beam passes through an acousto-optic modulator (AOM), which provides fast, precise, and independent attenuation. Each beam is then coupled into a single-mode polarization-preserving optical fiber, which guides it to the second unit consisting of the optics required for the manipulator and the sample observation (Fig. 2.12b). See the appendix for detailed drawings and photographs of the setup.

The tetrahedral configuration of the four beams is realized by a set of four identical microscope objectives (Zeiss, Achroplan 63 \times , N.A. 0.9, water dipping) arranged along the tetrahedron's axes of symmetry (as in the MIAM). The arrangement is shown in (Fig. 2.12b) in a simplified drawing, omitting the mechanical components that hold the objectives. The distance between the objectives is chosen such that their focal planes intersect at a single point in the centre of the tetrahedron. With a working distance of 1.46 mm the objective lenses provide sufficient space to inject the sample into the drop of water that fills the volume between the four lenses and is held in place by surface tension. The optics consist of four identical arms, only one of which is shown in Fig. 2.12b. The light exiting the fiber is focused by a lens into the back focal plane of the objective lens. The resulting collimated beam passes through the volume between the four objective lenses and exits the sample region through the space between the opposing three objectives. The four beams intersect in the centre, defining the manipulation volume, which is currently about $1 \text{ nL} = (100 \mu\text{m})^3$.

In addition to manipulation, the objective lenses also allow high-resolution observation of the sample. A dichroic mirror (transparent to the NIR manipulation beam) reflects visible light from the sample to a tube lens, which forms an image of the object on the CCD chip of a camera (Sony XCD-SX900, 1280×960 pixels). This allows one to follow the movement of the sample in three dimensions by analyzing the four simultaneously recorded camera views. Moreover, the data acquired with the four cameras is complementary, since it yields multiple views of the sample (see chapter 1). In the following experiment each view represents a field of approximately $144 \mu\text{m}$ by $108 \mu\text{m}$. The sample is illuminated with an external lamp (not shown) and is imaged by its scattered light. However, it should be noted the system is not restricted to scattered light: other microscopy tech-

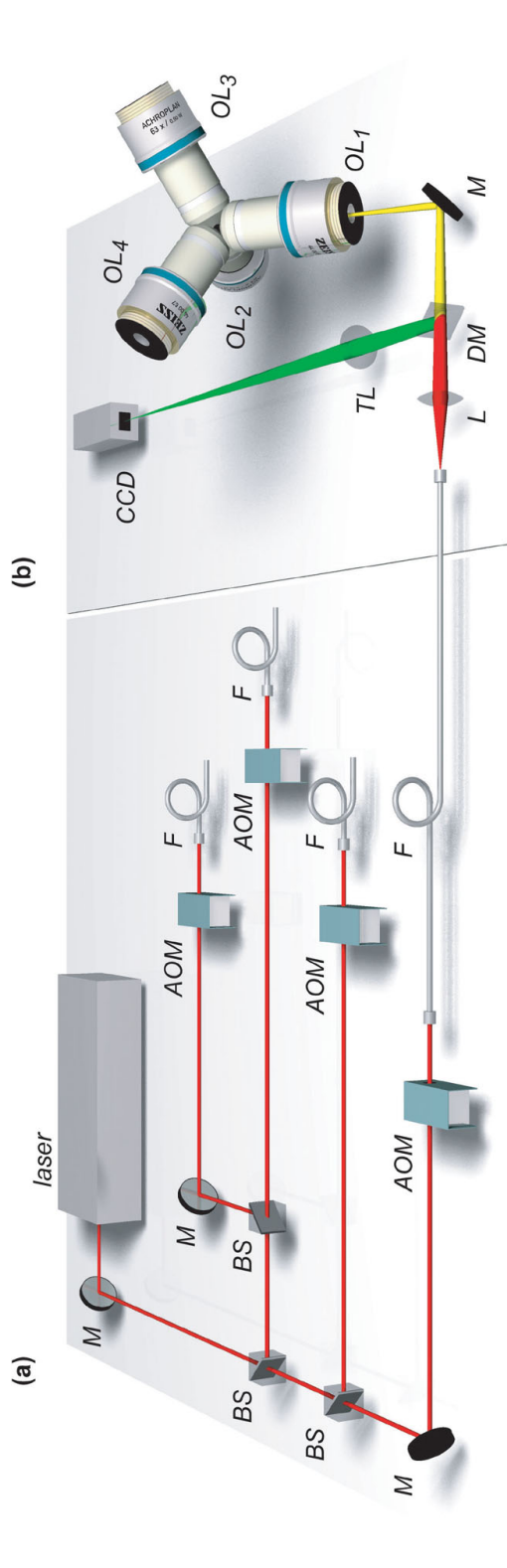


Fig. 2.12 The two units of the DAOM. (a) Unit that splits the manipulation beam utilizing mirrors (M) and beam splitter cubes (BS). Each of the four beams is attenuated individually by an acousto-optic modulator (AOM) and is coupled into a single mode fiber (F). (b) Arrangement of the four objectives (OL₁ - OL₄). One arm of the microscope is shown in detail: lens (L), dichroic mirror (DM), tube lens (TL), and camera (CCD). Optical elements and distances are not drawn to scale; the illumination optics for imaging via the camera are not shown. (Huisken *et al.*, 2004c)

niques (e.g. fluorescence, see section 1.5) can also be applied to visualize the sample.

The space between the lenses is about 3 mm in diameter, and is filled with a drop of aqueous medium held in place by surface tension. The sample is injected into this droplet and can then be manipulated optically. The user interface on a computer shows all four camera views and provides full control over the intensity of the four trapping beams, so that the sample can be translated along any axis to allow acquisition of a three-dimensional image stack.

Four position sensitive devices (PSD) are integrated to track the sample during the experiment. For this purpose, infrared LEDs ($\lambda = 880\text{ nm}$) is used to illuminate the sample and the back-scattered light is imaged onto the PSDs. Each PSD provides a 2D position signal, and the signals of all four PSDs are used to calculate the exact 3D position of the sample. This position detection system has not been completed during this work.

The DAOM integrates very well into the concept of the MIAM. For the MIAM each arm of the microscope consists of a fiber for fluorescence excitation, an LED for scattering contrast, and a camera for detection. For the DAOM a fiber for the trapping beam, an infrared LED, and a PSD are implemented. Such a unit is reproduced four times, and they are assembled as shown in Fig. 2.13. For a list of components, drawings, and photographs see the appendix.

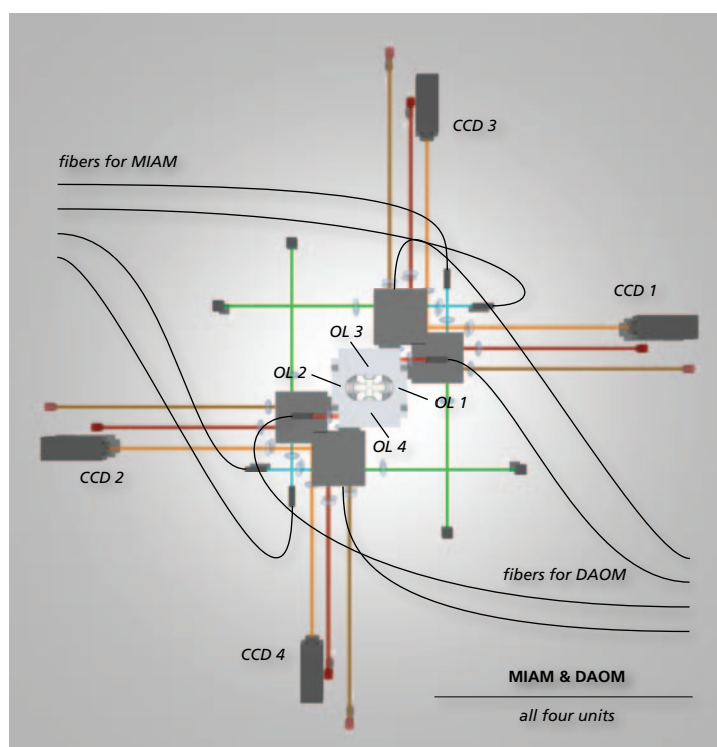
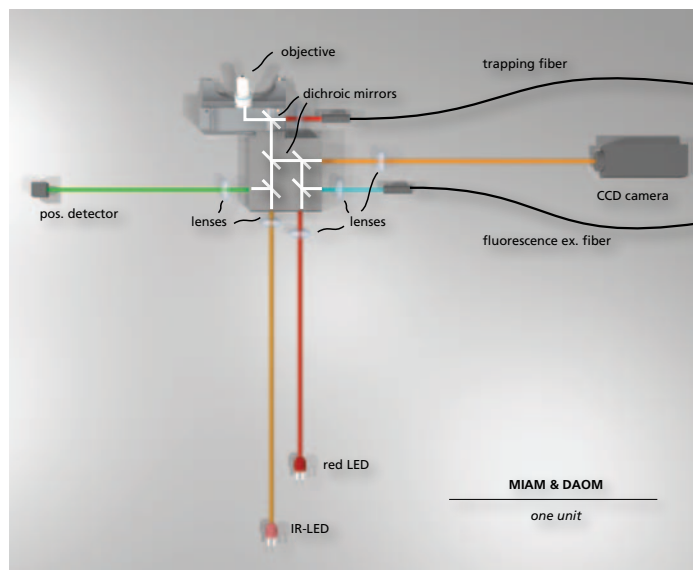


Fig. 2.13 Setup of a single arm integrating the MIAM and the DAOM in one instrument (top). The four parts are assembled to give a tetrahedral arrangement with both the MIAM and DAOM functionality.

2.4 Experimental results

In the DAOM latex beads with a diameter of $20\text{ }\mu\text{m}$ have been trapped and manipulated within the field of view of the cameras. Three examples are shown here to demonstrate the functionality of the DAOM.

Figure 2.14 shows selected frames from a video sequence taken with two cameras (CCD_1 and CCD_2), demonstrating the ability to move a bead through the focal planes while observing it. First, the bead was translated to the initial position shown in frame 1 by adjusting all four beam intensities. The power incident on the bead during the experiment was in the range 0–20 mW per beam. In the sequence depicted, only the intensities of beams 1 and 2 were modulated. However, beams 3 and 4 were held at constant power and were crucial to perform this experiment. Starting with the situation in frame 1 and increasing the intensity of beam 2 resulted in a movement along the direction sketched in the panel below frame 1. The result after seven seconds was a defocus on camera 2 (frame 2). This was accompanied by a shift towards the top of the frame on camera 1 and a slight defocusing.

Next, the movement was reversed by attenuating beam 2. The result is shown in frame 3, where the situation is the same as in frame 1. The slight lateral offset is due to the fact that the powers of beams 3 and 4 were not corrected during this sequence. The same procedure was repeated with beam 1. Its intensity was increased and decreased resulting in a focusing and defocusing on camera 1, as shown in panels 3–5. The whole procedure from frame 1 to frame 5 took 45 s. During that time the bead moved only slightly laterally, so beams 3 and 4 were left at a constant power. The sequence shown here represents a focusing procedure that is common in microscopy when acquiring three-dimensional image stacks. The sample was moved by $15\text{ }\mu\text{m}$ with a speed of up to $2\text{ }\mu\text{m/s}$ along both imaging axes. However, any three-dimensional path can be achieved by controlling all beams simultaneously.

3D manipulation is demonstrated by capturing and manipulating $20\text{ }\mu\text{m}$ diameter latex beads within the field of view of the cameras. For these experiments the field of view has been increased by addition of a $2.8\times$ telescope in each of the camera ports. Figure 2.15 shows two selected frames from a video sequence taken with cameras CCD_1 to CCD_4 , demonstrating the ability to move the sample into the centre of all fields of view. The bead, which was initially centered in the field of view of camera 1 (Fig. 2.15a) but happened to be too close to that lens, was moved towards the centre of the microscope by increasing the intensity of beam 1. Once the particle reached its destination, the beam powers were again balanced, bringing the bead to rest (Fig. 2.15b). The total distance the bead was moved from the edge of the field to its centre is $69\text{ }\mu\text{m}$ (Fig. 2.15c). It should be noted that this was limited by the field of view of the cameras ($144\text{ }\mu\text{m}$ by $108\text{ }\mu\text{m}$). Trajectories in any direction covering distances on the order of the

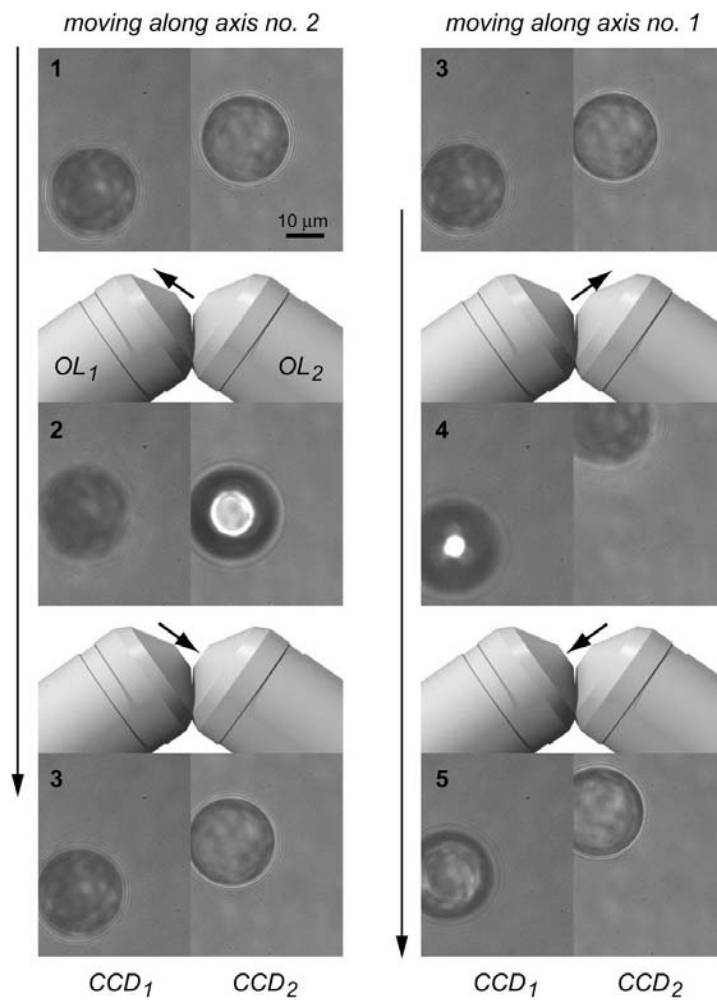


Fig. 2.14 Focusing of a 20 μm latex bead in the DAOM as seen with cameras CCD₁ and CCD₂. The sequence of images has been extracted from a movie. Between frames the orientation of the two lenses OL₁ and OL₂ is shown, and the direction in which the bead is pushed is sketched. Objectives OL₃ and OL₄ are omitted from the sketch for clarity. The left panel shows the movement along the axis of OL₂ and the right along the axis of OL₁. The bead is repositioned away from, and then back towards, the objective. (Huisken *et al.*, 2004a)

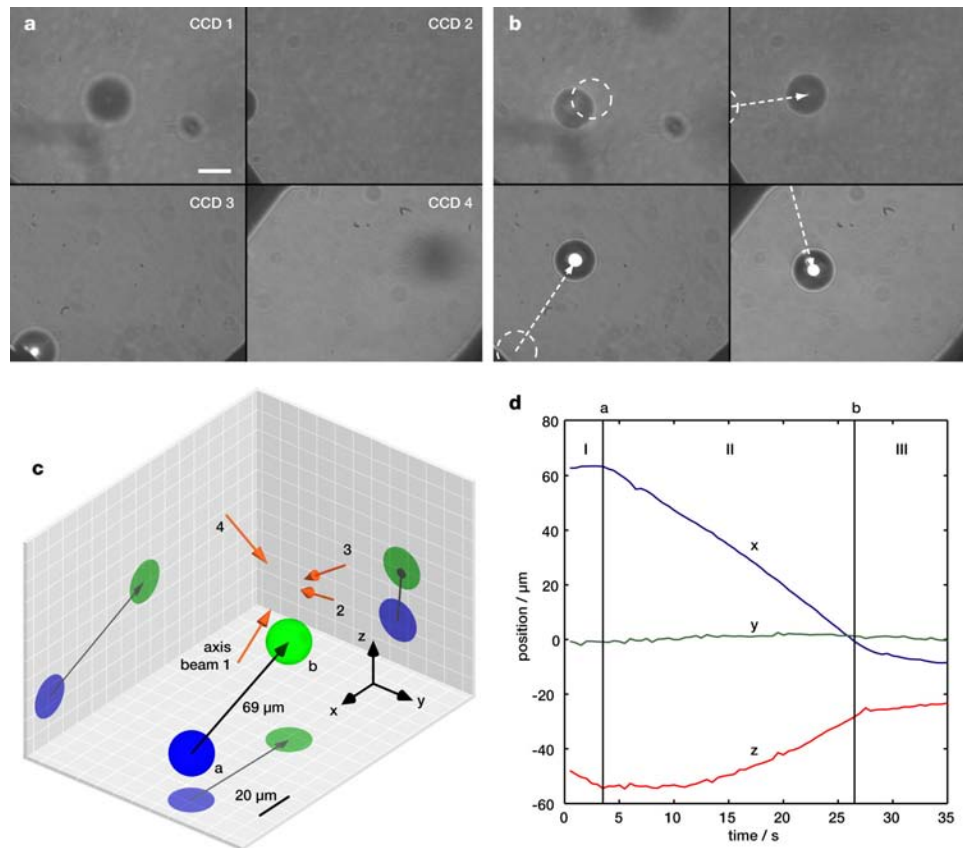


Fig. 2.15 Moving a $20\text{ }\mu\text{m}$ diameter latex bead in the DAOM as seen with cameras CCD_1 – CCD_4 . Two frames from a video sequence are shown. (a) Initial situation: the bead is only clearly visible in the field of view of CCD_1 , scale bar: $20\text{ }\mu\text{m}$. (b) Pushing with beam 1 moves the bead in the field of view of all four cameras; it is also now in focus on CCD_1 . Arrows indicate the direction the bead was moved. (c) three dimensional graphical representation of the bead's movement. Blue and green: bead in the position from frames a and b, respectively; orange: axes of the four beams. (d) coordinates of the bead over time. (Huisken *et al.*, 2004c)

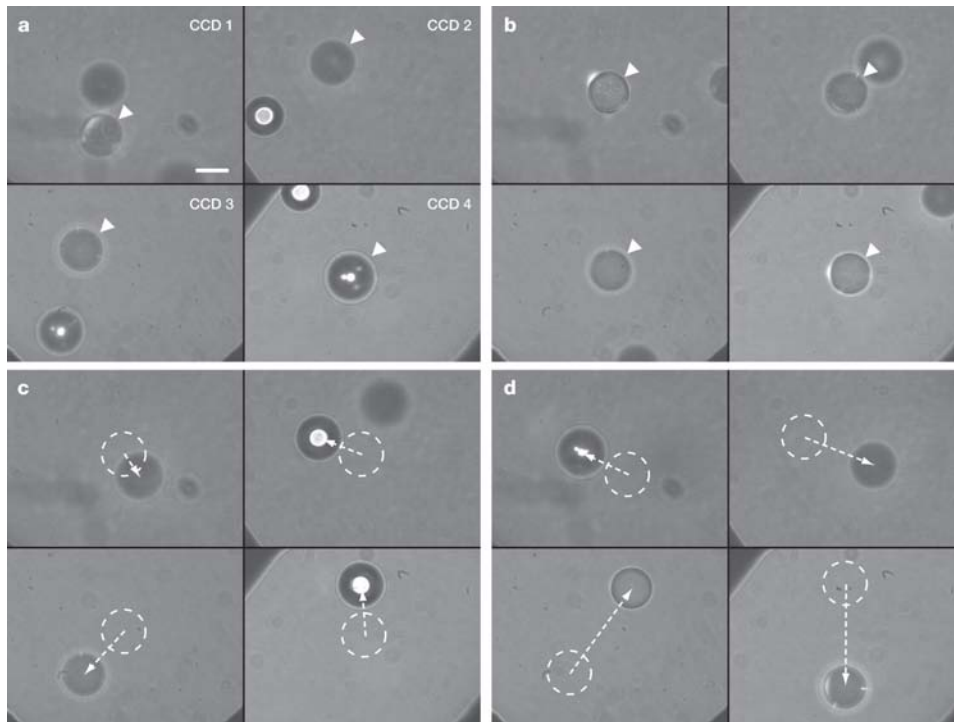


Fig. 2.16 Centering a bead and translation across the field of view. (a) Selection of the bead of interest (arrowhead). (b) The bead is centered in all four fields of view. (c)–(d) By adjusting the powers of all four beams the bead is moved across the fields of view. Circles indicate the previous positions, scale bar: $20\ \mu\text{m}$. (Huisken *et al.*, 2004c)

manipulation beam's width ($100\ \mu\text{m}$) are feasible within the volume of beam intersection. The sample can be transported into the manipulation volume along the beams' axes over even longer distances. Fig. 2.15d shows the coordinates of the bead's centre relative to the centre of the microscope, which have been extracted from the sequence by video analysis. The bead moved in $-x$ and $+z$ -direction while maintaining the position in the y -direction, consistent with a force applied in the direction of beam 1. The absolute speed was about $3\ \mu\text{m/s}$. The sum of all four beam powers was kept constant ($< 50\ \text{mW}$, i. e. $< 6\ \mu\text{W}/\mu\text{m}^2$) during the experiment: from frame a until frame b (phase II) beam 1 was more intense than the other three by a factor of 3.4, and in phases I and III the powers of all four beams were the same.

Figure 2.16 shows a situation where two beads are visible in the fields of view. One bead was selected (arrowhead) and by actively adjusting the intensities of the four manipulation beams it was moved into the centre of the microscope (Fig. 2.16b). Subsequently, this bead was moved back and forth across the fields of view (Fig. 2.16c-d). The second bead was ignored and quickly drifted out of the fields of view. This shows that the common functions of translation and focusing of a sample can be easily performed and any three-dimensional path can

be achieved by controlling all beams simultaneously.

2.4.1 Conclusion

Trapping and active movement of the sample in a microscope can be gently performed by applying optical forces. In the DAOM four infrared laser beams are arranged along the axes of a tetrahedron and are approximately collimated within the vicinity of their region of intersection. The DAOM makes use of a distinctive advantage of collimated light: in contrast to optical tweezers, this instrument allows movement of the confined particle over long distances without mechanical scanning. The beams' forces superimpose in their common volume, and the total force (magnitude and direction) on the particle can be set by adjusting the beams' intensities. This can be done quickly and independently for each beam, allowing us to move a particle along arbitrary paths within a volume of about 1 nL. Active feedback can be implemented which ensures that the sample is held in place or transported to a specified position as desired. This allows focusing and lateral translation of the microscopic sample, which are common tasks in microscopy. During manipulation the particle is simultaneously observed from four sides.

In our current implementation, samples with a diameter ranging from 1 μm to more than 50 μm can be optically confined and moved across distances of almost 200 μm . The total distance that particles can be moved is limited by the field of view (i. e. the magnification of the system) and the size of the manipulation beams. The principle of the DAOM can be easily adjusted to other scales; beam diameters and magnification can be chosen as required. In our current implementation these parameters were chosen to fit samples that are of interest in the life sciences, ranging from single cells to small embryos. The use of collimated laser beams instead of highly-focused beams provides ultra-long working distances, which are especially advantageous for the manipulation and observation of large samples like embryos in developmental biology.

By controlling the beam powers via the AOMs, we have developed a means of transporting samples in a system requiring no moving parts. This eliminates the vibrations, creep, and hysteresis that generally accompany positioning with a mechanical stage. The speeds achievable, several micrometers per second, are primarily limited by the viscous drag that the samples experience in the medium, and by the applied optical power.

In this work we have introduced the principle of the DAOM and experimentally demonstrated its validity. However, for this proof-of-principle we have employed a simple, relatively slow feedback system with a response time of ca. 1 s. This limits the speed at which motion corrections can be performed, and accounts for the accuracy of a few microns seen in Fig. 3d. However, we are cur-

rently implementing a much faster feedback system (response time <1 ms), in which case we anticipate that the positioning accuracy will be limited by the resolution of the imaging optics, rather than the response of the feedback system.

The principle of the DAOM can be easily applied to a range of different sized samples. The diameter of the manipulation beams and the magnification of the objective lenses have to be chosen appropriately for the sample of interest and the desired working distance. We believe that the DAOM is an ideal manipulator for various samples, especially fragile samples in the life sciences that require gentle handling. The fact that the samples can be observed from four sides simultaneously makes the system especially interesting for multi-view microscopy like the MIAM.

The DAOM has great potential in many disciplines that require manipulation of relatively large samples, e. g. embryology and colloidal physics. Compared to optical tweezers, long-range 3D sample manipulation is achieved, which gives a distinct advantage for many applications. The fact that the manipulator is set up inside a microscope that consists of four objective lenses (MIAM) makes it ideally suited for three-dimensional light microscopy, especially multi-lens arrangements that provides excellent resolution with low NA (and therefore long working distance) lenses in large samples. The ability to acquire views from four different directions while manipulating the sample without mechanical contact offers new perspectives in the fields of trapping and imaging.

3. Selective Plane Illumination Microscopy

The MIAM presented in the first chapter is an example for a multi-view microscope in which the sample is observed simultaneously from four sides. It is a camera based widefield microscope that can image samples of up to ca. $150\text{ }\mu\text{m}$. By multi-view combination of four data sets an isotropic resolution was obtained with a gain in the volume resolution of $3.5\times$.

As discussed in section 1.2.1, multi-view combination can increase the resolution in a fully transparent sample in which all features are present in all data sets as shown for the MIAM in section 1.5. However, the method of multi-view combination is also useful when some data sets contain information about parts of the sample that does not appear in other data sets. In this case, the multi-view combination increases the overall information content in the fused data set. In the fused image all the information of the individual data sets is gathered, and a resolution improvement can be obtained in areas where the data sets overlap.

In the *Selective Plane Illumination Microscope (SPIM)* presented in this chapter the data for multi-view combination is obtained using a stage that allows rotation of the sample with respect to illumination and detection axes. This allows consecutive acquisition of images from different sides of the sample. In contrast to the MIAM, in which four views are simultaneously acquired, in the SPIM the number of views can be adapted to the complexity of the sample. A large number of different views can be obtained and combined by image processing using one of the methods described in section 1.3. However, the views are acquired one after the other, which limits the speed at which multi-view data can be acquired.

The SPIM is well suited for a large range of samples, from a few tens of microns up to a few millimeters in size. As will be shown in the course of this chapter, the SPIM is especially useful in the imaging of large samples ($100\text{ }\mu\text{m}$ – 1 mm). By multi-view combination it was possible to obtain a full 3D image of an intact Medaka fish embryo. This has been impossible with existing microscopes. Partially transparent samples about 1 mm in size make great demands on the microscope. The penetration depth at which a useful signal can be recorded is generally limited and depends on the scattering properties of the tissue. A single SPIM data set features a good penetration depth which can then be further

improved by multi-view combination.

Techniques that provide *optical sectioning* like e. g. the confocal microscope are clearly advantageous when imaging thick samples. Optical sectioning is present when the information content of a single image is restricted to the in-focus parts of the sample. Any out-of-focus components of the image are suppressed, or better, not generated in the first place. The SPIM provides optical sectioning in a straightforward and elegant way. Only the plane in focus is illuminated so that no out-of-focus fluorescence is excited and therefore cannot spoil the image. This technique allowed us to follow the complete embryogenesis deep inside the fruit fly *Drosophila melanogaster in vivo*.

This chapter gives a short introduction to optical sectioning techniques and in particular how sectioning can be obtained by selective illumination. The experimental setup of the SPIM is described in detail. Images of Medaka and *Drosophila* demonstrate the performance of the microscope. The chapter ends with a discussion including a comparison of confocal and SPIM.

3.1 Challenges of imaging large samples

Imaging of microscopic details deep inside large biological samples is a desirable competence for medicine, pathology and in particular for developmental biology. Especially challenging is the attempt to follow embryogenesis both in space and in time (4D imaging). The visualization of organogenesis or embryonic gene expression for the analysis of developmental processes at the molecular level are applications that are becoming increasingly important. Important goals of multidimensional imaging are to acquire the complete spatio-temporal pattern of genes or to track the tissue of interest during the development of an intact embryo (*in toto* imaging, *Megason and Fraser* (2003)). In order to visualize the precise 4D distribution of developmental events such as specific gene activation, the wide range from small scale (sub-cellular) to large scale (millimeters) processes need to be followed. Ideally such events, which can last from seconds to days, will be observed in live and fully intact embryos.

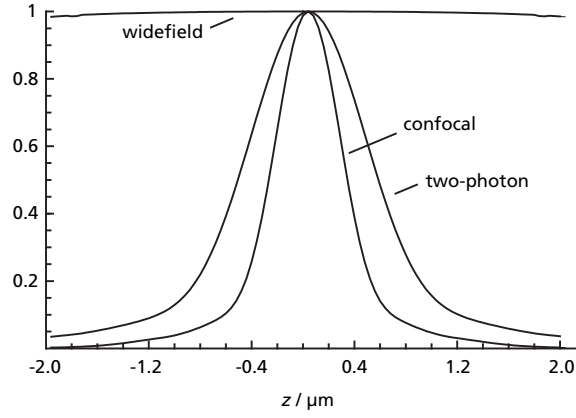
Several techniques have been developed that allow mapping of the 3D structure of large samples (*Ruffins et al.*, 2002). Gene expression has been monitored by *in situ* hybridization and block-face imaging (*Weninger and Mohun*, 2002). This procedure of fixing embryos at various stages of development, physically sectioning them, staining the sections, imaging, aligning, and combining the sections is cumbersome, and it destroys the embryo irretrievably. Techniques that provide non-invasive sectioning, as opposed to those which destroy the sample, are clearly advantageous, and are indispensable for live studies. Optical projection tomography (*Sharpe et al.*, 2002) has been shown to be a very promising tool capable of imaging fixed embryos at high resolution. Although magnetic resonance imaging (*Louie et al.*, 2000) and optical coherence tomography (*Huang et al.*, 1991) feature non-invasive imaging, they do not provide specific contrasts easily.

3.1.1 Optical sectioning

In optical microscopy, green fluorescent protein (GFP) and its spectral variants have become the least invasive labels, and are therefore indispensable tools for high-resolution visualization of specific protein localization patterns in living organisms (*Chalfie et al.*, 1994). When viewing GFP labelled samples, optical sectioning (which eliminates out-of-focus light) is obtainable by laser scanning microscopy (LSM), either by detection through a pinhole (Confocal LSM, *Pawley* (1995)) or by exploiting the non-linear properties of a fluorophore (multiphoton microscopy, *Denk et al.* (1990)).

The conventional fluorescence microscope has no optical-sectioning capability. At each depth in the specimen the total illumination power is the same,

Fig. 3.1 The integrated intensity of the PSF is constant as a function of z in the case of the widefield microscope. The integrated intensities of the confocal and two-photon PSFs peak at the focus. This illustrates the optical sectioning capabilities of these microscopes. (Jonkman and Stelzer, 2002)



i. e. the integral over the lateral extend of the PSF (see section 1.1.2) as a function of depth is constant (conservation of energy)

$$E_{\text{widefield,int}}(z) \propto \int_0^{\infty} |h_{\text{widefield}}(r, z)|^2 2\pi r^2 dr = \text{const.} \quad (3.1)$$

In contrast, in a confocal microscope and a two-photon microscope the corresponding relations are

$$E_{\text{conf,int}}(z) \propto \int_0^{\infty} |h_{\text{conf}}(r, z)|^2 2\pi r^2 dr = \int_0^{\infty} |h_{\text{ill}}(r, z)|^2 |h_{\text{det}}(r, z)|^2 2\pi r^2 dr \quad (3.2)$$

$$E_{2hv,int}(z) \propto \int_0^{\infty} |h_{2hv}(r, z)|^2 2\pi r^2 dr = \int_0^{\infty} (|h_{\text{ill}}(r, z)|^2)^2 2\pi r^2 dr. \quad (3.3)$$

These functions have a maximum in the focal plane (see Fig. 3.1), i. e. only a limited volume close to the focal plane contributes to the final image (depth-discrimination, optical sectioning). In the confocal microscope, when the sample is in the focal plane, the fluorescent light is focused onto the pinhole (see Fig. 1.3), and a large signal is detected. On the other hand, when the object is positioned out of the focal plane, a defocused spot is formed at the pinhole, and the measured intensity is greatly reduced.

Despite the improved resolution obtained in the axial direction and the sectioning capabilities, LSM suffers from two major limitations: a limited penetration depth in heterogeneous samples and a dramatic difference between the lateral and axial extents of the PSF (section 1.1.4). The limited working distance of high NA objective lenses, which are required for high-resolution imaging, and the severe drop in signal intensity with increasing depth in heterogeneous specimens are responsible for the limited working depth of a CLSM. Fig. 3.2 shows images

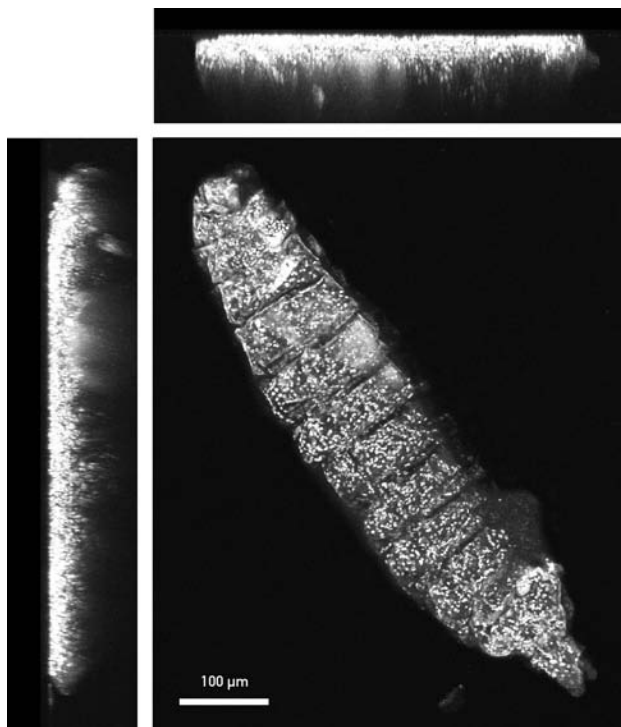


Fig. 3.2 *Drosophila* larva imaged with a confocal microscope (Leica TCS SP2) using a 20 \times , NA = 0.7 oil objective. Maximum projections along x (left), y (top), and z (center) show the limited penetration depth. GFP labels all cell nuclei.

of a *Drosophila melanogaster* larva taken on a confocal microscope and demonstrating the limited penetration depth of the system. Hecksher-Sørensen and Sharpe (2001) had to generate as many as 24 sections 70 μm thick to obtain a full expression pattern in mouse using a CLSM. A multi-photon microscope can image at greater depths, but at the expense of a lower resolution. A spinning-disk microscope (Pawley, 1995) can provide images at a much higher speed than the beam-scanning LSM, but inherits its other drawbacks.

Another approach to obtain optical sectioning was demonstrated by Neil *et al.* (1997). A stripe pattern of illumination is used to modulate the fluorescence excitation light. Three images with shifted patterns are recorded and subtracted. The out-of-focus contributions in each image are similar and are reduced in the difference image, while the in-focus information is not attenuated. However, this technique is slow (compared to traditional widefield imaging) and relies on a stripe pattern that is not distorted by inhomogeneities in the sample.

As shown in this work, optical sectioning in fluorescence microscopy can be achieved in a simple and direct manner. A separate optical path is used for the illumination, which confines the excitation of fluorescence to a limited volume. In a Selective Plane Illumination Microscope (SPIM) the sample is illuminated orthogonally to the detection axis (Fig. 3.3).

The excitation light is focused by a cylindrical lens to a sheet of light that illuminates only the focal plane of the detection objective, so that no out-of-focus flu-

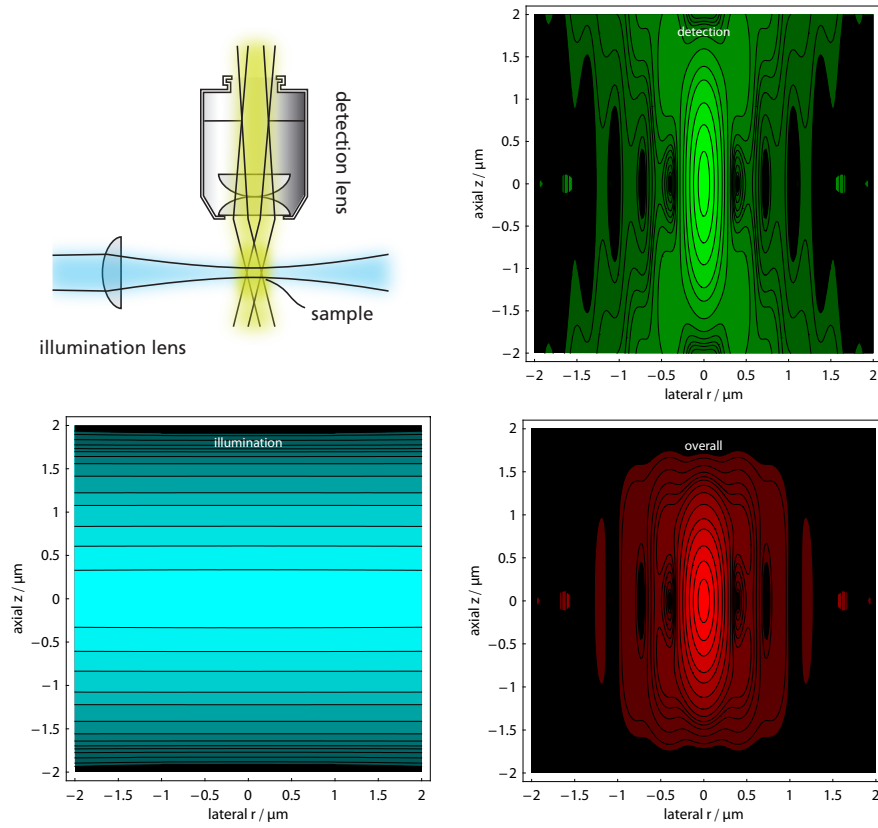


Fig. 3.3 Arrangement of illumination and detection lenses and intensity point spread functions (PSF) in the SPIM. The light sheet illuminates the focal plane of the detection system (top left). The theoretical overall PSF (bottom right) is obtained by multiplying the illumination (bottom left) and detection PSF (top right). $\lambda_{\text{ill}} = 488 \text{ nm}$, $\lambda_{\text{det}} = 520 \text{ nm}$, $\text{NA}_{\text{ill}} = 0.15$, $\text{NA}_{\text{det}} = 0.8$, $n = 1.33$. Same contour lines and LUT as in Fig. 1.2.

orescence is generated. Illuminating only the in-focus volume provides optical sectioning, not by rejecting out-of-focus light (as in a CLSM and in the method by *Neil et al.* (1997)), but by avoiding its generation in the first place. The idea of separating illumination and detection has been previously demonstrated to improve axial resolution in confocal microscopy (theta principle, section 1.1.6).

Because the whole focal plane is illuminated at once, the image can be collected with a widefield detector (e. g. CCD camera) and no time-consuming scanning is required. The sectioning effect in the SPIM is similar to that in the confocal microscope, because the illumination has a profile along the detection axis that is similar to the integral of the overall confocal PSF along the detection axis shown in Fig. 3.1. However, because of the orthogonal arrangement of illumination and detection no out-of-focus light is generated, and parts of the sample that are not imaged are not affected by the light.

The SPIM is characterized by

Selective Plane Illumination microscope

1. two separate optical systems for illumination and detection,
2. light-sheet illumination (optical sectioning),
3. widefield detection (e. g. with a camera),
4. rotation of the sample allows multi-view combination.

The imaging properties (resolution, sectioning) of the SPIM are again described by the PSF. As in the confocal (1.9) and in the theta microscope (1.12) the overall PSF is the product of illumination and detection PSF (Fig. 3.3)

$$|h_{\text{spim}}(x, y, z)|^2 = |h_{\text{ill}}(x, y, z)|^2 \cdot |h_{\text{det}}(x, y, z)|^2 \quad (3.4)$$

Variants of light sheet illumination have been utilized in oceanography to image bacteria (*Fuchs et al.*, 2002) following an idea introduced by *Siedentopf and Zsigmondy* (1903) and in 3D light scanning macrography to scan the surfaces of small specimens (*Huber et al.*, 2002).

3.1.2 Light sheet thickness

For optimal performance the light sheet thickness is adapted to the detection optics. Ideally, the NA of the illumination system is such that the light sheet has a uniform thickness across the full field of view (FOV) of the camera d_{FOV} . At the same time it is made as thin as possible. However, the light sheet will always be thinnest at the focus of the illumination optics. A good compromise is to choose the NA of the illumination system such that the light sheet is twice as thick on

the edge of the FOV as in the center.

$$w\left(\frac{d_{\text{FOV}}}{2}\right) = 2w_0, \Rightarrow d_{\text{FOV}} = \frac{\sqrt{3}n\pi w_0^2}{\lambda_{\text{ill}}} \quad (3.5)$$

Hence, the light sheet width depends on the diameter of the detection field of view, and thereby on the detection magnification M , as

$$w_0 = \sqrt{\frac{\lambda_{\text{ill}} d_{\text{FOV}}}{2\sqrt{3}n\pi}} \propto \frac{1}{\sqrt{M}}. \quad (3.6)$$

The FWHM is given by the relation

$$\text{FWHM} = \sqrt{2\ln 2} w_0, \quad (3.7)$$

and the numerical aperture of the illumination is obtained from

$$\text{NA} = \frac{\lambda}{n\pi w_0}. \quad (3.8)$$

For example a $5\times$ objective lens gives a field of view of 1.32 mm with a typical camera (1024 pixels, $6.45 \mu\text{m}/\text{px}$). Hence, the optimal illumination NA is 0.018 with a FWHM of $7.86 \mu\text{m}$ in the center of the FOV. See the appendix for a table summarizing relevant parameters of detection and illumination for common lenses in the SPIM. The profile of the light sheet that is used for the $5\times$ lens is shown in Fig. 3.4, in which the optical sectioning of the SPIM is readily apparent.

There are two aspects of the light sheet that are relevant to the SPIM: (1) the light sheet provides optical sectioning, and the extent of this sectioning depends on the thickness of the light sheet; (2) the light sheet significantly improves the axial resolution if it is thinner than the axial extent of the detection PSF (this case is shown in Fig. 3.3). The axial resolution is then dominated by the light sheet thickness and not by the detection lens NA.

If we approximate the PSFs describing illumination and detection by Gaussian functions we get

$$|h_{\text{SPIM,det}}(x, y, z)|^2 \propto e^{-2x^2 w_{\text{det,lat}}^{-2} - 2y^2 w_{\text{det,lat}}^{-2} - 2z^2 w_{\text{det,ax}}^{-2}} \quad (3.9)$$

$$|h_{\text{SPIM,ill}}(x, y, z)|^2 \propto e^{-2x^2 w_{\text{ill,ax}}^{-2} - 2y^2 w_{\text{ill,lat}}^{-2} - 2z^2 w_{\text{ill,lat}}^{-2}} \quad (3.10)$$

the multiplication of the two yields

$$|h_{\text{SPIM}}(x, y, z)|^2 \propto e^{-2x^2 (w_{\text{det,lat}}^{-2} + w_{\text{ill,ax}}^{-2}) - 2y^2 (w_{\text{det,lat}}^{-2} + w_{\text{ill,lat}}^{-2}) - 2z^2 (w_{\text{det,ax}}^{-2} + w_{\text{ill,lat}}^{-2})} \quad (3.11)$$

$$= e^{-2x^2 w_{\text{lat}}^{-2} - 2y^2 w_{\text{lat}}^{-2} - 2z^2 w_{\text{ax}}^{-2}} \quad (3.12)$$

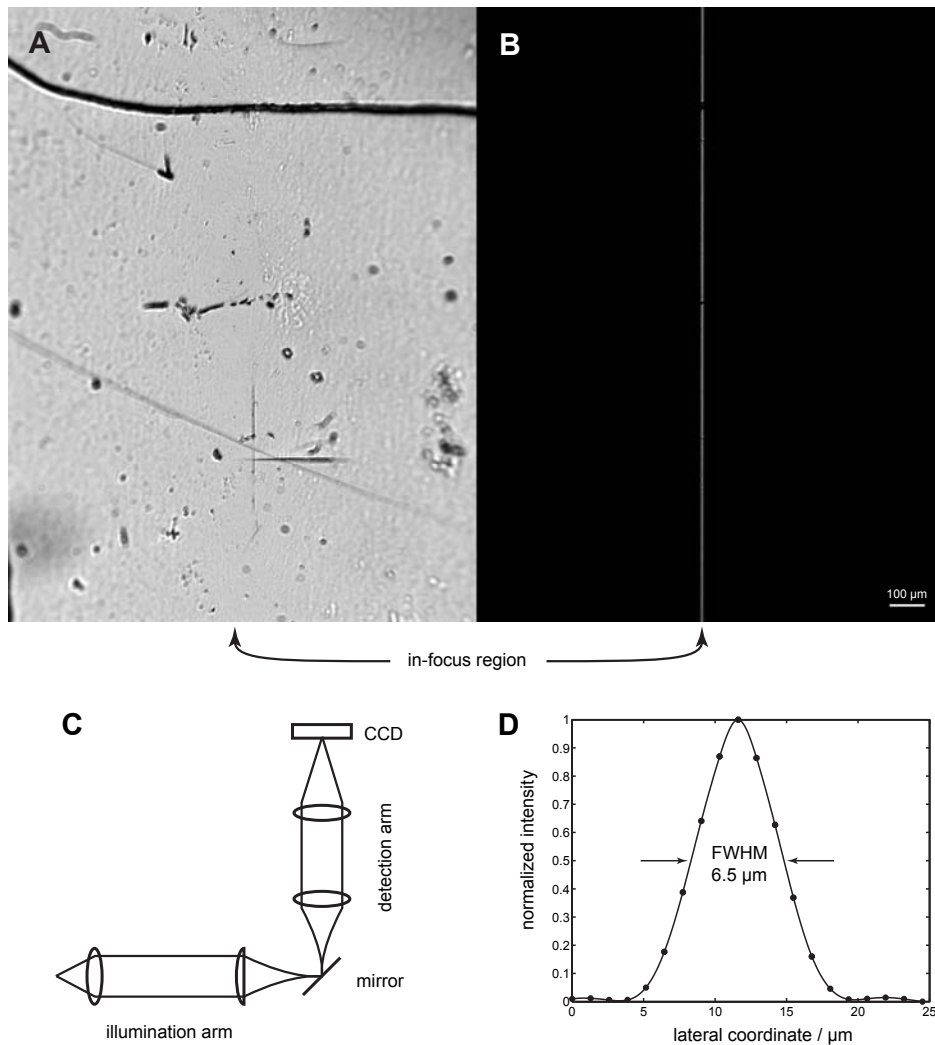


Fig. 3.4 Sectioning performance of the SPIM in reflection mode. The image of a mirror surface is shown, taken with the Fluar 5 \times , 0.25 lens with (A) plain illumination (lamp) and (B) SPIM illumination. The configuration is shown in the inset (C). In (A) the large depth of focus and the lack of sectioning is obvious. In contrast the SPIM provides sectioning and reduces the depth of focus (B). (D) shows the profile of the light sheet: the FWHM is 6.5 μm . (Huisken *et al.*, 2004b)

with

$$\frac{1}{w_{\text{lat}}^2} = \frac{1}{w_{\text{det,lat}}^2} + \frac{1}{w_{\text{ill,ax}}^2} \approx \frac{1}{w_{\text{det,lat}}^2} \quad \frac{1}{w_{\text{ax}}^2} = \frac{1}{w_{\text{det,ax}}^2} + \frac{1}{w_{\text{ill,lat}}^2}. \quad (3.13)$$

The lateral resolution of the SPIM is not influenced by the illumination because of its uniformity perpendicular to the detection axis. In contrast the axial resolution can be dominated by the lateral extent of the light sheet if this is significantly smaller than the axial extent of the detection PSF. However, the axial resolution cannot become worse than the axial resolution of the detection lens if the light sheet is much thicker. In this case, while the light sheet does not significantly decrease the size of the PSF, it can still contribute to the image quality by providing optical sectioning.

It is important to note that even if the light sheet is thicker than the axial extent of the objective PSF, it can still significantly improve the resolution in a thick fluorescent sample. This is because in practice the resolution is affected by the image contrast (*Stelzer, 1998*). In a $500\,\mu\text{m}$ thick sample imaged in the SPIM with a $10\,\mu\text{m}$ wide light sheet, the contrast will be improved by a factor of up to $50\times$ compared to imaging with uniform illumination. In addition to this, in the SPIM a further increase in resolution can be obtained by multi-view reconstruction.

3.1.3 Imaging in heterogeneous tissue

Despite the optical sectioning capabilities, the high resolution, and the good penetration depth of the SPIM, it can, like any fluorescence imaging system, suffer from scattering and absorbing tissue between the excited structures and the detection system: in large and highly scattering samples the image quality decreases as the optical path length in the sample increases. This problem can be compensated by multi-view reconstruction, in which multiple 3D data sets of the object are collected from different directions and combined in a post-processing step (section 1.2). The high-quality information about the sample is extracted from each data set and merged into a single, superior 3D image. It was shown in chapter 1 that this can be done with parallel image acquisition by using more than one lens for the detection of the fluorescence in the MIAM.

3.2 The Selective Plane Illumination Microscope

3.2.1 Setup

Fig. 3.5 shows the major components of the SPIM. A series of lasers (HeNe, Ar-ion) provide lines for fluorescence excitation (e.g. 488 nm, 543 nm). An optical system, which includes a cylindrical lens, focuses the laser light to a thin light sheet. The sample is mounted in a transparent, low concentration (0.5 %) agarose gel. This agarose is prepared from an aqueous solution adequate for the sample, in our case phosphate buffered saline (PBS), providing a suitable biological environment for a live sample. The cylinder of agarose containing the sample is immersed in PBS, which virtually eliminates refractive imaging artifacts at the agarose surface. The cylinder containing the sample is held from above by a translation and rotation micropositioning device. By using the four available degrees of freedom, the sample can be positioned such that the excitation light illuminates the plane of interest.

An objective lens, a detection filter and a tube lens are used to image the distribution of fluorophores in the illumination plane onto a CCD camera (Hamamatsu Orca-ER, 12 bit, 1344×1024 pixels). For this purpose the detection axis is arranged perpendicular to the axis of illumination. A variety of lenses (preferably designed for imaging in water without a cover slip) can be used, with magnifications ranging from $2.5\times$ to $100\times$. The light sheet thickness is adapted to the detection lens, i.e. the light sheet is made as thin as possible while keeping it approximately uniform across the field of view of the objective lens. Its thickness is typically between 2 and $8\text{ }\mu\text{m}$. Translation of the sample along the detection axis and successive image acquisitions deliver a three-dimensional data stack representing the sample's fluorophore distribution. Fig. 3.6 shows a three-dimensional representation and a photograph of the setup.

The technique of selective plane illumination intrinsically provides optical sectioning, since no out-of-focus light is generated. This is demonstrated in Fig. 3.7 for a sample of fluorescent beads $1\text{ }\mu\text{m}$ in diameter. A dramatic improvement in the axial resolution is clearly visible. Whereas the widefield picture shows no sectioning, the data set taken with light sheet illumination shows a dramatic reduction in the axial extent of the beads.

3.2.2 Data collection for multi-view reconstruction

In the SPIM the data for multi-view reconstruction is collected sequentially by generating multiple stacks of images and rotating the sample between each stack. Sample deformations during rotation are avoided because the rotation axis is vertical (parallel to gravity), with the illumination and detection axes in the hori-

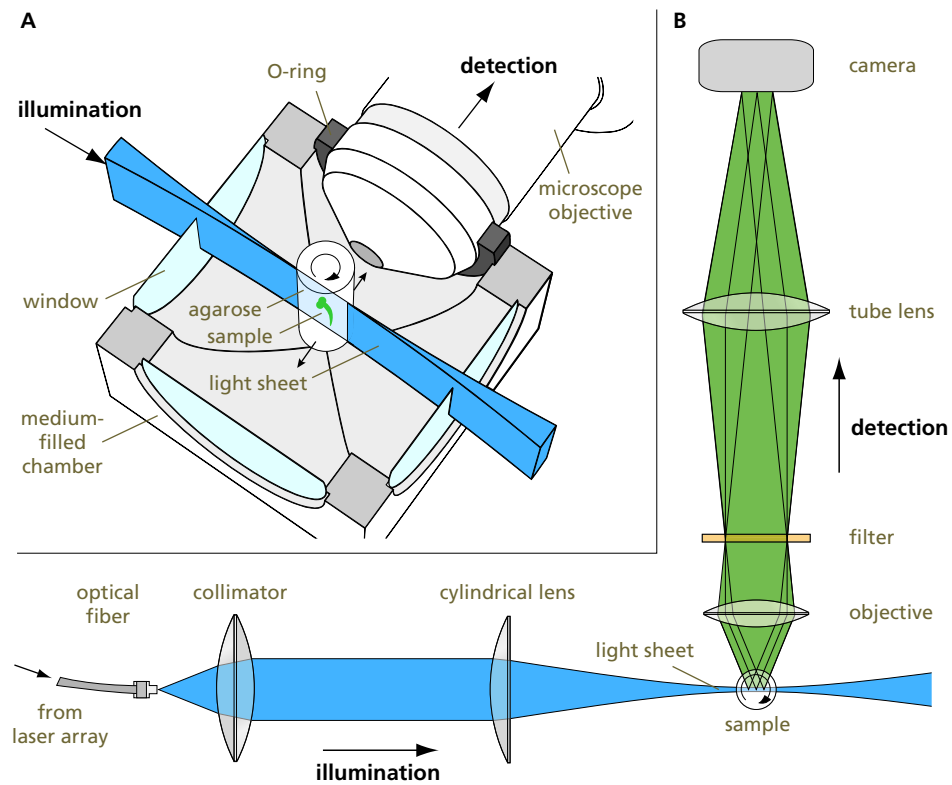


Fig. 3.5 Selective Plane Illumination Microscope. (A) Schematic of the sample chamber. The sample is embedded in a cylinder of agarose gel. The solidified agarose is extruded from a syringe (not shown) that is held by a mechanical translation and rotation stage. The agarose cylinder is immersed in an aqueous medium, which fills the chamber. The sheet of excitation light enters the chamber through a thin glass window. The microscope objective lens, which collects the fluorescence light, also dips into the medium with its optical axis orthogonal to the plane of the excitation light. The objective lens is sealed with an O-ring and can be moved axially to focus on the plane of fluorescence excited by the light sheet. In a modified setup, for low magnification lenses not corrected for water immersion, a chamber with four windows and no O-ring is used. In this case, the objective lens images the sample from outside the chamber. (B) Basic components of the microscope. Laser light emanating from a fibre is collimated. A cylindrical lens focuses the light in one dimension and forms a light sheet that penetrates the sample. This plane of illumination is then imaged onto a camera by a microscope objective lens and a tube lens. The fluorescence emission filter is required to reject scattered excitation light and to select the spectral detection band. (Huisken *et al.*, 2004b)

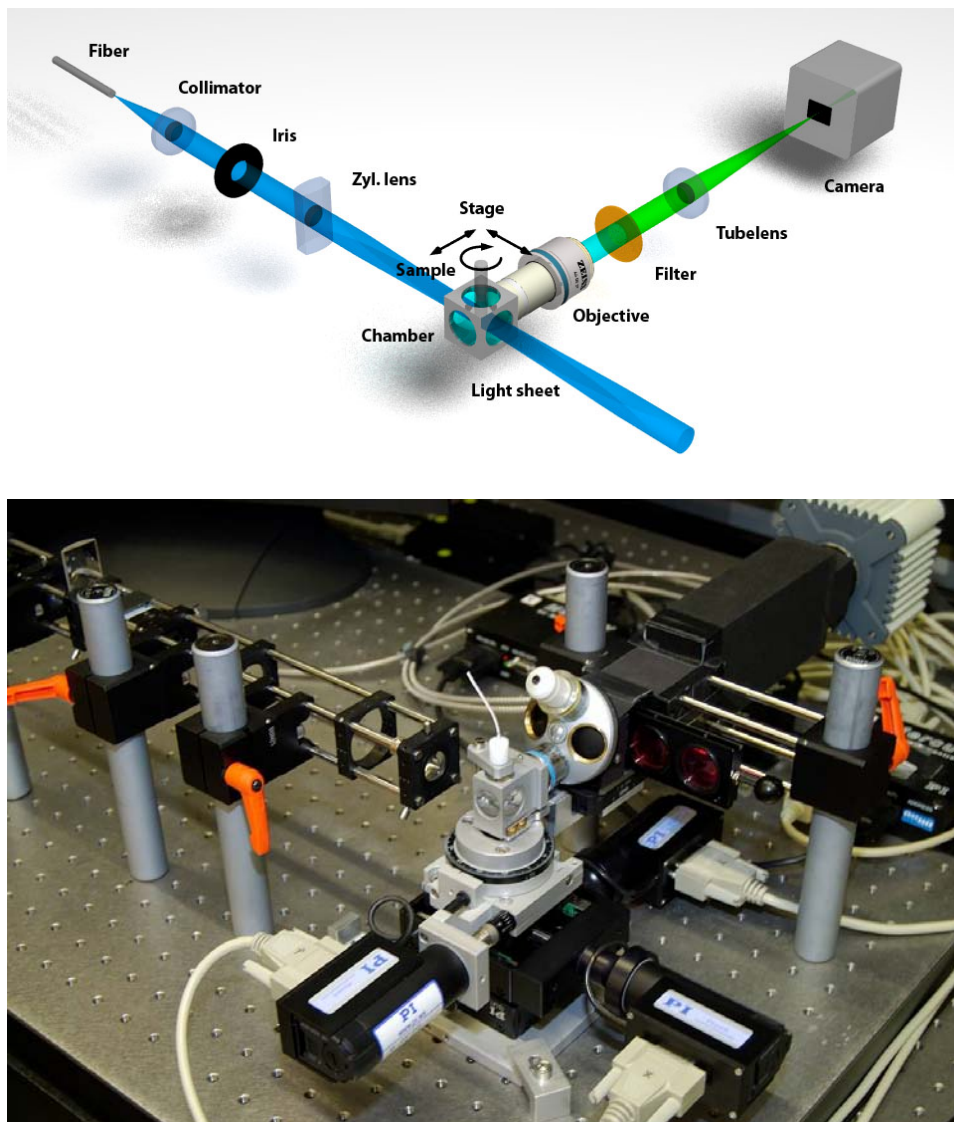


Fig. 3.6 Schematic of the major components of the SPIM (top) and a photograph showing the microscope in the same orientation (bottom).

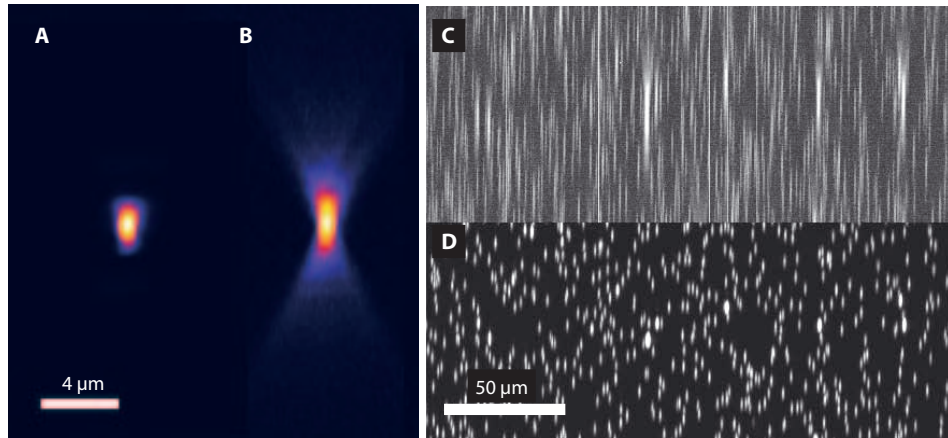


Fig. 3.7 1 μm fluorescent beads imaged in the SPIM with light sheet illumination (A,D) and conventional illumination (B,C). Maximum value projections along y , perpendicular to the detection axis are shown. In A and B a single bead is shown in false colors with a logarithmic look-up-table.

zontal plane (see Fig. 3.5). In contrast to other tomographic reconstruction techniques (e. g. *Sharpe et al. (2002)*), which require extensive processing of the data to yield any meaningful 3D image, the rotation and subsequent data processing are optional in the SPIM. They allow a further increase in image quality and axial resolution compared to a single stack, but in many cases a single, unprocessed 3D SPIM stack alone can provide the desired information about the sample.

3.2.3 Image processing outline

A single 2D slice acquired with the SPIM has a maximum size of 1344 by 1024 pixels (pixel pitch in the camera is $6.45\mu\text{m}$) and a dynamic range of 12 bits. An axial stack is acquired with a step size of $0.5\mu\text{m}$ to $5\mu\text{m}$ between slices. For the multi-view reconstruction, multiple stacks are recorded, rotating the sample between stacks. Most multi-view data sets consist of 4-8 views with 200-300 planes per stack. A time lapse function allows consecutive recordings over time.

The data processing stages required for the fusion of our multi-view SPIM images are (similar to the processing steps performed for the MIAM data, section 1.3):

1. Pre-processing

This includes cropping of the region of interest in all three dimensions (to reduce computation times), rescaling along the detection axis (to make the lateral and axial voxel dimensions equal), and rotation of the data sets.

2. Registration

This is the process of aligning the different views of the sample so that features visible in more than one view overlap spatially. For the purpose of

the registration, the stacks are high-pass filtered (to reduce background-induced artefacts) and cross-correlated. The position of the resulting correlation peak determines the translation that is applied to register the pre-processed images obtained in step I.

3. Fusion (as described in section 1.3)

The final stage is to fuse the pre-processed and registered views into a single, optimal image, i. e. to extract the high resolution features from each view and combine them into a single data set. The data sets were fused by:

- (a) Fourier transforming the individual views, yielding complex value data sets.
- (b) For each spatial frequency (i. e. each voxel in Fourier space), we select the (complex) value from the view with the largest magnitude, and insert it into the new, fused data set.
- (c) Inverse Fourier transforming to obtain the final, fused image.

Because the data stacks were quite large (there are $1201 \times 659 \times 688$ voxels in the data sets shown in Figs. 3.9, 3.10, and 3.11, next section), the fusion was done sequentially on smaller sub-regions from which the final data set was assembled as a 3D mosaic. This not only simplifies the processing of large data sets, but also permits different views to determine the weighting of the same spatial frequency in the different sub-regions of the sample. Thus only the high-information-content portions of each view contribute to the final fusion.

If the data sets overlap sufficiently in the multi-view reconstruction, the lateral detection resolution determines the system resolution, i. e. ideally the multi-view reconstruction compensates the poor axial resolution from any single view with information from others, and provides a nearly isotropic resolution (as in the MIAM, see chapter 1).

The above algorithm is non-iterative, which makes it possible to implement it in a reasonably computationally efficient form. For the processing of the images presented in this work, the algorithms were implemented in MATLAB 6.1, running on a 1.8 GHz Windows 2000 based personal computer. The total processing time required to produce the Medaka fusion (next section) was ≈ 24 hours; however, the processing time can be reduced considerably by implementing the algorithms in an optimized, compiled computer language.

The above processing algorithm is in principle applicable to other optical microscopies. However, the traditional method of mounting the sample between a glass slide and a cover slip means that recording stacks from multiple directions is not generally practical.

3.3 Example 1: Medaka fish embryo

To demonstrate the sectioning capability of the SPIM deep inside extended objects Fig. 3.8 shows a four day old fixed medaka (*Oryzias latipes*) fish embryo (stage 32, *Iwamatsu* (1994)). Medaka is a well established model organism for studies of vertebrate genetics and development (*Wittbrodt et al.*, 2002). The transgenic line *Arnie* was generated by injecting medaka embryos at the one cell stage with a construct containing 5 Kb of Fugu genomic region upstream of the fugu *Ath5* gene and the GFP coding region as reporter, flanked by I-Sce meganucleases recognition sites (*Thermes et al.*, 2002). The *Arnie* line shows GFP expression in the ganglion cells, driven by the Fugu *Ath5* promoter, as well in the developing muscle tissue, by an enhancer trap effect. Four day old embryos were fixed for one hour in 4% PFA/PBS and then dechorionated. The yolk was then removed and the embryo was mounted in a low melting temperature agarose cylinder and imaged in the SPIM. The maximum intensity projections of the stack (3.8) clearly illustrate that SPIM can provide high resolution (better than $5\ \mu\text{m}$) as deep as $400\text{--}500\ \mu\text{m}$ inside the fish. According to our experience such penetration depths are not possible using a CLSM. The lateral resolution of the SPIM is generally limited either by the NA of the detection lens or the pixel size of the camera. For the data set presented an area of $1.5 \times 0.85\ \text{mm}^2$ is imaged with a 1.4 megapixel camera. In this case, the lateral resolution of the detection lens ($1.1\ \mu\text{m}$ for the $5\times$, 0.25 lens) is not fully exploited and the images are undersampled (*Stelzer*, 1998).

The restoration process in a multi-view reconstruction is demonstrated with four stacks taken from four orientations of the same sample. Figure 3.9 shows four pre-processed data sets projected along two axes. Regions in the single views that contributed most to the final result were those requiring minimal optical path lengths inside the sample.

Combination of these stacks by image processing in Fourier space (section 1.3) yields a complete view of the sample, which is ca. 1.5 mm long and ca. 0.9 mm wide. The drop in image quality with penetration depth is compensated in the fused stack. No noticeable degradation deep in the sample or elongation of features along any of the four detection axes remain visible (Fig. 3.10). Figure 3.11 shows volume renderings of the individual views and the fused data.

Fusion of the data sets yields an increased information content in the resulting reconstruction in regions that were obscured (by absorption or scattering in the sample) in some views. This is possible because information about regions of the sample that were poorly imaged in one orientation is provided by data sets taken with another orientation. If the data sets sufficiently overlap in multi-view reconstruction, the lateral resolution also determines the axial resolution, i. e. the multi-view reconstruction compensates the poor axial resolution from any single view with information from others, and provides a nearly isotropic

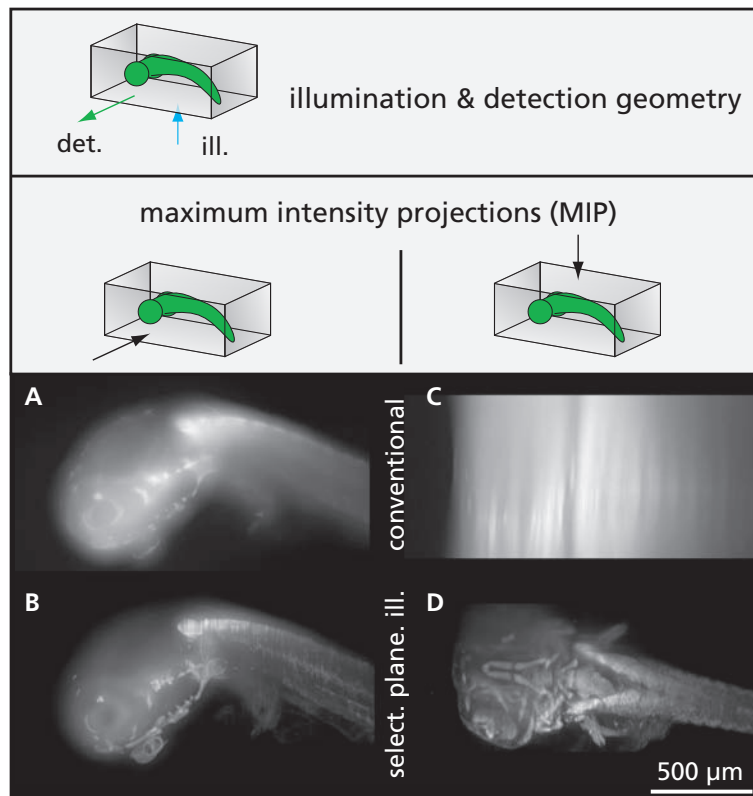


Fig. 3.8 Medaka embryo imaged in the Selective Plane Illumination Microscope by two different modes of illumination. Lateral (A,B) and dorsal-ventral (C,D) maximum projections are shown. A,C: Demonstrating the imaging properties of a conventional widefield microscope, the sample was illuminated without the cylindrical lens, resulting in a uniform illumination (no light sheet). There is no optical sectioning; the elongation of fluorescent features along the detection axis is clearly visible (C). In contrast, the selective plane illumination (B,D) provides optical sectioning. Here, the excitation light was focused to a light sheet by the cylindrical lens. Both image stacks were taken with a Zeiss Fluar 5 \times , 0.25 objective lens. (Huisken *et al.*, 2004b)

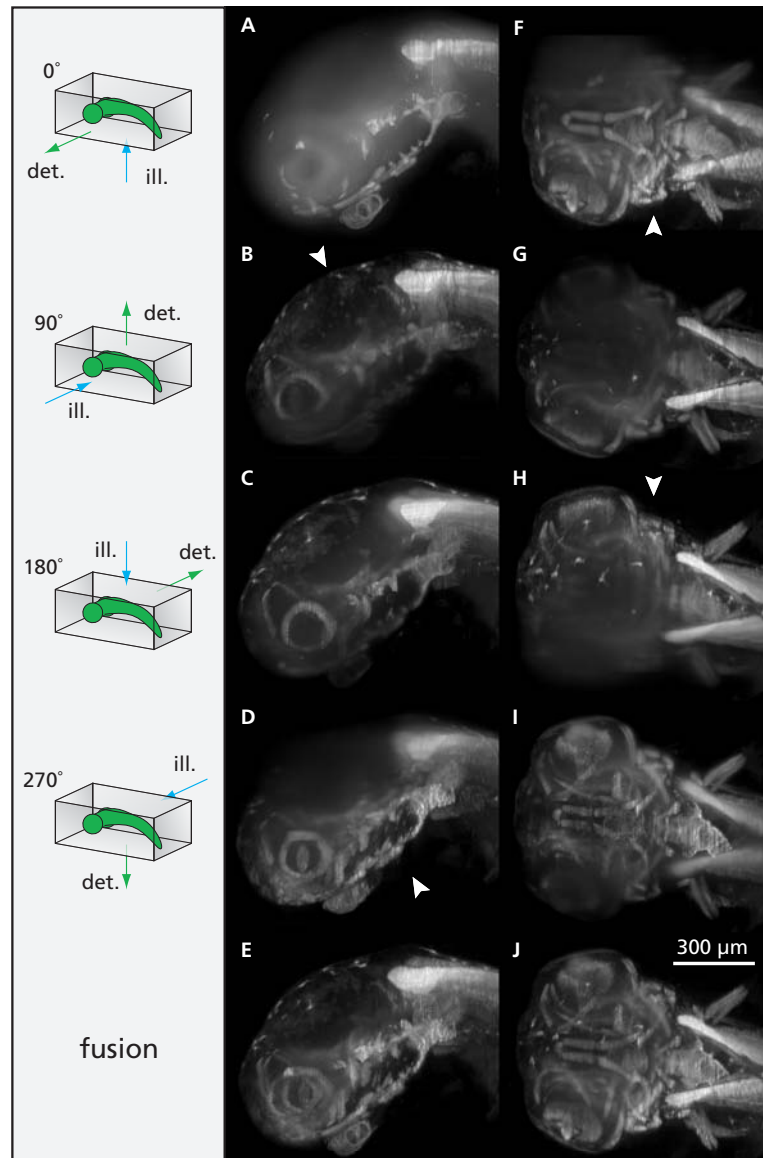


Fig. 3.9 Medaka embryo (same as in Fig. 3.8) imaged in the SPIM with different orientations. The sample was rotated mechanically and for each orientation (0°, 90°, 180°, 270°) a stack was recorded. The stacks were then re-oriented in the computer to align them with the stack recorded at 0°. Lateral (A-E) and dorsal-ventral (F-J) maximum projections are shown. Particularly well resolved are parts that were close to the detection lens and facing the illumination plane (arrow heads). E.g. the left eye is best resolved in the orientation 0° (F) whereas the right eye is best seen in view H (180°). The fusion of these four data stacks yields a superior representation featuring similar clarity and resolution throughout the entire specimen (E,J). The image combination procedure inherently favors well resolved and bright over poorly resolved and less well visible features. Images were taken with a Zeiss Fluar 5×, 0.25 objective lens. (Huisken *et al.*, 2004b)

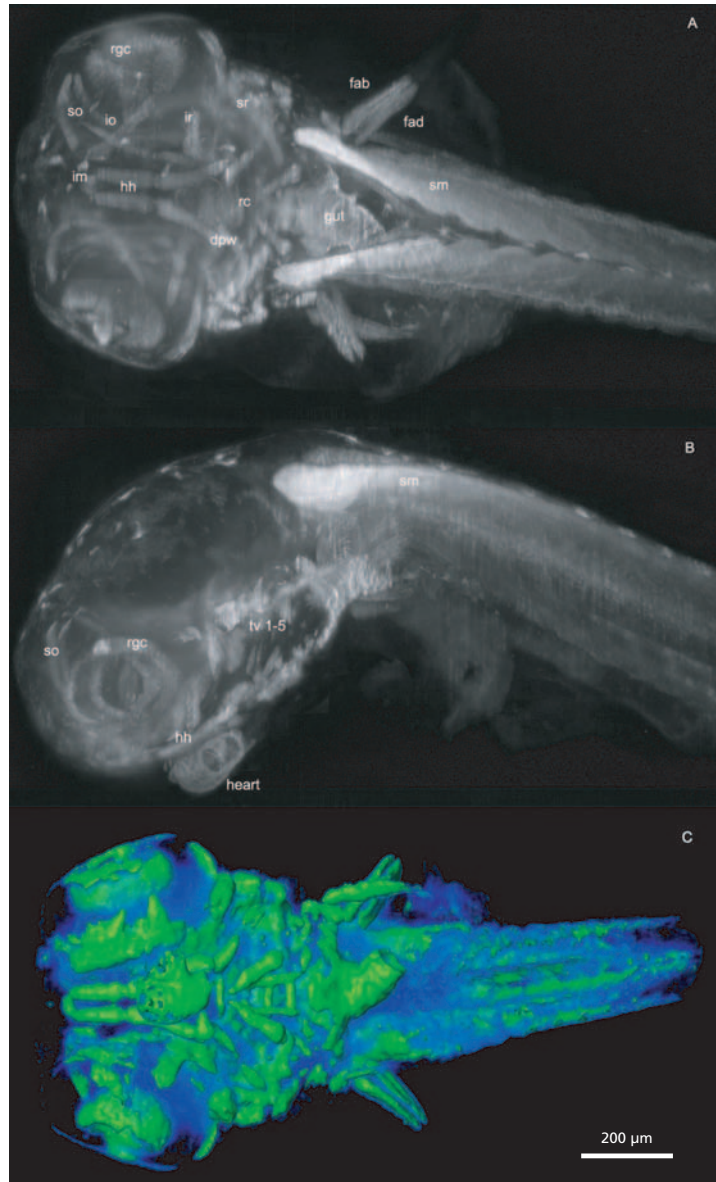


Fig. 3.10 Dorsal-ventral (A) and lateral (B) maximum-intensity projections of the fused data set from Fig. 3.9. The high resolution throughout the entire fish allows one to identify labelled tissue: rgc, retinal ganglion cells; so, superior oblique; io, inferior oblique; ir, inferior rectus; sr, superior rectus; im, intermandibularis; hh, hyohyal; rc, rectus communis; dpw, dorsal pharyngeal wall; fad, fin adductor; fab, fin abductor; sm, somitic mesoderm; tv, transverse ventrals. The stack has a size of $1201 \times 659 \times 688$ pixels ($1549 \mu\text{m} \times 850 \mu\text{m} \times 888 \mu\text{m}$). (C) volume rendering showing a ventral view of the fish. (Huisken *et al.*, 2004b)

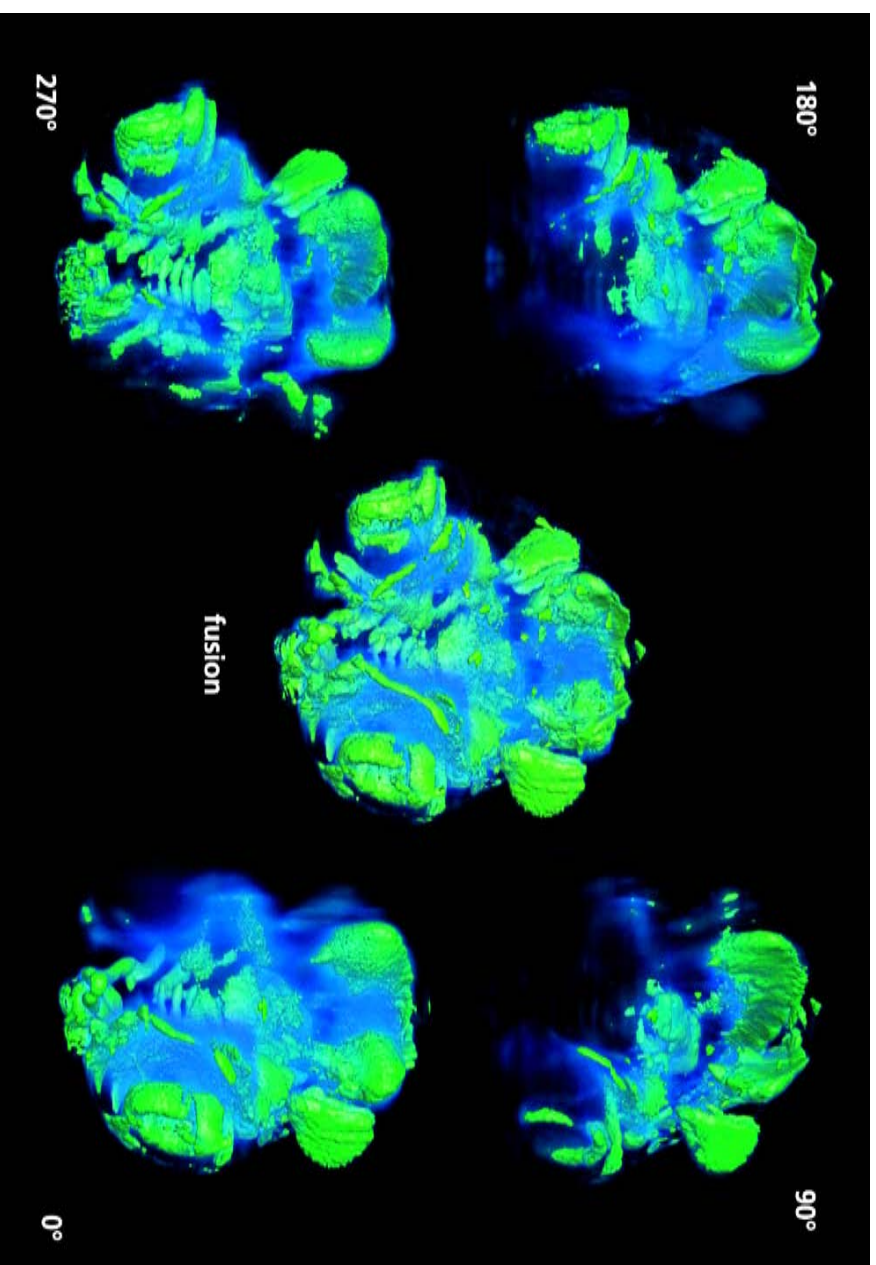


Fig. 3.11 Volume rendering of the data sets shown in Fig. 3.10 in an anterior orientation. The four pre-processed data sets are shown on the outside, and the fused image stack is in the figure. The fused data set represents a complete image of the fish and all details from the individual data sets are preserved. (*Huisken et al., 2004b*)

resolution. Even though a total of 1000 images were taken, photo bleaching was negligible due to the economical use of excitation light and the efficient collection of fluorescence light.

3.4 Example 2: *Drosophila melanogaster*

The method of embedding the sample in a low concentration agarose cylinder is one that can be efficiently employed with live specimens. Live medaka and *drosophila melanogaster* embryos were successfully imaged over periods of up to three days without detrimental effects on the embryogenesis and development of the sample. As an example a time-series of the complete embryogenesis of the widely studied model organism, the fruit fly *drosophila melanogaster*, is shown in Fig. 3.12. GFP-moesin labels the plasma membrane throughout the embryo (*Edwards et al.*, 1997). Slices are shown at depths of 49 and 85 μm of a single stack at different time points. Even without multi-view reconstruction, features inside the embryo are identifiable and traceable. Stacks (56 planes each) were taken every 5 minutes over a period of 17 hours in an automated fashion, without refocussing or realignment. Even after being irradiated 11480 times the fly embryo remained healthy and the embryogenesis completed normally.

It is also possible to use the SPIM technique for higher magnification and resolution imaging, as demonstrated in Fig. 3.13, which shows slices from a single-view SPIM stack. Here the pole cells of a *Drosophila* embryo in the cellular blastoderm stage are imaged with a NA = 0.8 water dipping lens at a resolution well below 1 μm . The individual cell membranes and the distribution of the spherical pole cells on top of the hexagonal somatic cells and the cortex are clearly visible. Although there is some degradation of image quality with depth (the side of the sample on which the illumination is incident, i. e. the bottom in Fig. 3.13, is sharper than the opposite side), even without multi-view image fusion the optical sectioning provided by the SPIM allows imaging of the interior of this optically diffuse embryo.

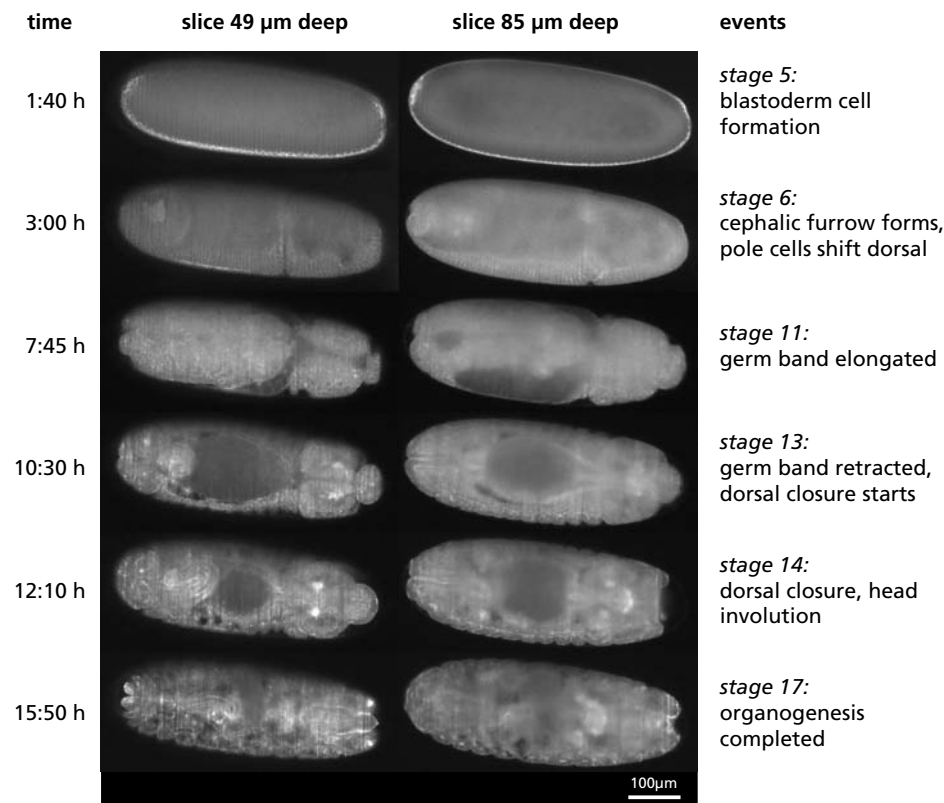


Fig. 3.12 Time-lapse of *drosophila melanogaster* embryogenesis. Six out of 205 time points acquired are shown. At each time point 56 planes were acquired, from which two are here shown at depths of 49 μm and 85 μm below the cortex. No multi-view reconstruction was performed. The optical sectioning capability and the good lateral resolution are apparent. Despite the optically dense structure of the *drosophila* embryo, features are well resolved at these depths in the sample. For this figure, the images were oriented such that the illumination occurs from below. This results in a slight drop in intensity and clarity from the bottom to the top (of each slice). Nevertheless, the information content across the embryo is nearly uniform, single cells can be tracked over time, and the overall movements and embryonic events can be followed. The images were normalized to exhibit the same overall intensity, thus compensating the continuous production of GFP-moesin. The stages and the prominent events are listed on the right. 205 stacks at 5 min intervals were taken with a Zeiss Achroplan 10 \times , 0.30W objective lens (56 planes per stack at 4 μm spacing): 11480 images in total. (Huisken *et al.*, 2004b)

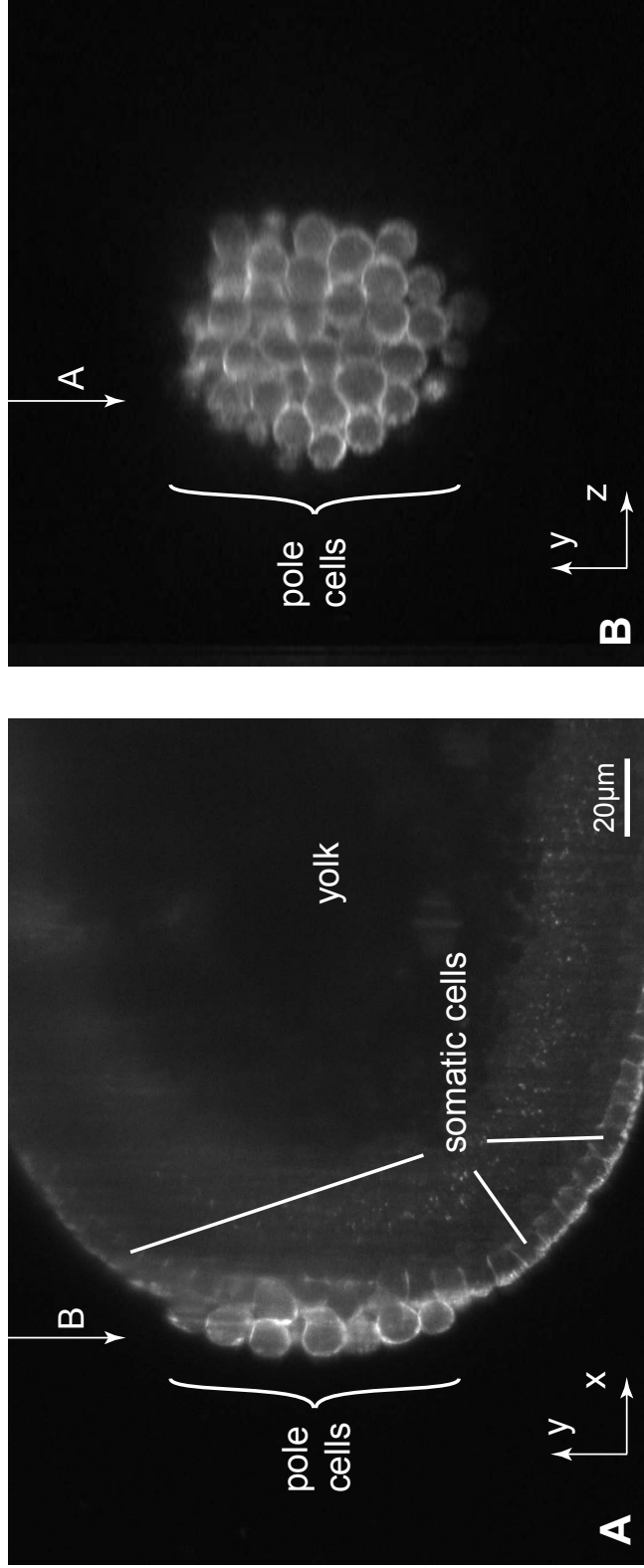


Fig. 3.13 Pole cells of a *Drosophila* embryo in the cellular blastoderm stage imaged in the SPIM. Two slices of unprocessed data (single view, no multi-view combination) are shown: *x-y*-slice (A) and *x-z*-slice (B) with *z* being parallel to the detection axis. Pixel size is $0.16\mu\text{m}$, plane spacing is $1\mu\text{m}$. (B) has been scaled by a factor of 6.2 along *z* to give an aspect ratio of 1:1. Objective lens: Zeiss Achroplan $40\times$, 0.8. The organism and the labelling are the same as in Fig. 3.12. (Huisken *et al.*, 2004b)

3.5 Performance of the SPIM

3.5.1 Lateral resolution

The lateral resolution of the SPIM is limited either by the NA of the detection lens or the pixel size of the camera. For the Medaka data sets presented an area of $1.5 \times 0.85 \text{ mm}^2$ is imaged with a 1.4 megapixel camera. In this case, the lateral resolution of the detection lens ($1.1 \mu\text{m}$ for the $5\times$, 0.25 lens) is not fully exploited and the images are undersampled (Stelzer, 1998). However, SPIM technology can be applied to any magnification and NA. Water dipping lenses with working distances of 1–3 mm (NA \approx 0.3–1.0) are particularly well suited for the current implementation of the SPIM. The primary niche of the SPIM is in imaging thick, intact samples such as whole embryos of 100s of μm to mm in size, which are generally imaged with relatively low magnification and NA (e. g. $5\times$, NA = 0.25 for the Medaka). They cannot be imaged with high NA lenses because of their intrinsic short working distances of these lenses.

3.5.2 Comparison with confocal microscopy

Optical sectioning in fluorescence microscopy has been obtained in the past mainly by confocal laser scanning microscopy (CLSM, Pawley (1995)). The limited working distance of high numerical aperture (NA) objective lenses, which are required for high-resolution imaging, and the severe drop in signal intensity with increasing depth in heterogeneous specimens are responsible for the limited accessible depth when imaging with a CLSM (see Fig. 3.14).

In a CLSM, fluorescence light is collected during the time the focal spot rests at each pixel (1–10 μs). In contrast, a CCD camera is used in the SPIM to detect fluorescence. Integration times of 0.1 s to 1 s mean that the laser intensity can be decreased, reducing the effects of fluorophore saturation (Pawley, 1995). As an example situation of interest, we compare the power densities used in the imaging for Fig. 3.14. For the confocal images shown in (A) and (C) we estimate a confocal spot size in the sample of $\approx 1.3 \mu\text{m}$ and a total power of $250 \mu\text{W}$, which means a power density of $\approx 20 \text{ kW/cm}^2$. For the SPIM images in (B) and (D) the light sheet was $\approx 10 \mu\text{m} \times 5 \text{ mm}$ and the power $\approx 5 \text{ mW}$, making the power density $\approx 10 \text{ W/cm}^2$. It is clear that although the confocal microscope may suffer from saturation, the SPIM power density is still more than 3 orders of magnitude lower.

Moreover, in a CLSM the process of imaging a single plane illuminates the entire volume of the sample (Fig. 3.15). When a stack of images is required to determine the full 3D fluorophore distribution in a thick sample, excessive photobleaching can occur because the entire sample is illuminated many times. In contrast, in the SPIM only the plane currently being observed is illuminated, and

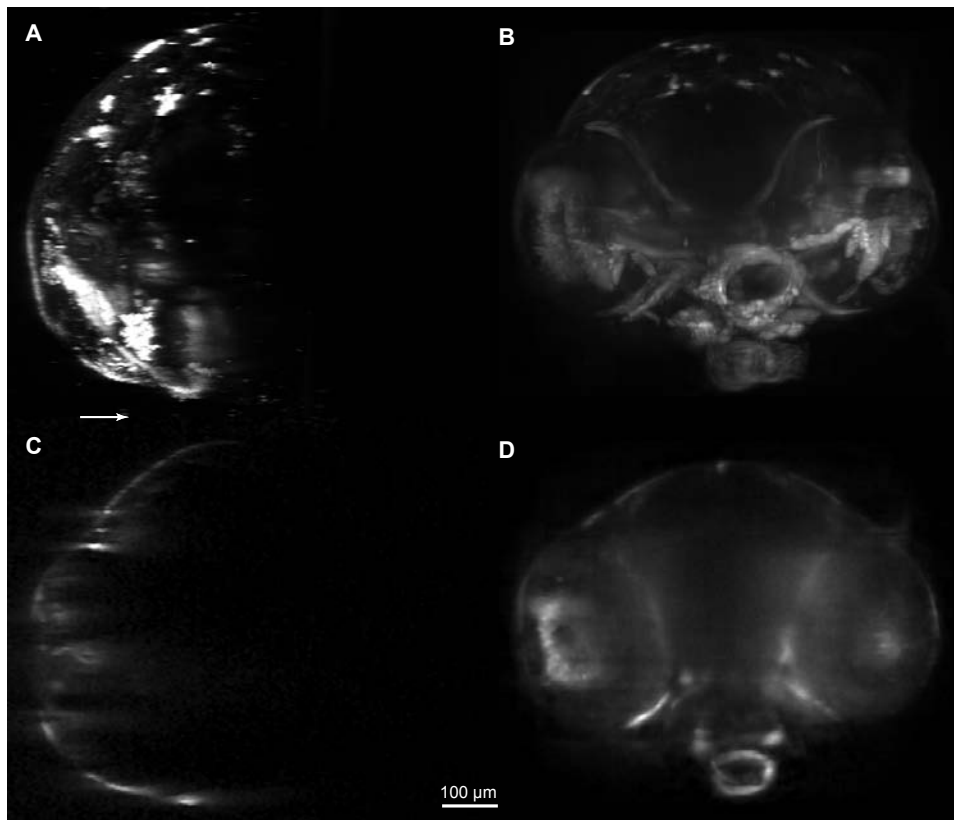
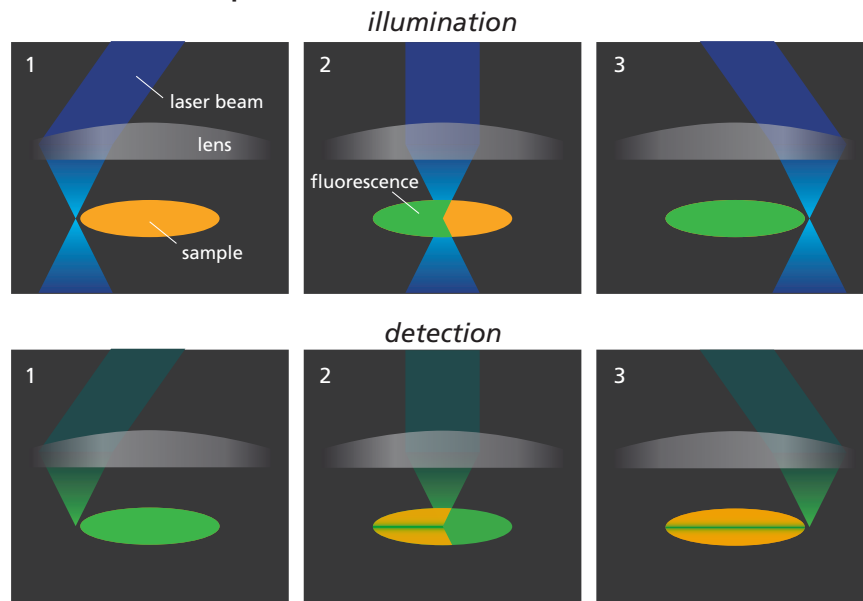


Fig. 3.14 Projections (A,B) and slices (C,D) from 3D reconstructions of the head region of a Medaka *Arnica* embryo, taken with a confocal microscope (A,C) and with the SPIM (B,D). (A,C) The sample was imaged in an inverted Zeiss LSM510 with a C-Apochromat 10 \times , 0.45W. Excitation wavelength 488 nm, detection filter LP510 nm. The direction from which the confocal sample was imaged is indicated by the arrow. (A) Maximum value projection, (C) single slice, gamma = 0.5. (B,D) Fusion of four SPIM views. For all of the individual views, both the illumination and detection axes lie in the plane of the image shown, and the rotation axis was perpendicular to the image. Objective lens: Fluor 5 \times , 0.25; excitation at 488 nm, detection filter: BP500-550 nm. (B) Maximum value projection, (D) single slice. (Huisken *et al.*, 2004b)

A. confocal microscope



B. SPIM

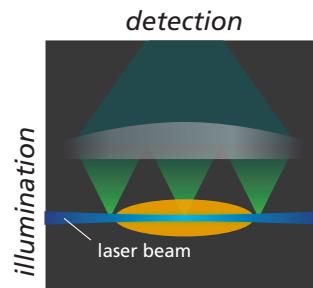


Fig. 3.15 Comparison of the image formation in the confocal microscope (A) and in the SPIM (B). Illumination and detection are shown separately to illustrate that the entire sample is exposed in the confocal microscope as soon as a single plane is scanned. Only in the detection process is out-of-focus light rejected (by the pinhole) and sectioning is achieved. In contrast, in the SPIM only the in-focus plane is illuminated and the rest of the sample is not exposed to the light.

is therefore affected by bleaching (Fig. 3.15). The total number of fluorophore excitations required to image a 3D sample is therefore greatly reduced. Even though a total of 1000 images were taken to generate the data shown in Fig. 3.10, photo bleaching was not noticeable due to the economical use of excitation light and the efficient collection of fluorescence light.

Selective plane illumination intrinsically provides optical sectioning, since no out-of-focus light is generated. In a CLSM, out-of-focus light is generated, but rejected by the pinhole. Moreover, in the CLSM the overall signal decreases as the focal plane is moved deep into scattering tissue, because aberrations cause the confocality to fail. Scattering of the illumination *in any direction* will degrade the confocal image quality. In contrast, in the SPIM only scattering of the illumination in *one dimension* (along the detection axis) causes the broadening of the light sheet that can deteriorate the image quality. Moreover, the low NA used in the illumination ensures that aberrations in the illumination process are minimal (Pawley, 1995).

Figure 3.14 illustrates the differences between confocal and SPIM imaging of Medaka fish embryos. Although the confocal gives excellent resolution near the surface of the sample, the penetration depth is minimal, and very little can be determined regarding the interior structure of this sample (note that contrast enhancement by using $\gamma = 0.5$ was required to make any internal structure visible at all). If one were solely interested in surface features, the confocal system would be ideal, and the resolution could be further improved by using a higher NA objective lens. However, this would absolutely preclude imaging the entire sample because currently available high NA lenses do not have sufficient working distance. In contrast, in the SPIM images one can see details of the structure throughout the sample, although there is naturally some degradation of the resolution towards the center of the embryo.

3.5.3 Penetration depth and aberrations with SPIM

Depending on the optical properties of the sample, there will be aberrations both in the illumination and detection processes. The image quality is degraded the deeper one penetrates into the sample. As with any other microscope, this is true for single data stacks taken with the SPIM. However, in the SPIM we can compensate for these effects by multi-view image fusion. For a given region of the sample, if high resolution information is available in at least one view, the reconstruction algorithm will favor this over the low resolution information in other views. The outcome is a high resolution over a much larger volume than in a single unprocessed stack. If the penetration depth is at least half the thickness of the sample, high resolution throughout the whole sample can be obtained by multi-view combination.

If the illumination beam is scattered or absorbed by features in the sample, shadowing along the illumination direction can appear. These effects may be present in all optical microscopies; however, in the SPIM these effects can be more pronounced because the illumination is collimated, rather than being incident on the sample from many directions. Multi-view combination can compensate for these artifacts, at least in part.

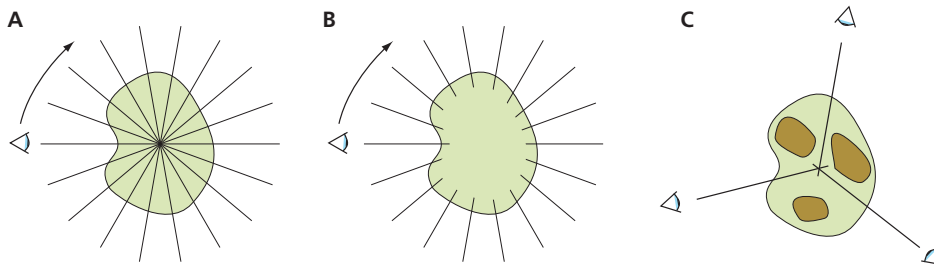


Fig. 3.16 Three examples of applications of the SPIM. (A) Resolution improvement in transparent samples: each stack represents a complete image of the sample, and the stacks overlap. (B) In nearly opaque samples the limited penetration depth only permits images of a thin layer below the surface: a complete overview of the sample's surface is obtained by combining multiple views. (C) By rotation of the sample in the SPIM it is possible to avoid obstacles in the beam paths, and single images or stacks are taken with minimal obstruction.

3.6 Conclusion

In summary, the SPIM is a widefield optical microscope capable of imaging deep inside both fixed and living embryos. By selective illumination of a single plane, the excitation light is efficiently used to achieve optical sectioning and to eliminate photo-damage in parts of the sample that are not imaged. A versatile stage allows positioning and rotation of the sample to orient it for optimal imaging conditions. In addition to single 3D stacks, multi-view reconstruction can combine data sets acquired independently into an optimal representation of the sample. Although the SPIM is only demonstrated in a fluorescence mode in this work, the implementation of other contrasts such as scattered light should be quite straightforward to implement. The system is compact, fast, optically stable, easy to use, and can be constructed for a fraction of the cost of a CLSM or a multi-photon system.

To summarize, there are three categories of applications for which the SPIM has been proven to be useful (Fig. 3.16). In a transparent sample (i. e. the penetration depth is sufficiently high that all multi-view stacks overlap), the multi-view combination yields a resolution improvement in all parts of the sample, and the resolution becomes nearly isotropic (Fig. 3.16A). If the penetration depth is limited each multi-view stack can provide only a surface “tile” of the sample's exterior regions. In this case the fusion of the data represents a stitching of these parts together. Since there is little overlap of the regions imaged in different views, no significant resolution improvement is obtained (Fig. 3.16B). Most samples, however, are between cases A and B. As has been demonstrated for the Medaka sample (section 3.3) the different SPIM views overlap partially, and both an increase in over-all information and a resolution improvement is visible in the fused image (Fig. 3.10). The versatile stage of the SPIM allows rotation of the

sample, which is useful for samples that present obstacles to the beam paths (Fig. 3.16C). Here, the SPIM allows one to orient the sample for optimal imaging conditions. Under these conditions a single SPIM image can be superior to those from other microscopes, where it would have been impossible to reorient the sample to see the feature of interest.

The SPIM has the potential to become the tool of choice for the visualization of gene-expression patterns in a 3D morphogenetic context. Optical sectioning and reduced photo-damage in large samples together with image improvement by multi-view reconstruction are key features when studying embryonic development and its complex 4D transformations. Because of its speed and its fully automatable operation the SPIM is an ideal tool for large scale gene expression studies of developing organisms and the systematic and comprehensive acquisition and collection of expression data to supplement the entries in genome sequence databases. SPIM technology can be readily applied to a wide range of samples, from whole embryos down to single cells, and subcellular resolution can be obtained in live samples kept in a biologically relevant environment. Therefore, SPIM also has the potential to be of great use in the promising fields of 3D cultured cells (*Abbott, 2003*) and 3D cell migration (*Webb and Horowitz, 2003*).

4. Summary and Conclusion

This work presents some advancements in the fields of high resolution fluorescence microscopy and optical manipulation. It demonstrates that the technique of multi-view combination can be applied to 3D microscopy data to overcome some limitations of conventional microscopy: i. e. *directional* variations (anisotropy of the PSF) and *positional* variations of the image quality. Important requirements for the method of multi-view combinations are that the 3D stacks can be registered and that they are not spoiled by deformations of the sample. Both the MIAM (chapter 1) and the SPIM (chapter 3) are shown to fulfill this requirement.

The MIAM has been conceptualized, designed, and build. It represents the first implementation of a multi-view multi-lens microscope. Using four water dipping lenses arranged along the axes of a tetrahedron the sample in the MIAM is imaged simultaneously from four sides. Although the idea of such a microscope is general and can be realized with different objective arrangements and magnifications, we believe that the current implementation of the MIAM is ideally suited for biological samples with sizes from $1\text{ }\mu\text{m}$ to ca. $150\text{ }\mu\text{m}$. Different methods to fuse the images have been evaluated, and Fourier-space based methods are shown to yield excellent results in both the MIAM and the SPIM.

In addition to its multi-view capability, the MIAM incorporates a completely new concept of sample handling. In the MIAM samples can be kept under physiologically relevant conditions, i. e. they do not have to be mounted on a cover slip. The sample can either be embedded in a low concentration agarose gel (as shown in chapter 1) or it can be held and scanned by optical forces of the DAOM (chapter 2). Because of these innovations the MIAM enables new experiments in e. g. developmental and cell biology that can profit from such sample preparation.

The DAOM is a 3D optical manipulator, that allows the experimenter to move the sample over distances of ca. $100\text{ }\mu\text{m}$. This has been impossible with existing trapping techniques such as optical tweezers, which confine the sample to the tight focus of a high NA lens. Moreover, it is demonstrated that the Earnshaw theorem, which states that a trap that relies solely on scattering forces is unfeasible, can be overcome by the implementation of a feedback system. Optical

forces are ideally suited to gently hold and manipulate a sample in a microscope. Therefore, the DAOM fits very well into the concept of the MIAM: it equips the microscope with a tool to move a freely floating sample in a controlled fashion. This is a very gentle way to image a sample in a microscope.

Optical sectioning has been obtained in the past mainly by confocal microscopy. The ability to reject out-of-focus light that can spoil the image in a conventional microscope is of great value in extended samples. However, the confocal microscope fails in imaging large samples because of its limited penetration depth. The SPIM presented in chapter 3 is an optical widefield microscope capable of imaging fluorescence protein expression patterns deep inside both fixed and living embryos. By selective illumination of a single plane the excitation light is efficiently used to achieve optical sectioning and under certain conditions an increase in axial resolution. Because only in-focus features of the sample are exposed to the excitation light, photo-damage in parts that are not imaged is completely eliminated. In the past 18 months SPIM has been used for many biological experiments; examples using the two model organisms Medaka and *Drosophila* are described in detail in this work. They demonstrate that the SPIM achieves deep penetration in fixed and live samples.

The versatile stage and the method of embedding the samples in agarose allows positioning and rotation of the sample to orient it for optimal imaging conditions. Independently acquired 3D data sets are combined by multi-view reconstruction into an optimal representation of the sample. A complete high-resolution protein-expression pattern of a Medaka embryo, ca. 1 mm in diameter, imaged in the SPIM is presented. It is also shown that such data is difficult or impossible to record with conventional or confocal microscopies.

In conclusion, some limitations of existing microscopy techniques are overcome in this work. Image improvement by multi-view reconstruction (in the MIAM and in the SPIM) as well as optical sectioning and reduced photo-damage in large samples (SPIM) enable new biological research from subcellular processes up to embryonic development. Moreover, optical forces (DAOM) and spatial fixation in agarose (MIAM and SPIM) are means to handle fragile samples such as embryos and will enable such studies as the use of 3D cell cultures to investigate the morphology, migration, and interactions of cells in a more realistic context than was possible in the past.

Appendix

Multi-Imaging Axis Microscope (MIAM) and Differential Active Optical Manipulator (DAOM)

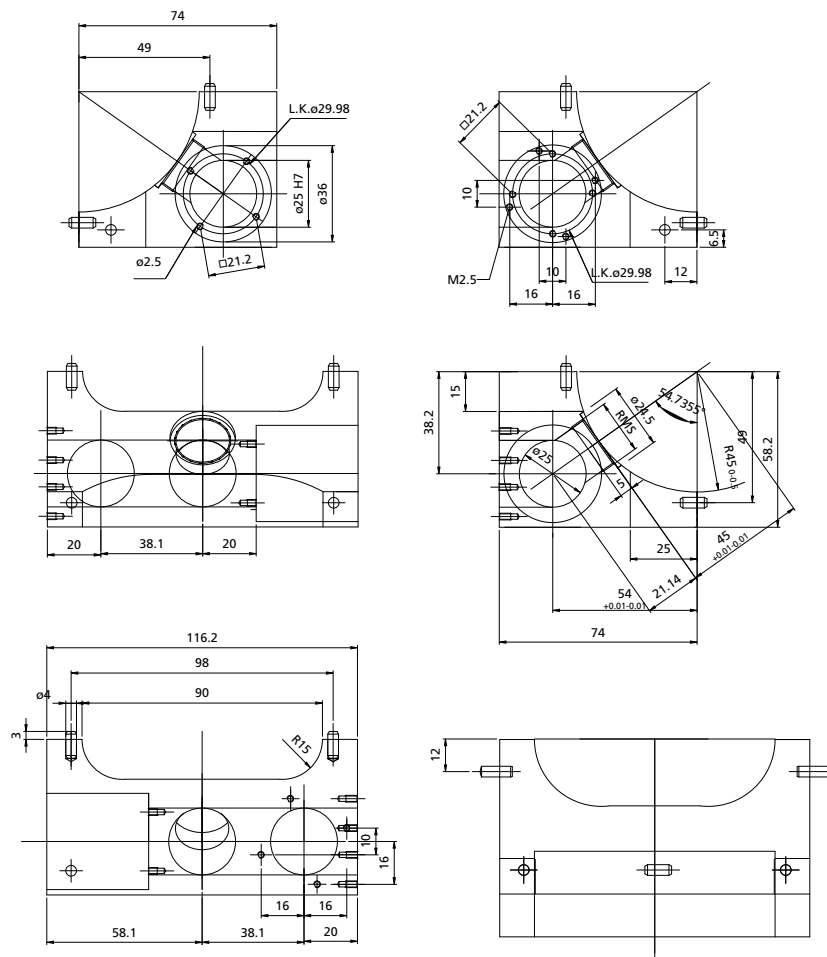


Fig. 1 Drawings of the objective holder unit for the MIAM, dimensions in millimeters.

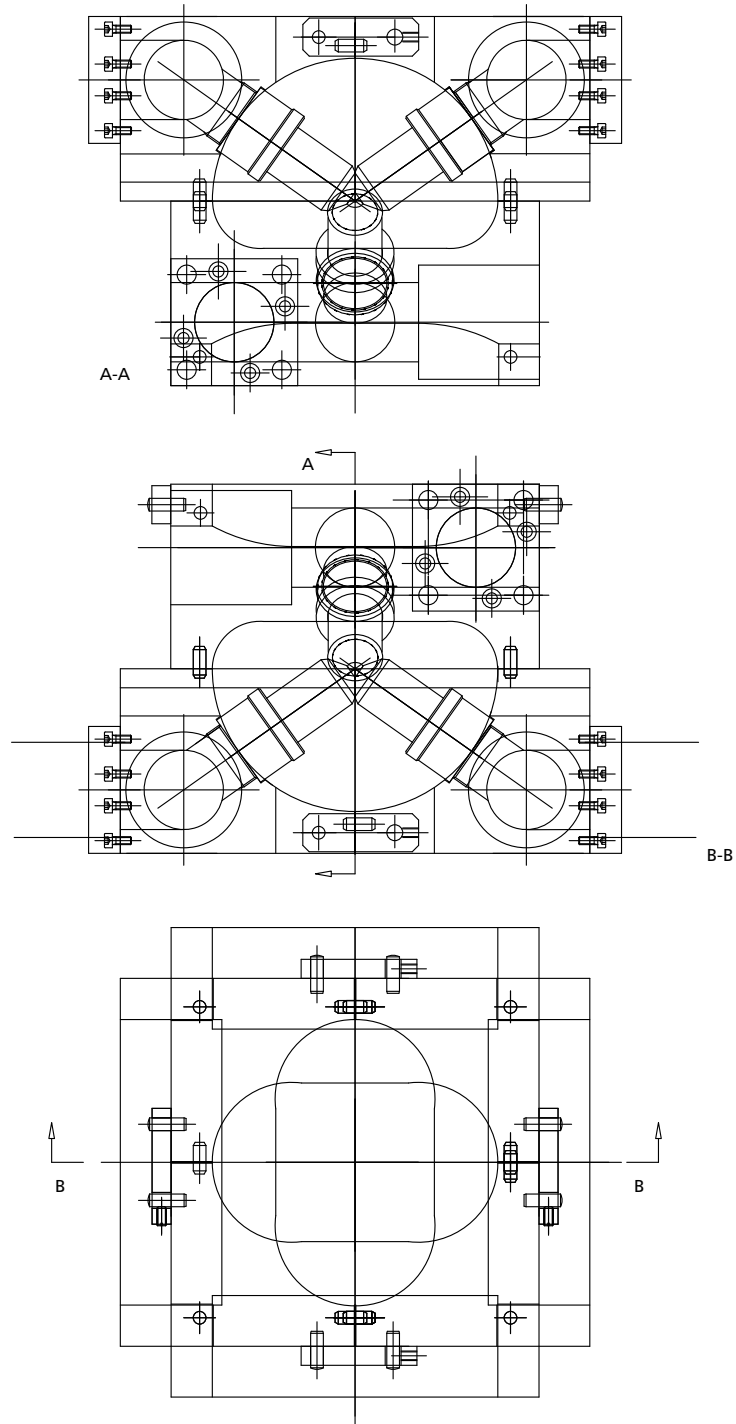


Fig. 2 The assembled view of the four units to hold the objectives in the MIAM.

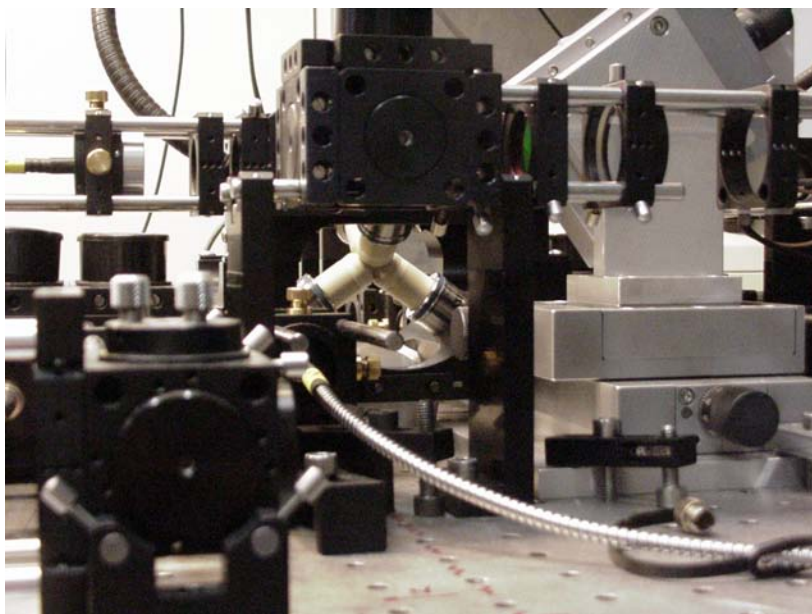


Fig. 3 Photograph of the core of the MIAM from the side. The four objectives, one fiber for illumination, and the manipulator for the capillaries (on the right) are visible.

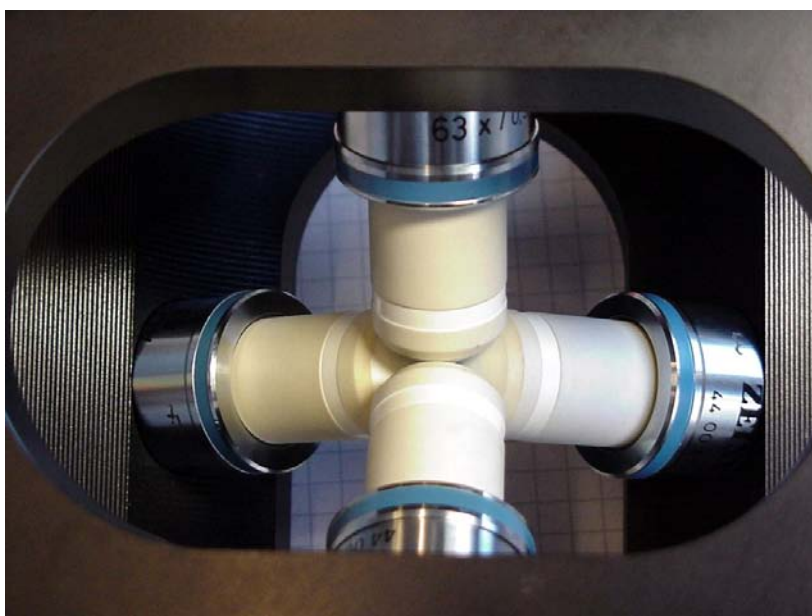


Fig. 4 View of the four objective lenses in the MIAM from above.

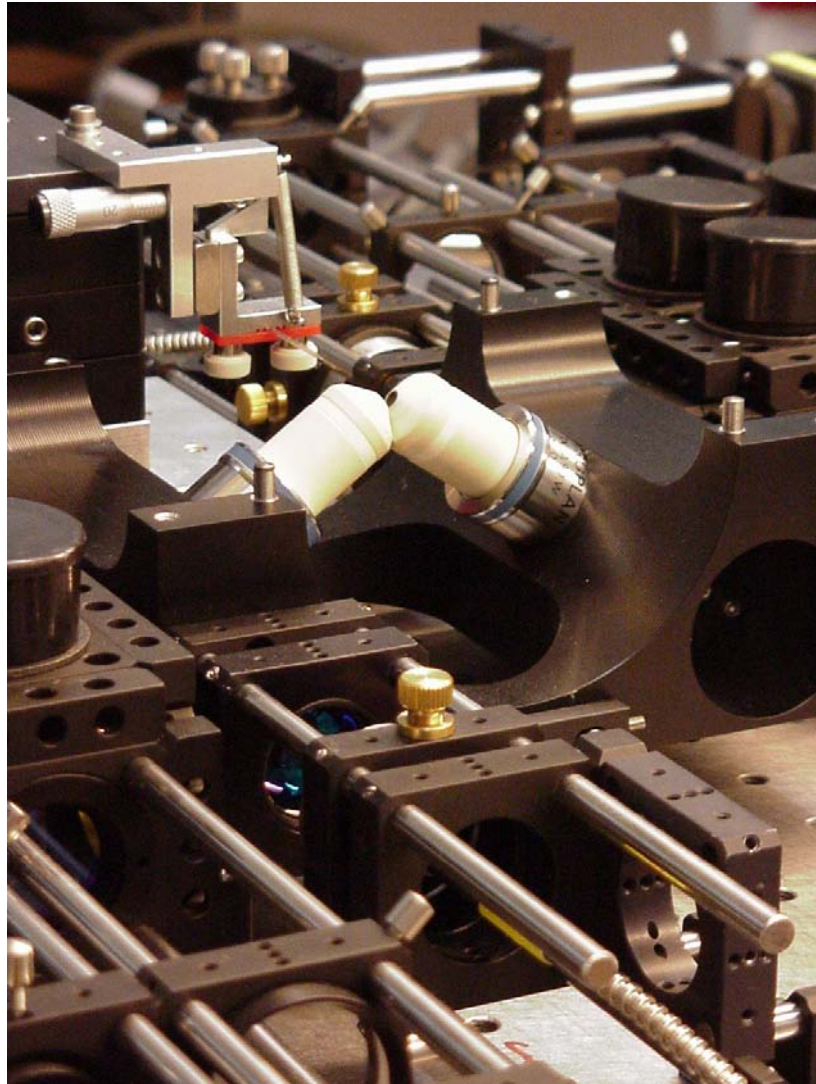


Fig. 5 View on the bottom two objective lenses. The top half is removed.

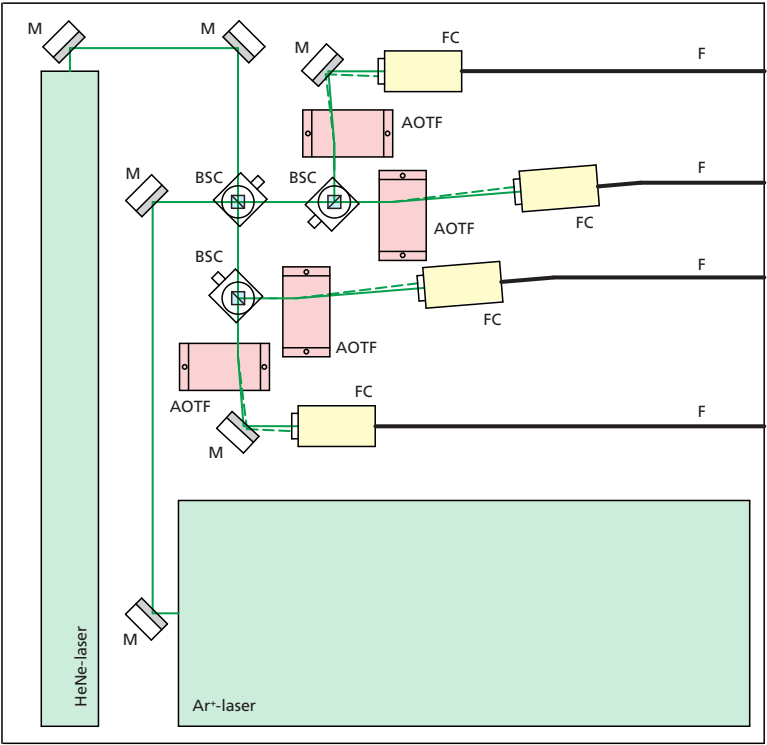


Fig. 6 Laser unit of the MIAM. The output of two lasers is combined into one beam and split into four beams which are then directed through AOTFs into fibers. M: mirror, FC: fiber coupler, BSC: beam splitter cube, AOTF: acousto-optical tunable filter, F: fiber.

Table 1 Main components of the MIAM and DAOM.

quantity	supplier	item
1	Spectra-Physics	Nd-YAG laser, 1064 nm, 10 W
1	Laser 2000	Ar ⁺ -laser, 488 nm, 40 mW
1	Coherent	HeNe-laser, 543 nm, 5 mW
4	A.A	AOTF, 2 channel
4	A.A	AOM, 1064 nm
8	Point Source	Kineflex fiber coupler
8	Point Source	single mode fiber
4	Zeiss	objective lens Achroplan 63×, 0.9W
4	Sony	Firewire camera XCD-SX900
1	PI	piezo R762.00
4	Hamamatsu	PSD S5991-01
	Linos	mechanical components (dichroic) mirrors, beam splitters, lenses,...

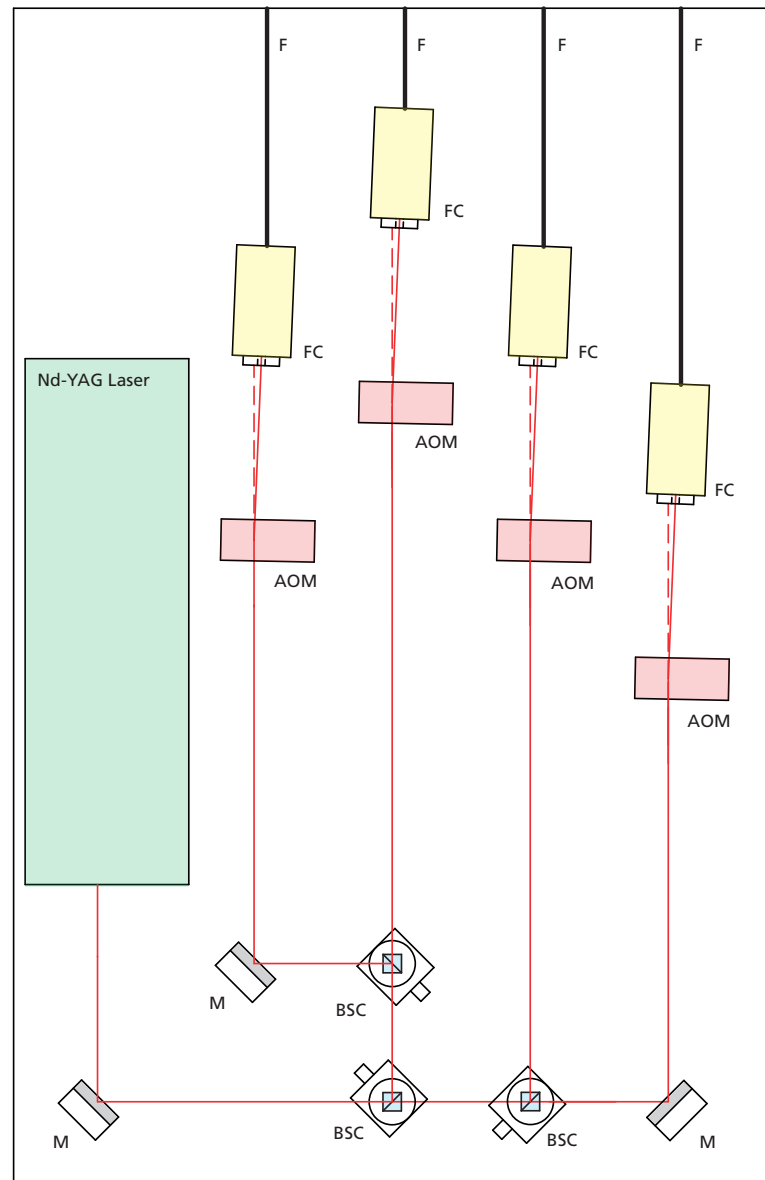


Fig. 7 Laser unit of the DAOM. The output of the laser is split into four beams which are then directed through AOMs into fibers. M: mirror, FC: fiber coupler, BSC: beam splitter cube, AOM: acusto-optical modulator, F: fiber.



Fig. 8 Detail of the laser unit of the MIAM: AOTFs (red), fiber couplers (black), fibers (silver), mirrors, and cubic beam splitters. The unit for the DAOM looks similar.

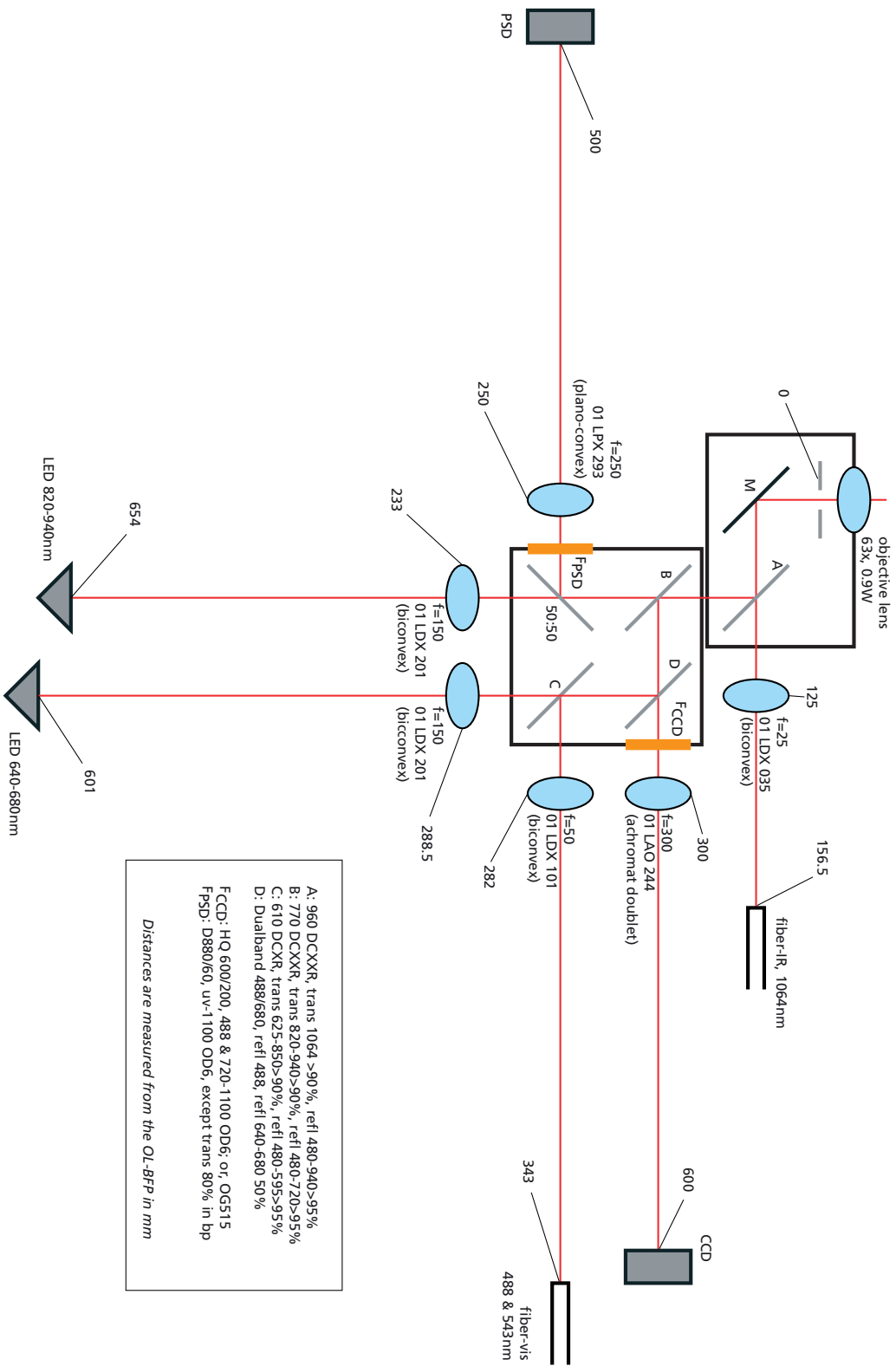


Fig. 9 Optics of one arm of the MIAM.

Selective Plane Illumination Microscope (SPIM)

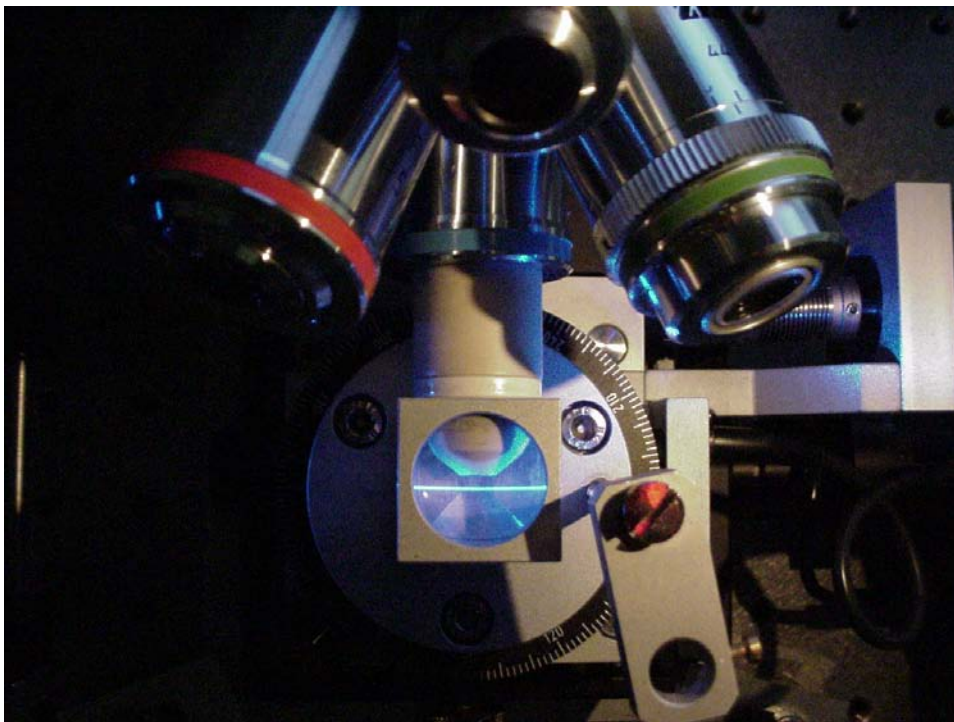


Fig. 10 The light sheet illumination in the SPIM. The scattered light in the chamber is visible. The sample is placed in the center of the chamber.

Table 2 Objective lenses used in the SPM. The light sheet thickness in the center is given. It is double on the edges of the FOV (field of view). NA: numerical aperture, WD: working distance.

medium	name	magn.	pixelsize / μm	FOV / mm	NA	WD / mm	$R_x, y / \mu\text{m}$	$R_z / \mu\text{m}$	lightsheet / μm
air	Fluar	5	1.290	1.32	0.25	12.50	1.27	16.64	7.86
air	Epiplan	10	0.645	0.66	0.20	18.40	1.59	26.00	5.56
water	Achroplan	10	0.645	0.66	0.30	3.10	1.06	15.37	5.56
water	Achroplan	20	0.323	0.33	0.50	1.97	0.63	5.53	3.93
water	Achroplan	40	0.161	0.17	0.80	3.30	0.40	2.16	2.78
water	Achroplan	63	0.102	0.10	0.90	1.45	0.35	1.70	2.21
water	Achroplan	100	0.065	0.07	1.00	0.97	0.32	1.38	1.76

Bibliography

- A. ABBOTT. Biology's new dimension. *Nature*, **424**, 870, 2003.
- D. A. AGARD. Optical sectioning microscopy: Cellular architecture in three dimensions. *Ann. Rev. Biophys. Bioeng.*, **13**, 191, 1984.
- A. ASHKIN. Acceleration and trapping of particles by radiation pressure. *Phys. Rev. Lett.*, **24**(4), 156, 1970.
- A. ASHKIN. Optical trapping and manipulation of neutral particles using lasers. *Proc. Natl. Acad. Sci.*, **94**, 4853, 1997.
- A. ASHKIN and J. M. DZIEDZIC. Optical levitation by radiation pressure. *Appl. Phys. Lett.*, **19**(8), 283, 1971.
- A. ASHKIN and J. M. DZIEDZIC. Optical levitation in high vacuum. *Appl. Phys. Lett.*, **28**(6), 333, 1976.
- A. ASHKIN and J. M. DZIEDZIC. Observation of radiation-pressure trapping of particles by alternating light beams. *Phys. Rev. Lett.*, **54**(12), 1245, 1985.
- A. ASHKIN, J. M. DZIEDZIC, J. E. BJORKHOLM, and S. CHU. Observation of a single-beam gradient force optical trap for dielectric particles. *Opt. Lett.*, **11**(5), 288, 1986.
- A. ASHKIN and J. P. GORDON. Stability of radiation-pressure particle traps: an optical Earnshaw theorem. *Opt. Lett.*, **8**(10), 511, 1983.
- B. BAILEY, D. L. FARKAS, D. L. TAYLOR, and F. LANNI. Enhancement of axial resolution in fluorescence microscopy by standing-wave excitation. *Nature*, **366**(6450), 44, 1993.
- M. BORN and E. WOLF. *Principles of optics*. Cambridge Univ. Press, 7th edition, 1999.
- J. BRADL, M. HAUSMANN, V. EHEMANN, D. KOMITOWSKI, and C. CREMER. A tilting device for three-dimensional microscopy: application to in situ imaging of interphase cell nuclei. *J. Microsc.*, **168**(1), 47, 1992.
- J. BRADL, M. HAUSMANN, B. SCHNEIDER, B. RINKE, and C. CREMER. A versatile 2π -tilting device for fluorescence microscopes. *J. Microsc.*, **176**(3), 211, 1994.

- A. CAN, O. AL-KOFAHI, S. LASEK, D. SZAROWSKI, J. TURNER, and B. ROYSAM. Attenuation correction in confocal laser microscopes: a novel two-view approach. *J Microsc*, **211**(Pt 1), 67, 2003.
- M. CHALFIE, Y. TU, G. EUSKIRCHEN, W. W. WARD, and D. C. PRASHER. Green fluorescent protein as a marker for gene expression. *Science*, **263**, 802, 1994.
- S. D. COLLINS, R. J. BASKIN, and D. G. HOWITT. Microinstrument gradient-force optical trap. *Appl. Opt.*, **38**(28), 6068, 1999.
- J. CURTIS, B. KOSS, and D. GRIER. Dynamic holographic optical tweezers. *Opt. Commun.*, **207**, 169, 2002.
- W. DENK, J. H. STRICKLER, and W. W. WEBB. Two-photon laser scanning fluorescence microscopy. *Science*, **248**, 73, 1990.
- K. A. EDWARDS, M. DEMSKY, R. A. MONTAGUE, N. WEYMOUTH, and D. P. KIEHART. GFP-moesin illuminates actin cytoskeleton dynamics in living tissue and demonstrates cell shape changes during morphogenesis in drosophila. *Dev. Biol.*, **191**(1), 103, 1997.
- E. FUCHS, J. S. JAFFE, R. A. LONG, and F. AZAM. Thin laser light sheet microscope for microbial oceanography. *Opt. Express*, **10**(2), 145, 2002.
- R. C. GAUTHIER and A. FRANGIOUDAKIS. Optical levitation particle delivery system for a dual beam fiber optic trap. *Appl. Opt.*, **39**(1), 26, 2000.
- D. G. GRIER. A revolution in optical manipulation. *Nature*, **424**(6950), 810, 2003.
- M. G. L. GUSTAFSSON. Extended resolution fluorescence microscopy. *Curr. Opin. Struc. Biol.*, **9**, 627, 1999.
- M. G. L. GUSTAFSSON. Surpassing the lateral resolution limit by a factor of two using structured illumination microscopy. *J. Microsc.*, **198**(2), 82, 2000.
- M. G. L. GUSTAFSSON, D. A. AGARD, and J. W. SEDAT. I⁵M: 3D widefield light microscopy with better than 100 nm axial resolution. *J. Microsc.*, **195**(1), 10, 1999.
- O. HAEBERLE, C. XU, A. DIETERLEN, and S. JACQUEY. Multiple-objective microscopy with three-dimensional resolution near 100 nm and a long working distance. *Opt. Lett.*, **26**(21), 1684, 2001.
- J. HECKSHER-SØRENSEN and J. SHARPE. 3D confocal reconstruction of gene expression in mouse. *Mech. Develop.*, **100**, 59, 2001.
- S. HELL and E. H. K. STELZER. Properties of a 4Pi confocal fluorescence microscope. *J. Opt. Soc. Am. A*, **9**, 2159, 1992.
- S. W. HELL. Toward fluorescence nanoscopy. *Nat. Biotechnol.*, **21**(11), 1347, 2003.

- D. HUANG, E. A. SWANSON, C. P. LIN, J. S. SCHUMAN, W. G. STINSON, W. CHANG, M. R. HEE, T. FLOTTE, K. GREGORY, and C. A. PULIAFITO. Optical coherence tomography. *Science*, **254**, 1178, 1991.
- D. HUBER, M. KELLER, and D. ROBERT. 3D light scanning macrography. *J. Microsc.*, **203**(2), 208, 2002.
- J. HUISKEN. *Size determination and controlled movement of Mie-particles by means of optical levitation*. Diploma thesis, University of Heidelberg, 2000.
- J. HUISKEN, J. SWOGER, and E. STELZER. Optical levitation of absorbing particles with a nominally gaussian laser beam. *Opt. Lett.*, **27**(14), 1223, 2002.
- J. HUISKEN, J. SWOGER, and E. H. K. STELZER. Active particle manipulation with four laser beams. In D. V. NICOLAU, J. ENDERLEIN, R. C. LEIF, and D. L. FARKAS, editors, *Imaging, Manipulation, and Analysis of Biomolecules, Cells, and Tissues II*, volume 5322. SPIE, 2004a.
- J. HUISKEN, J. SWOGER, and E. H. K. STELZER. Optical sectioning deep inside live embryos by selective plane illumination microscopy. *submitted*, 2004b.
- J. HUISKEN, J. SWOGER, and E. H. K. STELZER. Three-dimensional optical manipulation using four collimated intersecting laser beams. *submitted*, 2004c.
- S. M. HURTLEY and L. HELMUTH. The future looks bright. . . . *Science*, **300**, 75, 2003.
- T. IWAMATSU. Stages of normal development in the medaka *oryzias-latipes*. *Zool. Sci.*, **11**(6), 825, 1994.
- J. D. JACKSON. *Classical Electrodynamics*. John Wiley & Sons, New York, 2nd edition, 1975.
- J. E. N. JONKMAN and E. H. K. STELZER. Resolution and contrast in confocal and two-photon microscopy. In A. DIASPRO, editor, *Confocal and Two-Photon Microscopy: Foundations, Applications, and Advances*, chapter 5, pages 101–125. Wiley-Liss, Inc., New York, 2002.
- S. KIKUCHI, K. SONOBE, S. MASHIKO, Y. HIRAOKA, and N. OHYAMA. Three-dimensional image reconstruction for biological micro-specimens using a double-axis fluorescence microscope. *Opt. Commun.*, **138**, 21, 1997.
- T. A. KLAR, S. JAKOBS, M. DYBA, A. EGNER, and S. W. HELL. Fluorescence microscopy with diffraction resolution barrier broken by stimulated emission. *PNAS*, **97**(15), 8206, 2000.
- M. KOZUBEK, M. SKALNÍKOVÁ, P. MATULA, E. BÁRTOVÁ, J. RAUCH, F. NEUHAUS, H. EIPPEL, and M. HAUSMANN. Automated microaxial tomography of cell nuclei after specific labelling by fluorescence in situ hybridisation. *Micron*, **33**(7-8), 655, 2002.

- S. LINDEK, R. PICK, and E. H. K. STELZER. Confocal theta microscope with three objective lenses. *Rev. Sci. Instrum.*, **65**, 3367, 1994a.
- S. LINDEK, N. SALMON, C. CREMER, and E. H. K. STELZER. Theta-microscopy allows phase regulation in 4pi(a)-confocal 2photon fluorescence microscopy. *Optik*, **98**, 15, 1994b.
- S. LINDEK, T. STEFANY, and E. H. K. STELZER. Single-lens theta microscopy - a new implementation of confocal theta microscopy. *J. Microsc.*, **188**, 280, 1997.
- S. LINDEK, E. H. K. STELZER, and S. W. HELL. Two new high-resolution confocal fluorescence microscopies (4Pi and Theta) with one and two photon excitation. In J. B. PAWLEY, editor, *Handbook of biological confocal microscopy*, pages 417–429. Plenum Press, New York and London, 1995.
- A. Y. LOUIE, M. M. HÜBNER, E. T. AHRENS, U. ROTHBÄCHER, R. MOATS, R. E. JACOBS, S. E. FRASER, and T. J. MEADE. In vivo visualisation of gene expression using magnetic resonance imaging. *Nat. Biotechnol.*, **18**, 321, 2000.
- S. G. MEGASON and S. E. FRASER. Digitizing life at the level of the cell: high performance laser-scanning microscopy and image analysis for in toto imaging of development. *Mech. Develop.*, **120**, 1407, 2003.
- V. G. MINOGIN. A tetrahedral light pressure trap for atoms. *Opt. Commun.*, **43**(2), 119, 1982.
- M. A. A. NEIL, R. JUŠKAITIS, and T. WILSON. Method of obtaining sectioning by using structured light in a conventional microscope. *Opt. Lett.*, **22**(24), 1905, 1997.
- J. PALERO, W. GARCIA, and C. SALOMA. Two-color (two-photon) excitation fluorescence with two confocal beams and a raman shifter. *Opt. Commun.*, **211**(1-6), 65, 2002.
- J. B. PAWLEY. *Handbook of Biological Confocal Microscopy*. Plenum Press, 1995.
- P. RODRIGO, R. ERIKSEN, V. DARIA, and J. GLÜCKSTAD. Interactive light-driven and parallel manipulation of inhomogeneous particles. *Opt. Exp.*, **10**(26), 1550, 2002.
- S. W. RUFFINS, R. E. JACOBS, and S. E. FRASER. Towards a Tralfamadorian view of the embryo: multidimensional imaging of development. *Curr. Opin. Neurobiol.*, **12**, 580, 2002.
- K. SÄTZLER and R. EILS. Resolution improvement by 3-D reconstruction from tilted views in axial tomography and confocal theta microscopy. *Bioimaging*, **5**, 171, 1997.
- J. SHARPE, U. AHLGREN, P. PERRY, B. HILL, A. ROSS, J. HECKSHER-SØRENSEN,

- R. BALDOCK, and D. DAVIDSON. Optical projection tomography as a tool for 3d microscopy and gene expression studies. *Science*, **296**, 541, 2002.
- P. J. SHAW. Three-dimensional optical microscopy using tilted views. *J. Microsc.*, **128**(2), 165, 1990.
- P. J. SHAW, D. A. AGARD, Y. HIRAOKA, and J. W. SEDAT. Tilted view reconstruction in optical microscopy. *Biophys. J.*, **55**, 101, 1989.
- H. SIEDENTOPF and R. ZSIGMONDY. Über die Sichtbarmachung und Größenbestimmung ultramikroskopischer Teilchen, mit besonderer Anwendung auf Goldrubingläser. *Ann. Physik-Leipzig*, **10**(4), 1, 1903.
- G. SINCLAIR, P. JORDAN, J. LEACH, M. PADGETT, and J. COOPER. Defining the trapping limits of holographical optical tweezers. *J. Mod. Opt.*, **51**(3), 409, 2004.
- E. H. K. STELZER. Contrast, resolution, pixelation, dynamic range and signal-to-noise ratio: fundamental limits to resolution in fluorescence light microscopy. *J. Microsc.*, **189**, 15, 1998.
- E. H. K. STELZER and S. LINDEK. Fundamental reduction of the observation volume in far-field light-microscopy by detection orthogonal to the illumination axis - confocal theta microscopy. *Opt. Commun.*, **111**, 536, 1994.
- J. SWOGER, J. HUISKEN, and E. STELZER. Multiple imaging axis microscopy improves resolution for thick sample applications. *Opt. Lett.*, **28**(18), 1654, 2003.
- J. SWOGER, S. LINDEK, T. STEFANY, F. HAAR, and E. STELZER. A confocal fiber-coupled single-lens theta microscope. *Rev. Sci. Instrum.*, **69**(8), 2956, 1998.
- V. THERMES, C. GRABHER, F. RISTORATORE, F. BOURRAT, A. CHOULIKA, J. WITTBRODT, and J. JOLY. I-SceI meganuclease mediates highly efficient transgenesis in fish. *Mech. Develop.*, **118**, 91, 2002.
- T. D. WANG, C. H. CONTAG, M. J. MANDELLA, N. Y. CHAN, and G. S. KINO. Dual-axes confocal microscopy with post-objective scanning and low-coherence heterodyne detection. *Opt Lett*, **28**(20), 1915, 2003.
- D. J. WEBB and A. F. HOROWITZ. New dimensions in cell migration. *Nat. Cell Biol.*, **120**, 1407, 2003.
- W. J. WENINGER and T. MOHUN. Phenotyping transgenic embryos: a rapid 3D screening method based on episcopic fluorescence image capturing. *Nat. Genet.*, **30**, 59, 2002.
- J. WITTBRODT, A. SHIMA, and M. SCHARTL. Medaka—a model organism from the far east. *Nat. Rev. Genet.*, **3**, 53, 2002.
- T. WOHLAND, A. ROSIN, and E. H. K. STELZER. Theoretical determination of

the influence of the polarization on forces exerted by optical tweezers. *Optik*, **102**(4), 181, 1996.

W. R. ZIPFEL, R. M. WILLIAMS, and W. W. WEBB. Nonlinear magic: multiphoton microscopy in the bioscience. *Nat. Biotechnol.*, **21**(11), 1369, 2003.